TELEOPERATED POSITIONING AND MICROSCOPY SYSTEM FOR DIAGNOSTIC SINGLE-EVENT EFFECTS TESTING OF INTEGRATED CIRCUITS

A Thesis

by

JACKSON DOUGLAS WEDELICH

Submitted to the Graduate and Professional School of
Texas A&M University
in partial fulfillment of the requirements for the degree of

MASTER OF SCIENCE

Chair of Committee,	Rainer Fink
Committee Members,	Xingyong Song
	Jose Silva-Martinez
Head of Department,	Reza Langari

December 2021

Major Subject: Engineering Technology

Copyright 2021 Jackson Douglas Wedelich

ABSTRACT

The semiconductor industry is engaged in a process of innovation for space applications. Trends in space exploration and satellite technology are driving requirements for processing power higher and constraints for integrated circuit (IC) size lower. The processes for characterization and testing for radiation hardness of semiconductor devices, governed by the United States Department of Defense, remains focused on single-event effects and total ionizing dose at the level of an entire IC. Though these standards effectively give consumers the information and quality they need, simply testing to these standards does not enable effective innovation for designers of the devices. In the process of characterizing the radiation hardness of ICs, it is useful to isolate radiation exposure to individual functional blocks within a circuit. This radiation isolation testing can lead to discoveries of varying vulnerabilities in functional blocks of an IC. Radiation isolation testing is time consuming and costly because of the tedious process and repetitive actions required. This project combines mechanization of the existing process with remote operation capabilities to reduce repetitive actions and expand the capabilities of radiation isolation testing. This document covers the requirements of the system and its successful implementation.

ACKNOWLEDGEMENTS

I would like to thank my committee chair, Dr. Fink, and my committee members, Dr. Song and Dr. Silva-Martinez, for their guidance and support throughout the course of this research. Their feedback and guidance for this research has been invaluable. Thanks also go to the Engineering Technology & Industrial Distribution department faculty and staff.

Additionally, I have much gratitude for the incredible support of Texas Instruments Inc. and the Texas A&M Cyclotron Institute. The work of Joel Cruz, Tyler Lew, Andrew Joseph, Dr. Vladimir Horvat, and Dr. Henry Clark has been instrumental in the completion of this research.

Finally, I would like to thank my friends, parents, and wife for their love, patience, and prayers.

CONTRIBUTORS AND FUNDING SOURCES

Contributors

This work was supervised by a thesis committee consisting of Dr. Rainer Fink and Dr. Xingyong Song of the Department of Engineering Technology and Industrial Distribution as well as Dr. Jose Silva-Martinez of the Department of Electrical Engineering. Dylan Blezinger of the Department of Engineering Technology and Industrial Distribution was tasked with a portion of this project. While conducting our own individual research on this project, portions of the work required collaboration. Any work completed solely by Dylan Blezinger or collaboratively with Dylan Blezinger represented in this document is clearly noted in the text.

All other work conducted for the thesis, including the entire written document, was completed by me, Jackson Wedelich, independently.

Funding Sources

This work was funded by Texas Instruments Inc. through Texas A&M University.

NOMENCLATURE

TI	Texas Instruments Inc.
PCB	Printed Circuit Board
IC	Integrated Circuit
TID	Total Ionizing Dose
SEE	Single-event Effect
SEL	Single-event Latch-Up
SEB	Single-event Burnout
SEGR	Single-event Gate-Rupture
SET	Single-event Transient
SEU	Single-event Upset
SEFI	Single-event Functional Interrupt
NA	Numerical Aperture
PSF	Point-Spread Function
WD	Working Distance
FOV	Field of View
DOF	Depth of Focus
PWM	Pulse-Width Modulation
VREG	Voltage Regulator
OEM	Original Equipment Manufacturer
LED	Light-Emitting Diode
µC	Microcontroller

EN	Enable
PUL	Pulse
DIR	Direction
GND	Ground
CMOS	Complementary Metal-Oxide Semiconductor
UDP	User Datagram Protocol
ADC	Analog-to-Digital Converter
GUI	Graphical User Interface
FEDC	Fischer Engineering Design Center
CNC	Computer Numerical Control
PLA	Polylactic Acid
DMM	Digital Multimeter
RT	Rise Time
FT	Fall Time

TABLE OF CONTENTS

Page

ABSTRACT ii

ACKNOWLEDGEMENTS iii

CONTRIBUTORS AND FUNDING SOURCES iv

NOMENCLATURE v

TABLE OF CONTENTS vii

LIST OF FIGURES ix

LIST OF TABLES xiii

1. INTRODUCTION 1

1.1. Problem 1
1.2. Proposal 4

2. BACKGROUND AND SYSTEM REQUIREMENTS 6

2.1. Radiation Effects Testing 6
2.1.1. Mechanical System Requirements 8
2.1.2. Motion System Requirements 9
2.2. Microscopy 10
2.2.1. Microscope System Requirements 11
2.2.2. Important Terminology in Microscopy 14
2.2.3. Motorized Focus 23
2.3. Motion Systems 26
2.4. Stepper Motor Control 29

3. SYSTEM ARCHITECTURE 31

3.1. Microscope 31
3.1.1. Olympus BXFM 31
3.1.2. Objectives 33
3.2. Mechanical and Motion Components 39
3.2.1. Clearance Verification 49
3.3. Electrical Design 53
3.3.1. PCB Design 56

3.4. Microcontroller Software 61
3.5. Communication and Control 61
3.6. Camera Software 64
3.7. Concept of Operations 64

4. IMPLEMENTATION 66

4.1. Mechanical and Microscope Components...66
4.2. Electrical Implementation..68
4.3. Final Integration 71

5. MEASUREMENTS AND RESULTS 72

5.1. Motion Measurements 72
5.1.1. Data Collection Procedure - Motion 74
5.1.2. Motion Results and Analysis..74
5.2. Electrical Measurements..82
5.2.1. Electrical Results and Analysis 82
5.3. Optical Measurements 85
5.3.1. Optical Results and Analysis..86
5.4. Costing Data 99

6. CONCLUSIONS & FUTURE WORK 101

6.1. Conclusions 101
6.2. Future Work...102

REFERENCES 103

APPENDIX A 106

APPENDIX B 111

LIST OF FIGURES

Page

Figure 1. 3D-View of Testing Area [1]. 2

Figure 2. Proposed System. 5

Figure 3. Angled View of the In-Air Test Station. 8

Figure 4. Test Stand Platter. 9

Figure 5. Annotated View of the In-Air Test Station. 10

Figure 6. Traditional Upright Microscope [16]. 12

Figure 7. Reflected Light Microscopy. 13

Figure 8. Numerical Aperture and Focal Point Diagram 14

Figure 9. Airy Pattern [18]. 16

Figure 10. Working Distance Diagram 16

Figure 11. Field of View Diagram 18

Figure 12. Depth of Focus Diagram 19

Figure 13. Spherical Aberration [21] 20

Figure 14. Chromatic Aberration Diagram [21]. 21

Figure 15. Astigmatism Aberration [21]. 22

Figure 16. Comatic Aberration [21]. 23

Figure 17. Olympus DSX1000 [22]. 24

Figure 18. Navitar 12X Stereoscope [23]. 25

Figure 19. Optical Axis Incremental Motion versus DOF Increment Concept Diagram. 26

Figure 20. Linear Motion Stage from PI [24]. 26

Figure 21. Ball Screw Cutaway Illustration [25]. 27

Figure 22. Roller Bearings on Stage in Contact with Precision Rod. 28

Figure 23. Precision Rods with Cycling Bearings [26]. 28

Figure 24. Linear Slide Rail. 29

Figure 25. Annotated 3D Model of the BXFM System – Angled Rear View. 32

Figure 26. Annotated 3D Model of the BXFM System – Angled Front View 33

Figure 27. Mechanical Drawing of the MPLN5X Objective [27]. 34

Figure 28. Mechanical Drawing of the LMPLFLN10X Objective [27]. 35

Figure 29. Mechanical Drawing of the LMPLFLN20X Objective [27]. 36

Figure 30. Mechanical Drawing of the LMPLFLN50X Objective [27]. 37

Figure 31. Mechanical Drawing of the SLMPLN100X Objective [27]. 38

Figure 32. Parfocal Objective Series. 39

Figure 33. 3D Model of the In-Air Test Station. 40

Figure 34. Adapter Plate. 41

Figure 35. Microscope Linear Motion Rail, Stabilizing Linear Slide Rails, and Stabilizing Brackets. 41

Figure 36. Microscope Support Bracket and BXFM Microscope System. 43

Figure 37. PCB/Pinhole Group Linear Motion Rail, Stabilizing Linear Slide Rails, and Brackets. 44

Figure 38. PCB/Pinhole Group Bracket, Pinhole Linear Motion Rail, and Vertical Manual Pinhole Adjuster. 45

Figure 39. Pinhole Frame, Horizontal PCB Linear Motion Rail, and Optical Axis Manual Adjuster. 46

Figure 40. Vertical PCB Linear Motion Rail, PCB Mount, and PCB. 48

Figure 41. Pinhole/Microscope Clearance – Beam Port View. 49

Figure 42. PCB's Ability to Reach <40mm to Beam Port. 50

Figure 43. Ability to Test with Smallest Pinhole. 51

Figure 44. Ability to Test without Beam Reduction. 52

Figure 45. Clearance within Working Distance of Objectives. 53
Figure 46. Electrical Block Diagram. 54
Figure 47. Stepper Motor Driver [28]. 55
Figure 48. 24V/12V Voltage Regulator Schematic. 56
Figure 49. 24V/5V Voltage Regulator Schematic. 57
Figure 50. 3.3V/5V Level Translators – Schematic. 58
Figure 51. Teensy 4.1 Connections - Schematic. 59
Figure 52. Printed Circuit Board Manufacturing Preview. 60
Figure 53. Teensy 4.1 Microcontroller [29]. 60
Figure 54. LabVIEW Control GUI. 62
Figure 55. Manufactured Adapter Plate. 66
Figure 56. Mechanical Component and Microscope Integration. 67
Figure 57. Printed Circuit Board from JLCPCB. 68
Figure 58. Populated Printed Circuit Board. 69
Figure 59. Electronics Enclosure – Open-Top View 70
Figure 60. Electronics Enclosure – Closed Side View. 70
Figure 61. Full System Integration. 71
Figure 62. Electronic Outside Micrometer – Starrett [30]. 72
Figure 63. Average Horizontal Error: PCB Left. 75
Figure 64. Average Horizontal Error: PCB Right. 76
Figure 65. Average Vertical Error: PCB Down. 77
Figure 66. Average Vertical Error: PCB Up. 78
Figure 67. Average Horizontal Error: Pinhole Left. 79
Figure 68. Average Horizontal Error: Pinhole Right. 80

Figure 69. 3.3V PWM Signal – Oscilloscope. 83

Figure 70. 5V PWM Signal – Oscilloscope. 83

Figure 71. UCC27282EVM-335 PCB from Texas Instruments. 85

Figure 72. 5X Objective FOV on P10 Standard. 86

Figure 73. 10X Objective FOV on P10 Standard. 87

Figure 74. 20X Objective FOV on P3 Standard. 88

Figure 75. 50X Objective FOV on P3 Standard. 88

Figure 76. 100X FOV on P3 Standard. 89

Figure 77. UCC27282DRC Imaged with 5X Objective. 91

Figure 78. Stitched Image of UCC27282DRC with 5X Objective. 91

Figure 79. UCC27282DRC Imaged with 100X Objective. 92

Figure 80. 500µm Pinhole Imaged with 5X Objective. 93

Figure 81. IC Region of Interest Imaged with 5X Objective. 93

Figure 82. IC Region of Interest Imaged through 500µm Pinhole with 5X Objective. 94

Figure 83. 200µm Pinhole Imaged with 20X Objective. 94

Figure 84. IC Region of Interest Imaged through 200µm Pinhole with 20X Objective. 95

Figure 85. All Pinholes Coincident with All Light Cones. 96

Figure 86. Required Distance from 500µm Pinhole to IC without Light Cone Intersection – 5X Objective. 97

Figure 87. Required Distance from 25µm Pinhole to IC without Light Cone Intersection – 5X Objective. 98

LIST OF TABLES

Page

Table 1. Increments of Motion for Each Axis. 63

Table 2. Horizontal PCB Rail Movement Statistics. 76

Table 3. Vertical PCB Rail Movement Statistics. 78

Table 4. Pinhole Movement Statistics. 81

Table 5. Electrical Results - Digital Multimeter. 82

Table 6. PWM Rise and Fall Time Results. 84

Table 7. PWM Amplitude and Frequency Results. 84

Table 8. Calculated FOV versus Measured FOV. 90

Table 9. Parameters for Theoretical Objective Capable of Imaging IC through 25μm Pinhole, ~2mm Air Gap. 99

Table 10. Cost Breakdown of System. 100

1. INTRODUCTION

Texas Instruments Inc. (TI), the sponsor of this project, conducts radiation effects testing of semiconductor devices at the Texas A&M University Cyclotron Institute. The Cyclotron Institute is home to two cyclotrons, the K150 and K500 cyclotrons, which are the particle accelerators that serve as sources of radiation with various radiation beam energies. The Space Power Team at TI primarily uses the K500 cyclotron and its in-air test station to conduct characterization testing and qualification of their integrated circuits (ICs). The K500 cyclotron is typically outfitted with a circular beam exit port that has a 1” diameter. With this 1” beam, the Space Power Team can conduct full-beam and reduced-beam tests on integrated circuits having a maximum dimension of 10 mm^2. The tests are conducted with the distance between the printed circuit board (PCB) and the exit beam port set to 40mm.

1.1. Problem

In reduced-beam tests, TI is aiming to reduce the affected area to a specific region of interest. This region of interest can be as large as half of an IC to as small as a single transistor. Having the capability to irradiate only a specific portion of an IC gives the team the opportunity to test the radiation tolerance of a radiation-isolated but electrically connected functional block. This opportunity provides the team with valuable information regarding the functionality of their IC and the radiation tolerance of specific functional blocks. For the reduced-beam tests, the team employs an aluminum tape with a pinhole in the center. This aluminum tape is sized and positioned to block irradiation of the IC in all areas except for the pinhole, which allows a specified region of interest to be irradiated. The process for fabricating the pinhole starts with cutting a section of aluminum foil tape with scissors that is sized to cover the entire IC. The

aluminum tape is then flattened by hand on a flat surface. Using the tip of an X-Acto blade or the tip of an oscilloscope voltage probe, a pinhole is punctured in the aluminum tape. Under a microscope, the pinhole is aligned with the desired region of interest on the IC. Finally, the aluminum tape is pressed against the PCB to attach the two together. This process takes place in the Staging Area of the K500 Cyclotron Testing Area, shown in Figure 1.

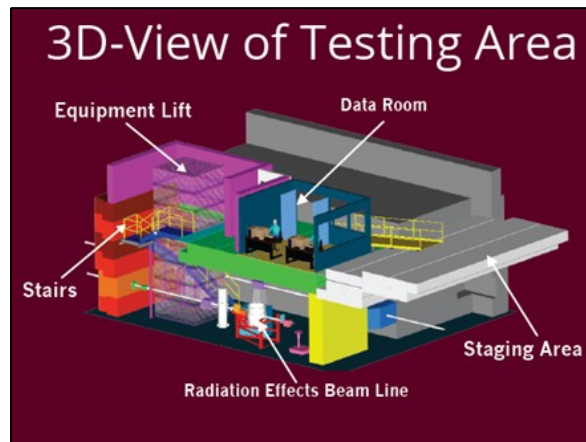

Figure 1. 3D-View of Testing Area [1].

After the shielding has been attached to the PCB, the shielded PCB is then taken downstairs to the testing cave, shown in Figure 1 as the Radiation Effects Beam Line. The Space Power Team mounts the shielded PCB to the test platter in the path of the beam, placing the PCB at distance of 40mm from the exit beam port. Electrical test setup connections are then completed. These connections include power as well as the measurement and monitoring connections for the PCB. Once the test setup connections have been made, the team evacuates the cave, moving upstairs to the Data Room shown in Figure 1. The procedure for evacuating the cave includes the successful completion of a safety chain. This safety chain is a time-bound sequence of actions that, when completed, will unlock the radiation source. The first two steps

are pressing separate inspection station buttons located in the cave. After the buttons have been pressed in the correct order, the team exits the cave, closing the door to the cave on the second floor. Once the door to the cave is closed, the team presses and holds a series of buttons on the second floor. After holding for a preset time, the cave is effectively sealed, and the radiation source is unlocked.

In the Data Room, the team requests the beam from the Control Room via a direct phone line. Once the beam is available and verified to have the desired characteristics, the team can start the radiation effects test, stopping the source when desired.

When the team desires to conduct a test of a different region of interest, it must retrace all actions taken up to this point, requesting permission to enter the cave via the phone line, entering the cave, removing the test connections and shielding, and finally, taking the PCB back to the Staging Area, where a new region of interest can be identified.

This workflow process has several disadvantages. The first disadvantage is that many repetitive actions are required to transition from testing one region of interest to another. This is particularly impactful because of the high cost per hour and limited availability of the K500 cyclotron. The K500 cyclotron costs over $1,000 per hour to use, and the beam is booked 24 hours per day, seven days per week throughout the year. These two factors make efficiency a high-priority for TI. The second disadvantage is the lack of repeatability and accuracy involved in the process of shielding the IC, as TI positions the shielding by hand. Additionally, the shielding on the PCB may move or shift during transportation of the shielded PCB from the Staging Area to the in-air test station downstairs. The third disadvantage of this workflow is the potential for damage to and deformation of the shielding during the cutting, pinhole creation,

handling, and placement processes. Finally, the sensitive IC may experience damage upon removal of the shielding.

Four main opportunities have been identified through the analysis of the problem. The first opportunity can be found in limiting the repetitive test setup actions required to test different regions of interest on a single IC. The second is to reduce human error through mechanization of the positioning process. The third opportunity is to eliminate the attachment of the shielding to the IC. Finally, the transfer of the shielded PCB can also be eliminated. These opportunities turn into the objectives for this research. TI expects a remotely operated positioning and microscopy system that effectively meets the requirements to be discussed in this document.

An additional objective of this research is to investigate the feasibility of imaging an IC through various pinholes with the aforementioned system. The approach, results, and an analysis of this investigation are found at the end of this document.

1.2. Proposal

The proposed solution to the identified problem is a remotely-operated positioning and microscopy system that meets the objectives as described above. The proposed system brings changes to the current workflow process. The proposed workflow starts with the installation of the system in the in-air test station. The PCB will then be mounted to the system, where test setup connections to the PCB can be made. After this step, the team can evacuate the cave, completing the required safety chain. Upon entering the Data Room, the team can remotely identify a region of interest, position the PCB, position the shielding, and direct the radiated test. After the test is complete, the team can start with another region of interest without having to enter the cave. A 3D model of the proposed system can be seen in Figure 2.

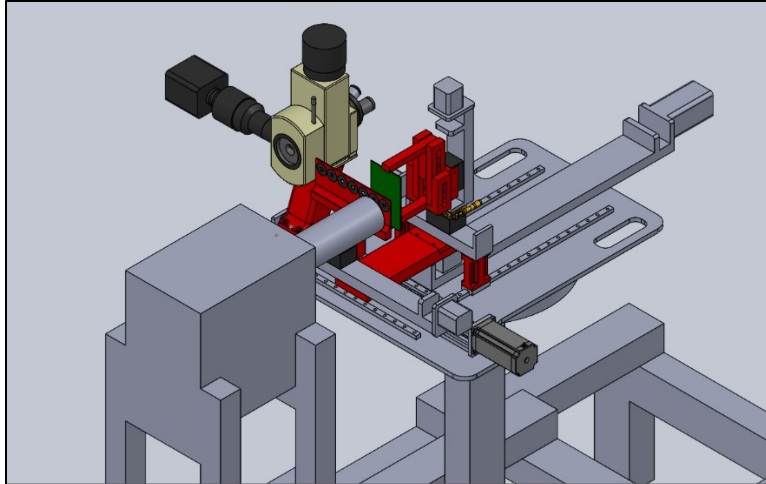

Figure 2. Proposed System.

2. BACKGROUND AND SYSTEM REQUIREMENTS

After identifying the problem, research must be conducted to understand the various factors that impact the system before the proposed system can be designed, implemented, and tested. This section covers the relevant background information related to radiation testing of electronics, the K500 cyclotron's in-air test station, microscopy, and positioning.

2.1. Radiation Effects Testing

TI characterizes and qualifies semiconductor devices for radiation environments for a variety of reasons. In high-altitude and space applications, electronics are subjected to environments that are different from the environments found on Earth. Space electronics are used outside of Earth's atmosphere and magnetic field, which provide substantial protection against the forms of radiation found in space [2]. The exposure to radiation that electronics see in space is sufficient to cause malfunctions that can lead to the loss of an entire mission. With the radiation hardened space electronics sector of the space electronics industry being projected to grow to $1.4B by 2024, TI has a business case for innovation [3]. Additionally, the use and testing of space electronics is regulated by the U.S. Department of Defense with MIL-STD 883-1 [4]. This standard requires companies who certify electronics for use in space to follow specific procedures for radiation effects testing. This regulation allows consumers to have confidence in the products they use for space applications. Finally, the actual testing of ICs for radiation environments is done on Earth with radiation sources because it is both cost-effective and comparable to in-flight testing.

When ICs are exposed to irradiated environments, there are two categories of effects that can be induced. The first category, total ionizing dose (TID) effects, finds its cause in all forms

of radiation acting in a cumulative manner to affect the IC. The effects of total ionizing dose can include shifts of internal thresholds and references, structural damage, and increased leakage. The second category of radiation effects is single-event effects (SEEs). The cause of SEEs is narrowly defined as direct ionization by heavy ions [2], [5]. Within SEEs, there are several individual categories that can be destructive or non-destructive. Destructive SEEs include single-event latch-ups (SEL), single-event burnouts (SEB), single-event gate ruptures (SEGR), and single event transients (SET). These destructive effects have been known to render a transistor, functional block, or IC useless. The non-destructive SEEs are single-event upsets (SEU) and single-event functional interrupts (SEFI), with the addition of some SETs that are not strong enough to be destructive. These non-destructive SEEs do not typically render the IC useless, but they can have a temporary effect on the function of a system. This temporary effect can lead to mission loss [2].

The relative effect of TID versus SEEs is an important consideration for radiation testing teams, as the methods for testing vary from one to the other. With great strides in the design and manufacturing processes of ICs, computational power and electrical efficiency has roughly doubled every one and a half years since the 1940s [6]. During the same timeframe, the size of transistors and spacing between them has also been decreasing. Due to the effect of TID decreasing with total exposed area, the effect of SEEs has seen a relative increase [7]. Additionally, SEEs are more apparent with smaller transistors and spacing. These two factors have contributed to the shift from primarily testing for TID to primarily testing for SEEs [8]. This is the type of testing that TI conducts with the K500 cyclotron.

The K500 cyclotron at the Texas A&M Cyclotron Institute is particularly well-suited for conducting tests for SEEs. Its high-energy (> 40 MeV), heavy ion beam is effective at inducing

SEEs [9], [10]. The K500 has a foil degrader system that is capable of tuning the effective beam that reaches the in-air test station. This in-air test station is better-suited for repetitive testing of separate functional blocks than vacuum-sealed test chambers, which are common in radiation testing facilities [11], [12], [13]. Because the test article must be inside the vacuum chamber for radiation tests in sealed test environments, the testing team must wait on the vacuum sealing process between tests [14], [15]. At the K500 in-air test station, the platter for mounting devices to test has the capability to move in the X, Y, Z, and θ axes. This motion can either be controlled remotely from the Data Room or locally from the in-air test station. After visiting the in-air test station to take measurements, corresponding with a senior research associate at the Cyclotron Institute responsible for the in-air test station platter, and meeting with the TI Space Power Team, a series of mechanical requirements was identified.

2.1.1. Mechanical System Requirements

The first mechanical system requirement to be identified is that the system must allow a PCB being testing to be positioned within the 40mm standard distance to the beam port. Figure 3 shows an angled view of the in-air test station with the beam port on the right.

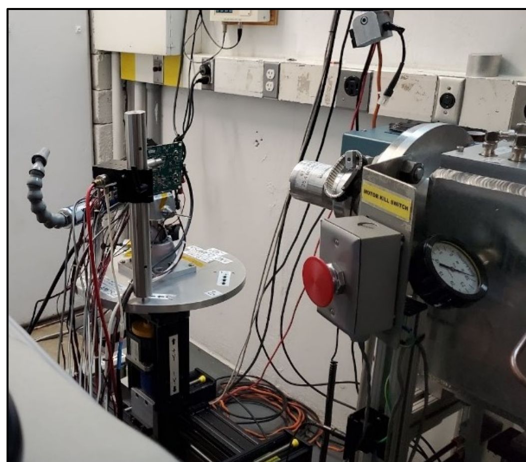

Figure 3. Angled View of the In-Air Test Station.

The PCB being tested in Figure 3 is located on the center of the test stand platter. The next mechanical system requirement is that the space between the microscope used for viewing and the tested PCB must be sufficiently large enough to fit a beam reduction device.

The system must also mount to the test stand platter, shown in Figure 4. The system will be mounted with bolts and has an upper weight limit of 100 lbs.

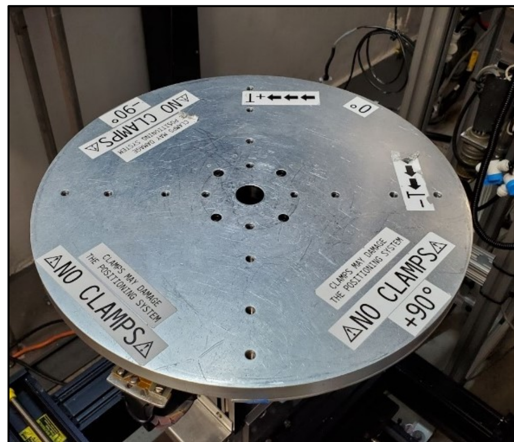

Figure 4. Test Stand Platter.

Figure 4 also shows the pattern of the bolt holes that will need to be transferred to the system for accurate alignment with the test stand platter.

2.1.2. Motion System Requirements

To successfully position the PCB, pinhole, and microscope for alignment, the system must have the capability to move these components in certain axes. Figure 5 shows a view of the in-air test station with the X, Y, and Z axes for reference.

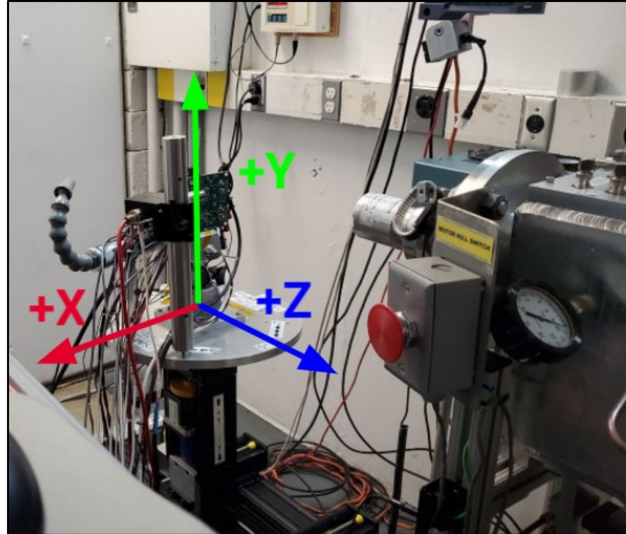

Figure 5. Annotated View of the In-Air Test Station.

The PCB must be able to move along the X, Y, and Z axes, as shown in Figure 5. The pinhole frame and microscope must be able to move in the X axis. Based on the various diameters of the pinholes in the pinhole frame, the incremental motion required is less than 5µm. Additionally, a requirement for static stability has been defined as less than 5µm of motion in any axis while the system is not moving. This requirement applies to the PCB, pinhole, and microscope.

2.2. Microscopy

To successfully image an IC and align the pinhole with the region of interest on an IC, TI has given information that led to derived system requirements. After defining these requirements, background information on important terminology and characteristics of microscope systems will be provided. This background information is vital to understand for the selection of a microscope system configuration that meets the system's requirements.

2.2.1. Microscope System Requirements

The diameters of the pinholes on the beam reduction devices are 25, 50, 100, 200, 300, 400, and 500µm. This leads to a derived system requirement of the microscope having a field of view (FOV) greater than 500µm. TI uses small metal and silicon traces on the IC as landmarks when viewing the PCB under a microscope. These traces are greater than or equal to 1µm in width. The microscope system must be able to effectively image these features. As a design consideration, the space between the microscope and PCB must be large enough to fit a pinhole mount, an air gap, and the height of an IC. This spatial requirement affects the acceptable working distance (WD) of the microscope, and it has been set at 6mm. The WD of each objective on the microscope must be greater than 6mm.

To enable remote imaging, the microscope must have a live streaming camera and motorized focus. This motorized focus must have a magnitude of incremental motion that is smaller than the depth of field of the objective with the highest magnification. The other motion requirement for the microscope is that it must have a large range in the X-axis, with incremental motion less than 500µm. This allows the microscope to be moved out of the way of the beam line for radiated tests.

The footprint of the microscope must be minimized along the Z-axis (optical axis) and along the X-axis in the +X direction. Finally, the distance from the top of the test stand platter to the optical axis in the Y-axis must be less than 13”, which is the current range of motion of the test stand platter.

2.2.1.1.1. The Traditional Upright Microscope

A diagram of a traditional upright microscope can be used as a starting point for the development of a microscope system for the given requirements. Figure 6 shows an annotated view of a traditional upright microscope.

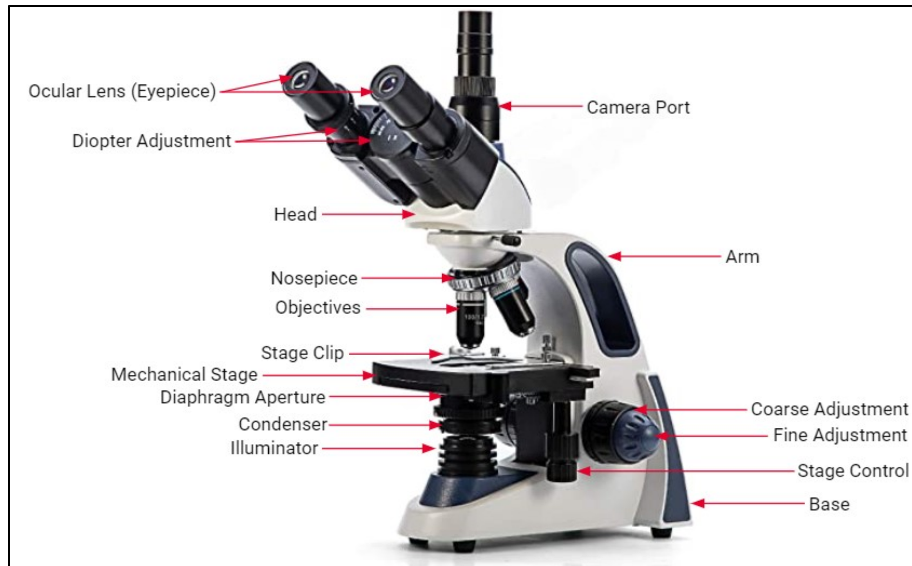

Figure 6. Traditional Upright Microscope [16].

The microscope pictured above uses a trinocular head to accommodate a camera and two eyepieces. It also has a stage assembly mounted to the base of the microscope. This stage has the ability to move up and down through the use of the coarse and fine adjustment knobs. The pictured microscope uses a lighting technique called transmitted illumination. Transmitted illumination relies on thin samples to transmit light through a sample. The light is then collected by the objectives on the microscope once it has travelled through the sample.

Some changes are required from the traditional upright microscope. The first change is that the eyepiece is not necessary, as the microscope will be used remotely. Additionally, the use

case is incompatible with transmitted light, so reflected light will be used. The microscope must have the ability to move away from the stage enough to be outside of the 1" radiation beam diameter. Finally, motorized focus is required for remote operation. A diagram of the reflected light microscopy is shown in Figure 7.

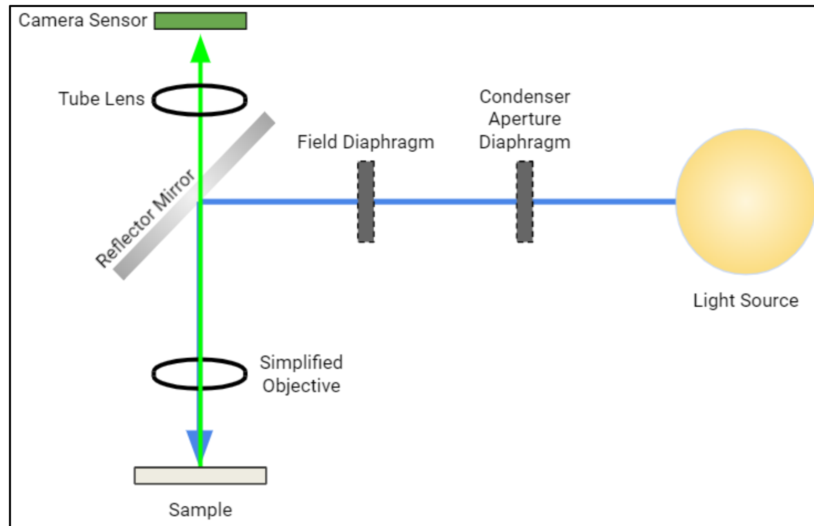

Figure 7. Reflected Light Microscopy.

The light travels from the light source to a half-mirror, or reflector mirror, through a condenser aperture diaphragm and field diaphragm. The light is reflected 90° to the optical axis by the mirror. The light is then focused to the focal plane by the objective, where it can illuminate the sample. After making contact with the sample, light is reflected from the sample and collected by the objective. The light passes through the reflector mirror, focusing on the camera sensor through the tube lens.

2.2.2. Important Terminology in Microscopy

There are several characteristics and parameters that describe how a microscope objective functions. The following characteristics are taken into account when selecting a series of microscope objectives to comply with system requirements.

2.2.2.1. Numerical Aperture and Focal Plane

Figure 8 shows an annotated diagram of the cross-sectional views of low and high magnification objectives to illustrate the concepts of numerical aperture (NA) and focal points.

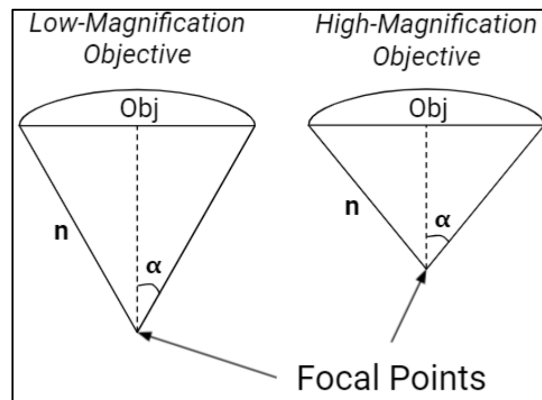

Figure 8. Numerical Aperture and Focal Point Diagram

Numerical aperture can be described as an objective's ability to gather light. This unitless parameter is measured in terms of $\boldsymbol{n}$ and $\boldsymbol{\alpha}$. The equation for numerical aperture is found below.

$$NA = \boldsymbol{n} \times \ \mathbf{sin}(\boldsymbol{\alpha})$$

$\boldsymbol{n}$ is the refractive index of the viewing medium transition. The values of $\boldsymbol{n}$ for the transition from the quartz of the objective lens to air, water, and oil immersion are 1.0003, 1.11, and 1.47, respectively. $\boldsymbol{\alpha}$ is the half-angle of the light cone, measured at the focal point, as illustrated in Figure 8. The focal point is where the light from an objective is ideally and radially

refracted to a single point. As seen in Figure 8, objectives with higher magnifications have larger values of $\boldsymbol{\alpha}$, and thus, have a larger NA [17]. Given similar nominal magnifications, the NA may vary due to differences in lens construction and geometry. Selecting the right NA for an objective is important, as it drives parameters such as working distance, resolve limit, and depth of field. The viewing medium for the application in this research is air, so a value of 1.0003 is used for $\boldsymbol{n}$ in calculations.

2.2.2.2. Theoretical Resolving Limit

The theoretical resolving limit of an objective is defined as the smallest discernable feature size. This parameter is measured in terms of λ and NA. The equation used for resolve limit is found below.

$$Resolve\ Limit = \frac{0.61\lambda}{NA}$$

Since the application for this research uses visible light, the resolve limit can be defined as a range, based on the upper and lower limits of the wavelengths of visible light. For calculations, the range is 380nm to 700nm. Given a constant NA, the resolve limit using shorter wavelengths of light is lower. Given a constant wavelength, the resolve limit of higher NA objectives is also lower. As the definition incorporates the concept of discernability, the equation is derived from a criterion known as the Rayleigh Criterion [17]. This criterion defines a standard for resolve limit in diffraction-based systems. This criterion uses the Airy Pattern shown in Figure 9.

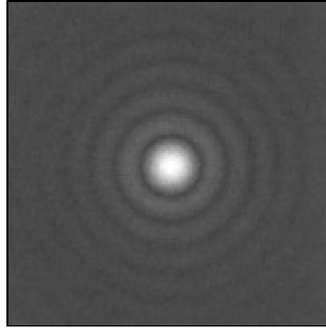

Figure 9. Airy Pattern [18].

The Airy Pattern, defined by Robert Airy, is a diffusion pattern created by perfectly circular apertures. The pattern can be described by the point spread function (PSF). The Rayleigh Criterion defines resolve limit as the smallest viable separation between two Airy Patterns that can be distinguished. The resolve limit of an objective has effects for the oversampling rate of the camera sensor, the practical use of the microscope, and the minimum discernible feature size on an IC.

2.2.2.3. Working Distance

The working distance (WD) of a microscope is the distance from the pinnacle of a lens to its focal point, as shown in Figure 10.

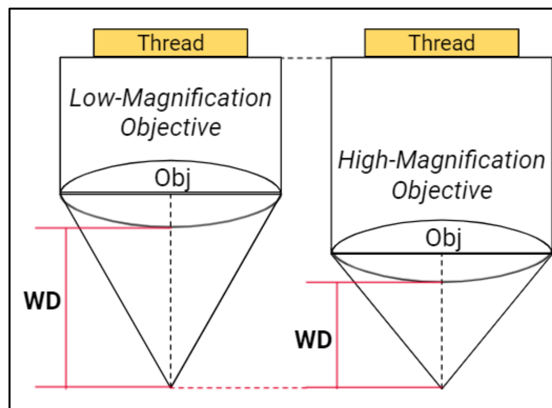

Figure 10. Working Distance Diagram

The working distance of a single lens is described by the equation below, where $\boldsymbol{a}$ is the distance from the center of the lens to its image plane [19].

$$Theoretical\ WD = \boldsymbol{a} \times Magnification$$

While the equation defines the WD, the WD of an objective is much more challenging to calculate, as the calculation must be performed for each lens in an objective. This can be difficult or even impossible to perform because of the high lens count and proprietary nature of objective design. Additionally, the WD of an objective is affected by lens construction and any aberrations present in the objective. This does not pose an issue, as objective manufacturers report the working distance of their objectives. The overall trend in WD is that higher magnification objectives have shorter working distances. Given a constant magnification, an objective with a higher NA will have a higher working distance.

An additional consideration for design is the parfocal length of an objective. This parameter is the distance from the seat of the thread to the lower point of the working distance. A series of standardized parfocal objectives has the same parfocal distance across all objectives. This means that, when transitioning from one objective to the next, focusing the highest magnification objective brings all objectives into focus. This has the effect of reducing time required to focus on the sample in question.

2.2.2.4. Field of View

Field of view (FOV) is the diameter of the sample visible, as shown in Figure 11.

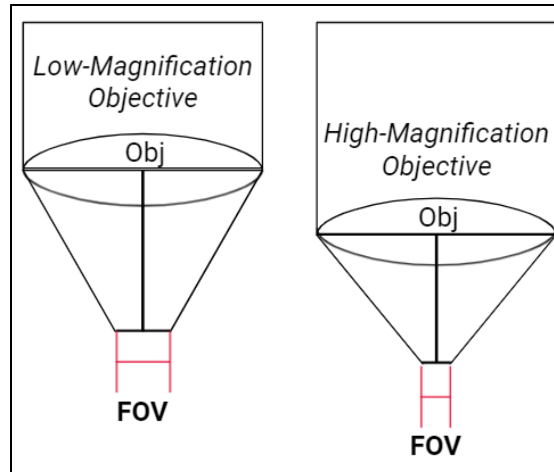

Figure 11. Field of View Diagram

While the circular FOV of a microscope is useful to define when using and eyepiece, the use of a digital camera introduced the need to incorporate the camera's sensor in the calculation. The dimensions of the FOV after the camera can be described by the equations below.

$$FOV_W = \frac{Sensor_W}{(M_{OBJ} \times M_{TUBE})}$$

$$FOV_H = \frac{Sensor_H}{(M_{OBJ} \times M_{TUBE})}$$

The effective FOV is affected by the magnification of the objective and tube lens, as well as the sensor size. This calculation affects the selection of objectives and the maximum feature size that can be imaged. As seen in Figure 11, an objective with higher magnification has a smaller FOV than an objective with lower magnification.

2.2.2.5. Depth of Focus

Depth of focus (DOF) is the distance along the optical axis between the closest and furthest planes in focus. The concept of DOF is illustrated by Figure 12.

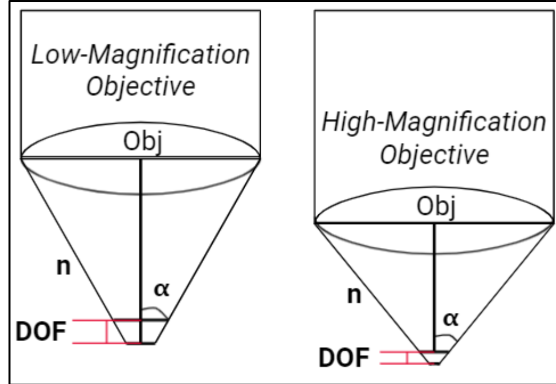

Figure 12. Depth of Focus Diagram

DOF is measured in terms of the wavelength of light used, the refractive index, and the NA. It is described by the equation below.

$$DOF = \frac{\lambda\sqrt{n^2 - (NA)^2}}{(NA)^2}$$

DOF is affected by the wavelength of light used and the NA of the objective [20]. It affects the focusing resolution requirement of the system and the depth of sample capable of being imaged. The DOF of an objective with higher magnification is smaller than the DOF of an objective with lower magnification, as shown in Figure 12.

2.2.2.6. Total Magnification

The total magnification of a microscope system is defined as the product of the magnifications of individual magnifying components. The equation for total magnification is shown below.

$$Total\ Magnification = M_{OBJ} \times M_{TUBE} \times M_{DISP}$$

The magnifying components in a typical microscope are the objective, tube lens, and ocular lens (eyepiece). For digital imaging, the magnification of the ocular lens can be substituted for the magnification of the display. The magnification of the display is defined as the

ratio between the pixel count and sensor size of the camera sensor to the pixel count and size of the display being used. This is affected by the display used, which will not be smaller than the camera's sensor. Some resolution may be lost if the pixel density of the display is lower than the pixel density of the camera sensor.

2.2.2.7. Aberrations and Their Corrections

An aberration is a non-ideality in a lens system. Pertinent aberrations for this system can be placed into two categories, with the first being lens-based or light-based aberrations.

2.2.2.7.1. Lens-based and Light-based Aberrations

The first aberration is spherical aberration, which is lens-based. Figure 13 shows an annotated diagram illustrating spherical aberration.

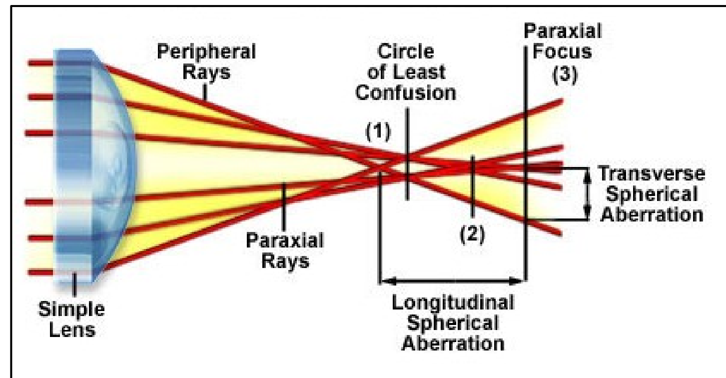

Figure 13. Spherical Aberration [21].

Peripheral rays are the rays of light that intersect with a lens at the largest diameter, when measured radially from the center of the optical axis. Paraxial rays are all rays that fall inside the peripheral rays These rays are grouped by their radial distance from the center of the optical axis. A non-zero distance along the optical axis between the focal point of the paraxial rays and the focal point of the peripheral rays results in a longitudinal spherical aberration, while a non-zero

radial distance from the optical axis between these two points results in a transverse spherical aberration. The cross-sectional plane where longitudinal and transverse spherical aberrations are minimized is described as the Circle of Least Confusion. These aberrations affect the DOF and FOV, as they alter the paths of rays of light entering and exiting the lens.

Lenses with high NAs are particularly affected by spherical aberrations. The corrections for this type of aberration are tight lens fabrication tolerances and additional lenses within a single objective. These additional lenses help to bend light rays in a more optimal path. The industry-standard term for this type of correction is Super Apochromat correction.

The second aberration is chromatic aberration, which is light-based. Figure 14 shows an annotated diagram illustrating spherical aberration.

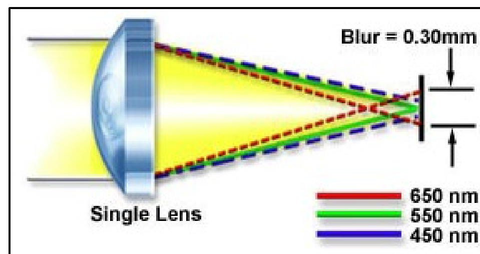

Figure 14. Chromatic Aberration Diagram [21].

A chromatic aberration is a wavelength-dependent color blur caused by using a spectrum of light, instead of a single wavelength. Different wavelengths of light refract at different angles, which causes the focal points to differ along the optical axis. The correction for chromatic aberrations is an Achromat or Semi-Apochromat correction. Similar to the Super Apochromat correction, the Achromat and Semi-Apochromat corrections use additional lenses to bend light in a more optimal path.

2.2.2.7.2. Lens Fabrication Aberrations

Aberrations can also be introduced with varying qualities and tolerances of lens fabrication. The first of these aberrations is an astigmatism, which is characterized as vertical or horizontal blur. This aberration is caused by non-uniform lens construction or imperfect alignment of a lens inside of an objective. Figure 15 shows an illustration of this aberration.

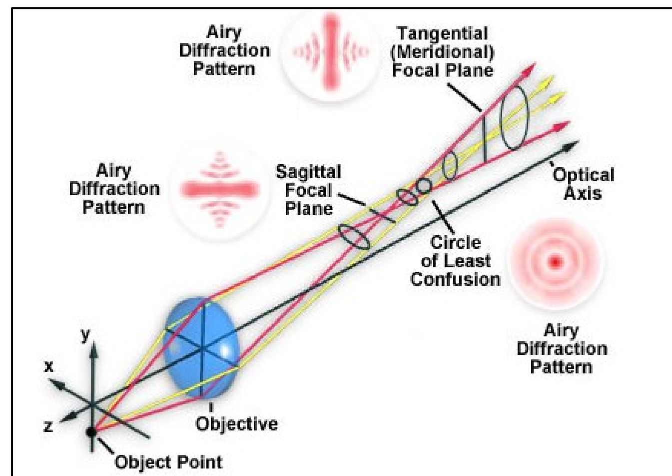

Figure 15. Astigmatism Aberration [21].

Astigmatism aberrations can be horizontal or vertical. The horizontal astigmatism is shown by the non-zero distance between the sagittal focal plane and the Circle of Least Confusion. The vertical astigmatism is shown by the non-zero distance between the tangential focal plane and the Circle of Least Confusion. The correction for astigmatism is tight lens and objective fabrication tolerances.

The second type of lens fabrication aberrations is field curvature. This is characterized by a non-planar focal plane and can be corrected with tight lens fabrication tolerances.

The third type of lens fabrication aberrations is comatic aberration. Comatic aberrations result in a comet-like blur originating from a single point of light. Figure 16 shows an illustration of a comatic aberration.

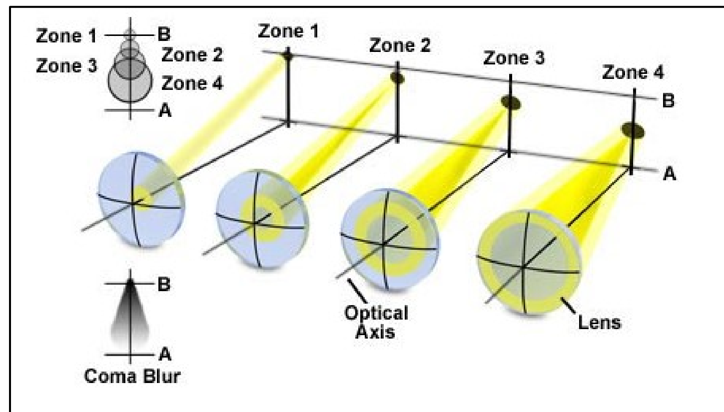

Figure 16. Comatic Aberration [21].

A comatic aberration occurs when the lens has a linear shift in the focal plane for rays intersecting with the lens at different radii away from the optical axis. This aberration can also be corrected with tight lens fabrication tolerances.

2.2.3. Motorized Focus

The microscope system must incorporate motorized focus. The act of focusing a microscope is simply varying the distance between the objective and sample being imaged. This requirement triggered a question of whether the motorized focus should be built or bought. Several potential solutions were identified in the research process. Because of the horizontal orientation required by the design, the purchased solution must be able to operate in a horizontal orientation. Additionally, the microscope system must be modular, as the stage of a traditional microscope is not necessary for the application in this research. The first potential solution was

to purchase a microscope system that incorporated motorized focus. This solution has some drawbacks, as most of the commercially available modular microscope systems with motorized focus are gravity-dependent. The motorized focus mechanisms of these microscope systems only provided a force upward along the optical axis, pushing the objective to a point further from the sample being imaged. To bring the objective closer to the sample being imaged, the focus mechanism would retract downward, allowing gravity to provide a force sufficient to allow the objective and head of the microscope to slide downward. While this mechanism works when the optical axis is oriented vertically, it does not work for a horizontally oriented microscope, as required in this application.

Looking past gravity-dependent systems, there are systems that effectively focus in a horizontal orientation. These systems are very costly (> $50,000) and low in modularity. An example of such a system, the Olympus DSX1000, is shown in Figure 17.

Figure 17. Olympus DSX1000 [22].

The optical solution shown in Figure 17 has the capability necessary for horizontal orientation, but comes with a large footprint. Based on footprint and size constraints, the need for

a more compact design was identified. This need is typically met with an optical system called a stereoscope, as shown in Figure 18.

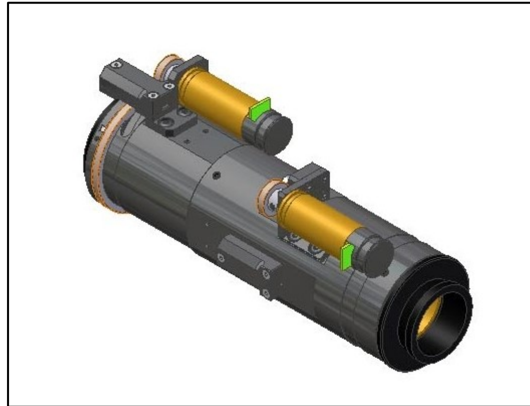

Figure 18. Navitar 12X Stereoscope [23].

Stereoscopes have a compact design around the optical axis. While this concept may seem attractive at first, stereoscopes come with two main disadvantages. They are not compact along the optical axis and typically have low magnification capabilities. Even though the theoretical resolve limit may fall within the required range, the lack of the ability to switch objectives, and thus, fields of view, eliminated stereoscopes as a viable option.

With purchasing a microscope system that incorporates motorized focus have impracticalities and failures for system requirements, the concept of replicating the motorized focus mechanism is the best option. To replicate the mechanism, a linear motion stage may be used. It is important to note that the incremental focusing motion along the optical axis must be smaller than the DOF of the objective with the highest magnification. This ensures that the entire range of the depth of the sample being imaged may be brought into focus. Figure 19 illustrates this concept.

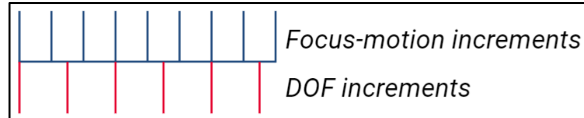

Figure 19. Optical Axis Incremental Motion versus DOF Increment Concept Diagram.

Given a specific focal point, as shown in Figure 19 by the red lines, the focus-motion increment may be positioned at a given line in the set of blue lines that allows the entire DOF to be achieved, overlapping the next focus-motion increment within the same DOF increment.

2.3. Motion Systems

Various motion systems were considered to meet system requirements. The motion system must be sufficiently modular enough to be used as a building block in the system. It also must be capable of meeting requirements for footprint, resolution of motion, and range. The first set of motion stages found in the survey of available options was a set of linear motion stages supplied by PI USA. Figure 20 shows an example of one of their stage options.

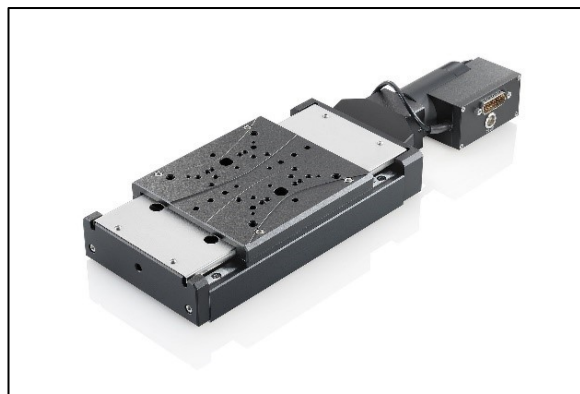

Figure 20. Linear Motion Stage from PI [24].

The linear motion stage shown above is well-suited for precise motion control, but the available ranges of motion did not allow for much scalability in terms of PCB size. Additionally,

these highly-precise motion stages came at a high price that was incompatible with the budget constraints of the research. Each axis costs more than $3,000 and a control module costing over $4,000 is required for the system. As the need for absolute positioning accuracy was not a system requirement, stages similar in capability to the stage above included more capability in absolute positioning accuracy than required.

The next set of motion stages identified is similar in concept, but includes less absolute positioning accuracy, higher travel ranges, and a much lower cost. The stages vary in their reinforcement scheme, but all other design features are relatively similar. The stages in question use a frame of aluminum extrusion, a stepper motor for control, and a stage built around a ball screw. A ball screw uses a ball-bearing housing, as shown in Figure 21, to cycle ball-bearings around a lead screw.

Figure 21. Ball Screw Cutaway Illustration [25].

When the ball-bearing housing is isolated from rotating with the lead screw through the use of a stage, rotating the lead screw results in motion along the long axis of the lead screw. There are three main methods to isolate the ball-bearing housing from rotation. The first, as shown in Figure 22, is by connecting the stage to roller bearings that roll along a precision rod.

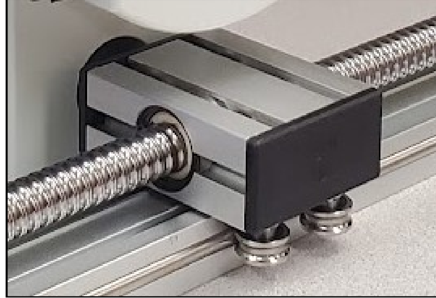

Figure 22. Roller Bearings on Stage in Contact with Precision Rod.

As the lead screw rotates, the rotation of the ball-bearing housing is limited by the contact of the roller bearings with the precision rod along the side of the aluminum frame. The second method used to ensure linear motion of the stage is through the use of cycling bearings along precision rods, as shown in Figure 23.

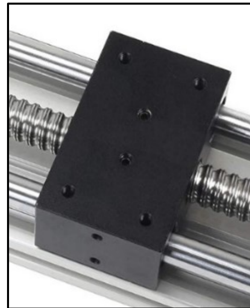

Figure 23. Precision Rods with Cycling Bearings [26].

As the lead screw rotates, the rotation of the stage is limited by the centering of two ports in the stage. The centering is made possible by cycling bearings inside the ports making contact with the precision rods that are positioned inside the ports.

The third method of limiting rotation is through the use of a linear slide rail, pictured in Figure 24.

Figure 24. Linear Slide Rail.

Linear slide rails operate with cycling bearings rolling along the rail inside the stage. To use linear slide rails to eliminate rotation of a stage on a linear motion rail, a bracket may be added that connects the stage of the linear motion rail to the stage of the linear slide rail. This mechanically couples the motion of the stage of the linear stage rail with the stage of the linear slide rail, increasing stability.

To calculate the expected linear travel distance motion of a ball-screw stage, the following equation can be used.

$$Linear\ Travel\ Distance = \ Thread\ Pitch\ \times Revolutions$$

With the motion of the linear stage rails being controlled by stepper motors, some background information on the control of these stepper motors is required.

2.4. Stepper Motor Control

Stepper motors rotate at a predetermined angle per pulse of current allowed. A standard stepper motor travels 1.8° per step, giving 200 full steps per full rotation. The current is applied to a set of coils inside the stepper motor that, when energized, align a rotor with a stator fixed to the motor case. A technique called micro-stepping can be used to step the motor at lower intervals than that of the nominal angular step. This micro-stepping technique applies a specific amount of current to each coil that allows the rotor and stator to be aligned at positions other than

a 180° magnetic pole difference. While requiring more current to result in similar static holding forces to a full step, micro-stepping can greatly increase the rotational resolution of a stepper motor.

Stepper motor drivers are used to amplify normal pulse-width modulated (PWM) signals at a logic level voltage into pulses that have sufficient power to move the rotor of a stepper motor under a load. When combined with a stepper motor that has the ability to micro-step, a micro-stepping motor driver can be set at various increments of rotational motion per step to result in finer resolution of rotational motion. This technique is employed in the design of the system to reach the motion resolution requirement of the system.

3. SYSTEM ARCHITECTURE

3.1. Microscope

After considering all of the characteristics described in section 2.2, as well as modularity, footprint, software compatibility, and cost, a survey of solutions was conducted. The microscope manufacturers included Thorlabs, Nikon, Navitar, Olympus, and Zeiss. Ultimately, the BXFM System from Olympus was selected for use in the system.

3.1.1. Olympus BXFM

The Olympus BXFM System is a microscope system that has high modularity, as it allows customers to select from an original equipment manufacturer's (OEM) catalog to customize the design of the system. All components for this system were carefully selected from the OEM catalog to meet system requirements for optics. Figure 25 shows an angled rear view of the microscope system as designed.

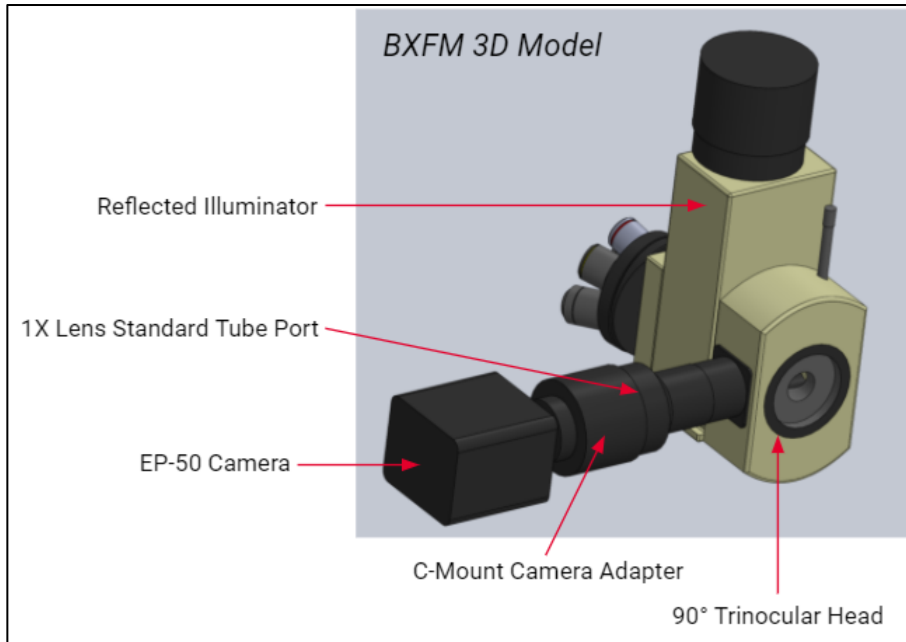

Figure 25. Annotated 3D Model of the BXFM System – Angled Rear View.

The BXFM system pictured in Figure 25 first shows the reflected illuminator. This reflected illuminator meets the system requirement for reflected illumination and helps to minimize the footprint in both the optical axis and the +X direction. The 90° trinocular head allows the resulting image to be reflected away from the optical axis, minimizing the footprint along the optical axis. The trinocular head mates with a standard tube port and integrated 1X lens. This tube port length is described as standard because it matches the required length for the objectives with no additional magnification. The tube port mates with a camera adapter with its own 1X lens to maintain image size. Lastly, the EP-50 camera mates with the camera adapter to provide the required live streaming capability.

Figure 26 shows an angled front view of the BXFM System.

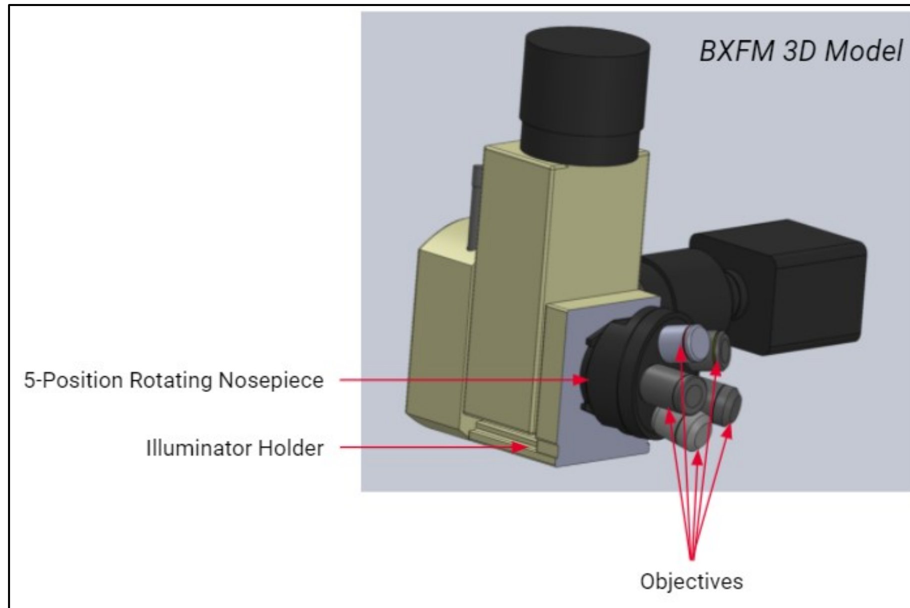

Figure 26. Annotated 3D Model of the BXFM System – Angled Front View.

Figure 26 first shows the 5-position rotating nosepiece, which is mounted to the illuminator holder. The nosepiece holds all of the five objectives, which have nominal magnification ratings of 5X, 10X, 20X, 50X, and 100X. The selection of objectives and their properties is covered in the following section.

3.1.2. Objectives

The main driving factors for selection of objectives were system compatibility, WD, FOV, resolving limit, and aberration correction. The detailed explanation of these parameters will start with the lowest magnification objective and move up to the highest magnification objective.

3.1.2.1. 5X Objective – MPLN5X

This 5X objective is part of Olympus' Plan Achromat Series. Figure 27 shows a mechanical drawing of the objective.

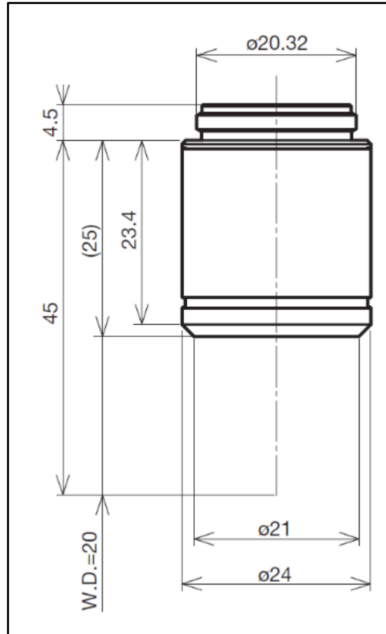

Figure 27. Mechanical Drawing of the MPLN5X Objective [27].

The 5X objective has a NA of 0.1, a focal length of 36mm, and a WD of 20mm. The objective features Achromat correction for chromatic aberrations. The theoretical FOV has been calculated to be 1244.16µm × 933.12µm after the sensor's reduction. This allows for a 500µm or 400µm pinhole to fit within the FOV, while filling most of the image. The theoretical resolve limit was calculated to be between 2.32µm and 4.27µm, based on the wavelength range of the visible spectrum.

3.1.2.2. 10X Objective – LMPLFLN10X

This 10X objective is part of Olympus' long working distance Plan Semi-Apochromat Series. Figure 28 shows a mechanical drawing of the objective.

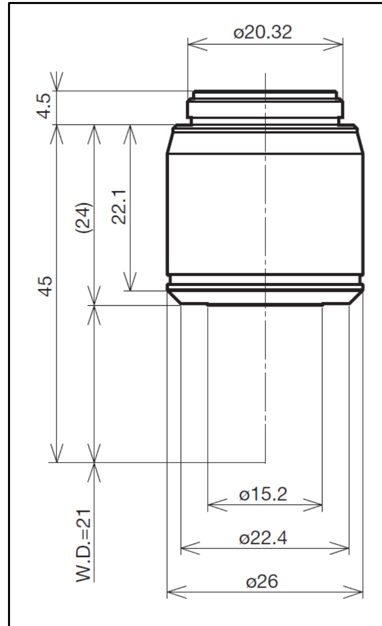

Figure 28. Mechanical Drawing of the LMPLFLN10X Objective [27].

The 10X objective has a NA of 0.25, a focal length of 18mm, and a WD of 21mm. The objective features Semi-Apochromat correction for chromatic aberrations. The theoretical FOV has been calculated to be 622.08µm × 466.56µm after the sensor's reduction. This allows for a 300µm or 200µm pinhole to fit within the FOV, while filling most of the image. The theoretical resolve limit was calculated to be between 0.93µm and 1.07µm, based on the wavelength range of the visible spectrum.

3.1.2.3. 20X Objective – LMPLFLN20X

This 20X objective is part of Olympus' long working distance Plan Semi-Apochromat Series. Figure 29 shows a mechanical drawing of the objective.

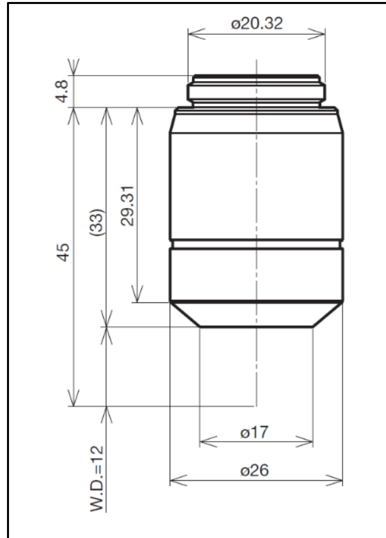

Figure 29. Mechanical Drawing of the LMPLFLN20X Objective [27].

The 20X objective has a NA of 0.4, a focal length of 9mm, and a WD of 12mm. The objective features Semi-Apochromat correction for chromatic aberrations. The theoretical FOV has been calculated to be 311.04µm × 233.28µm after the sensor's reduction. This allows for a 100µm pinhole to fit within the FOV, while filling most of the image. The theoretical resolve limit was calculated to be between 0.58µm and 1.065µm, based on the wavelength range of the visible spectrum.

3.1.2.4. 50X Objective – LMPLFLN50X

This 50X objective is part of Olympus' long working distance Plan Semi-Apochromat Series. Figure 30 shows a mechanical drawing of the objective.

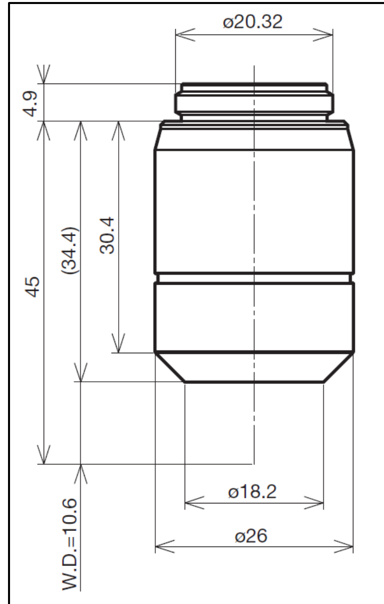

Figure 30. Mechanical Drawing of the LMPLFLN50X Objective [27].

The 50X objective has a NA of 0.5, a focal length of 3.6mm, and a WD of 10.6mm. The objective features Semi-Apochromat correction for chromatic aberrations. The theoretical FOV has been calculated to be 124.24µm × 93.31µm after the sensor's reduction. This allows for a 50µm pinhole to fit within the FOV, while filling most of the image. The theoretical resolve limit was calculated to be between 0.46µm and 0.85µm, based on the wavelength range of the visible spectrum.

3.1.2.5. 100X Objective – SLMPLN100X

This 100X objective is part of Olympus' super-long working distance Plan Apochromat Series. Figure 31 shows a mechanical drawing of the objective.

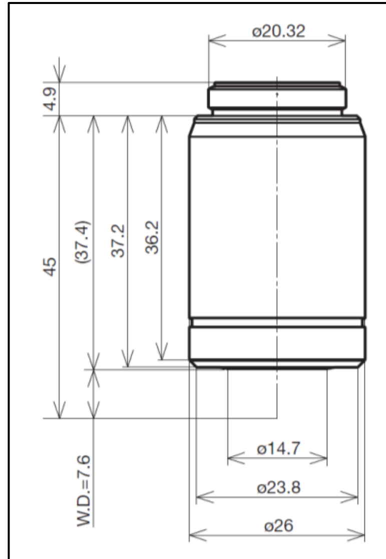

Figure 31. Mechanical Drawing of the SLMPLN100X Objective [27].

The 100X objective has a NA of 0.6, a focal length of 1.8mm, and a WD of 7.6mm. This WD meets the system requirement of a WD greater than 6mm. The objective features Apochromat correction for chromatic aberrations. The theoretical FOV has been calculated to be 62.21µm × 46.66µm after the sensor's reduction. This allows for a 25µm pinhole to fit within the FOV, while filling most of the image. The theoretical resolve limit was calculated to be between 0.38µm and 0.71µm, based on the wavelength range of the visible spectrum.

3.1.2.6. Objective Series Considerations

All aforementioned objectives have planar correction, which ensures minimal curvature of the focal plane. Additionally, all objectives have the same parfocal distance. This reduces focusing time by allowing all objectives to be in focus when the objective with the highest magnification has been focused. Figure 32 shows an illustration of this concept.

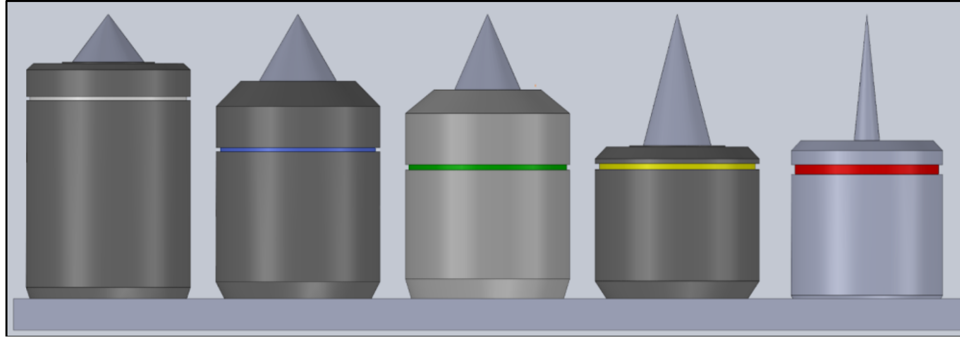

Figure 32. Parfocal Objective Series.

Figure 32 includes all objectives, starting with the 100X on the left and ending with the 5X on the right. The gray cones represent the light cones of each objective, with the height of each cone representing the working distance. The apex of each cone is the focal point of each objective. This illustration shows that the parfocal distances of all objectives in the series are the same.

3.2. Mechanical and Motion Components

A set of the mechanical and motion components were selected collaboratively with the researcher working on the pinhole portion of this project. This was done because of the collaborative nature of the project. The pinhole frame, PCB/pinhole group bracket, and PCB mount were all designed by Dylan Blezinger. Collaboration on this section of the project was necessary, as many factors of this portion of the project impact and relate to factors of the other portion of this project. Though the entire set of mechanical and motion components will be described in this section, the portion described above is the result of the work of the other researcher, Dylan Blezinger. Areas where my contribution was less than 100% of the work are clearly noted in this section.

As a first step to designing the system, the platter and beam port in the in-air test station were measured and digitized into a 3D model, accounting for the available motion range of the platter. The measurement and digitizing process was performed in a collaborative manner. Figure 33 shows the resulting 3D model.

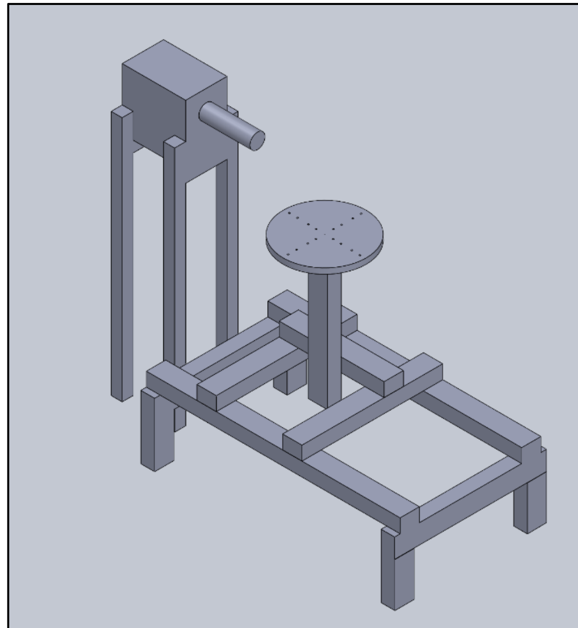

Figure 33. 3D Model of the In-Air Test Station.

The first mechanical component of the system is an adapter plate to mate the rest of the system components with the platter in the in-air test station. The design of this adapter plate was collaborative.

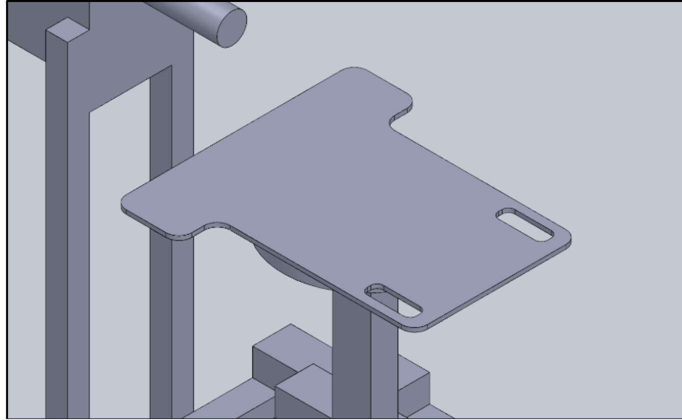
Figure 34. Adapter Plate.

The adapter plate is designed to be manufactured from a $^{3}/_{8}$" thick aluminum plate. The bolt holes from the platter of the in-air test station are transferred to this adapter plate, but are not shown in the figure. The adapter plate mounts to the platter with six $^{1}/_{4}$" – 20 bolts from the top of the adapter plate. The next set of components is the microscope linear motion rail, stabilizing linear slide rails, and stabilizing brackets. A view of these components can be seen in Figure 35.

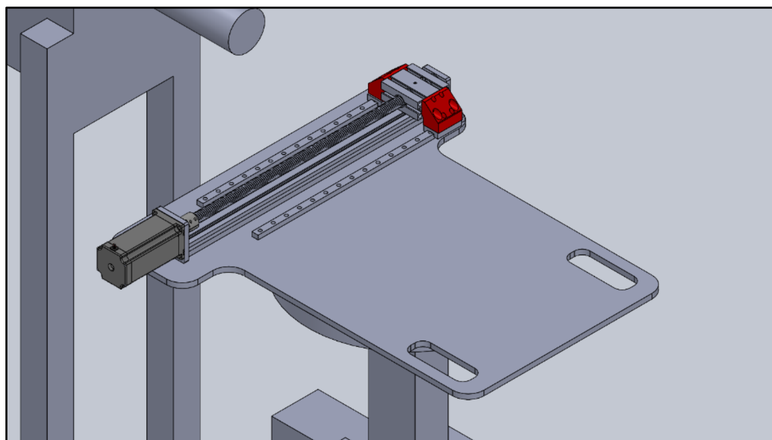
Figure 35. Microscope Linear Motion Rail, Stabilizing Linear Slide Rails, and Stabilizing Brackets.

The linear motion rail being used for the microscope has a travel range of 400mm and a thread pitch of 5mm. It is powered by a 24V stepper motor with 1.8° nominal steps. The stage is isolated from rotation by two roller bearings on each side of the stage, as shown in Figure 22. The rail mounts to the adapter plate with four M4 bolts through the underside of the adapter plate. These bolts seat into square T-slot nuts that are positioned inside the T-slot of the aluminum extruded frame. Two stabilizing linear slide rails, each with 400mm of travel, are bolted to the adapter plate with M3 bolts from the top. A picture showing the linear slide rail can be found in Figure 24. The stages of these linear slide rails are connected to the stage of the linear motion rail with 3D printed brackets. These slide rails and connecting brackets serve to increase the stability of the microscope linear motion stage. The next components to be added to the system are the microscope support bracket and BXFM Microscope System, as shown in Figure 36.

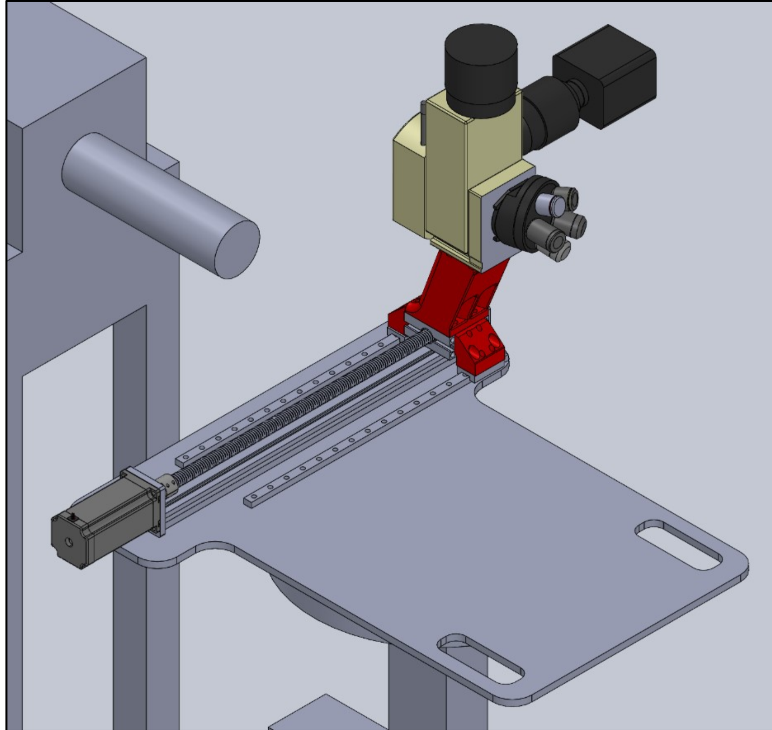

Figure 36. Microscope Support Bracket and BXFM Microscope System.

The large red bracket mounted to the top of the microscope linear motion stage is a 3D printed bracket. It serves to hold the BXFM Microscope System and raises the optical axis to the height of the center of the beam port. The next set of components includes the PCB/pinhole group linear motion stage rail, the stabilizing linear slide rails, and the supporting brackets, as shown in Figure 37. The design and selection process for this group of components was collaborative.

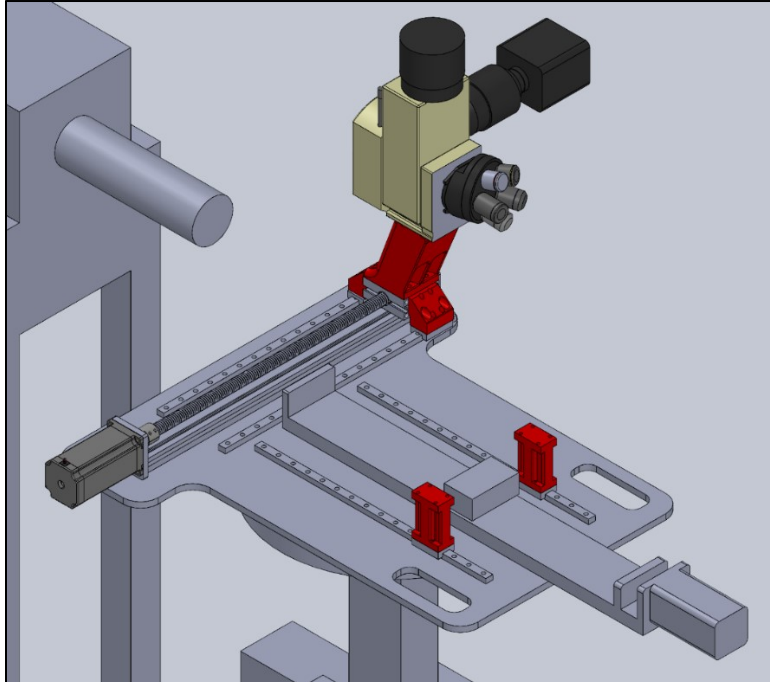

Figure 37. PCB/Pinhole Group Linear Motion Rail, Stabilizing Linear Slide Rails, and Brackets.

Figure 37 shows the addition of the PCB/pinhole group linear motion rail. This linear motion rail has a travel range of 500mm with a thread pitch of 5mm. It is also powered by a 24V stepper motor with 1.8° nominal steps. The stage is isolated from rotation by two cycling bearings, precision rods, and ports within the stage, as shown in Figure 23. The rail mounts to the adapter plate with eight M5 bolts through the underside of the adapter plate. Similar to the microscope linear motion rail, the bolts of the PCB/pinhole group rail seat into square T-slot nuts that are positioned inside the T-slot of the aluminum extruded frame. Two stabilizing linear slide rails, each with 400mm of travel, are bolted to the adapter plate with M3 bolts from the top. Two stabilizing brackets mount to the stages of the linear slide rails. These stabilizing brackets are 3D printed. The upper mating surface will be explained later in this section. The next set of components to be added includes the PCB/pinhole group bracket, the pinhole linear motion rail,

and the vertical manual pinhole adjuster. This group of components was designed and implemented by the other researcher, Dylan Blezinger, with input from the author. This portion of the work required collaboration because it represents the point at which the two areas of research intersect. This group of components is shown in Figure 38.

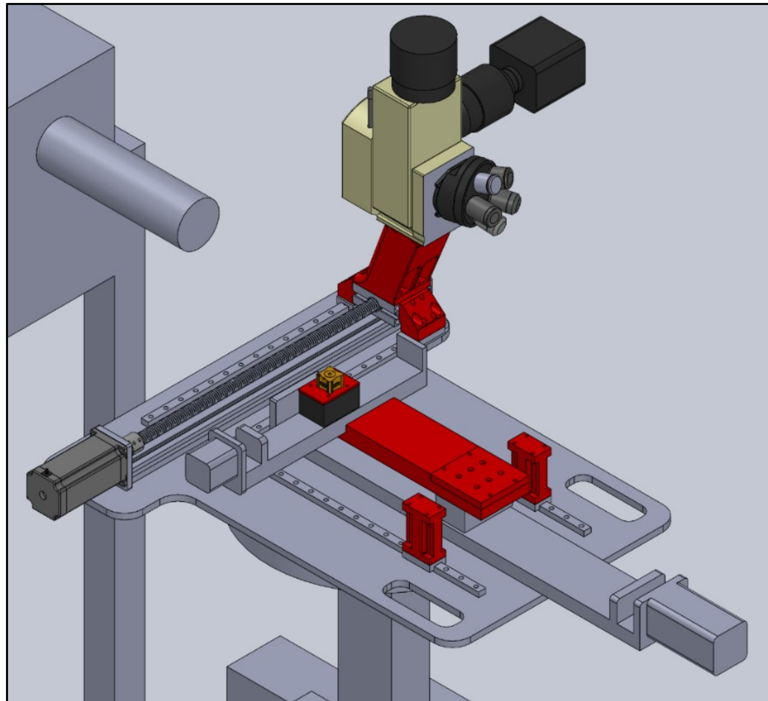

Figure 38. PCB/Pinhole Group Bracket, Pinhole Linear Motion Rail, and Vertical Manual Pinhole Adjuster.

The large red bracket mounted to the PCB/pinhole group linear motion stage in Figure 38 serves to hold the pinhole linear motion rail. This linear motion rail has a travel range of 200mm with a thread pitch of 4mm. It is also powered by a 24V stepper motor with 1.8° nominal steps. The stage is isolated from rotation by a single linear slide rail internal to the aluminum extruded frame. The adapting plate is the red part mounted to the top of the pinhole stage. The vertical manual pinhole adjuster is the gold part on top of the adapting plate. The purpose and

characteristics of this adjuster will be described in greater detail following Figure 39. Figure 39 includes the pinhole frame, horizontal PCB linear motion rail, and optical axis manual adjuster. The pinhole frame was designed and implemented solely by Dylan Blezinger. All other parts added in Figure 39 were designed and implemented in a collaborative manner.

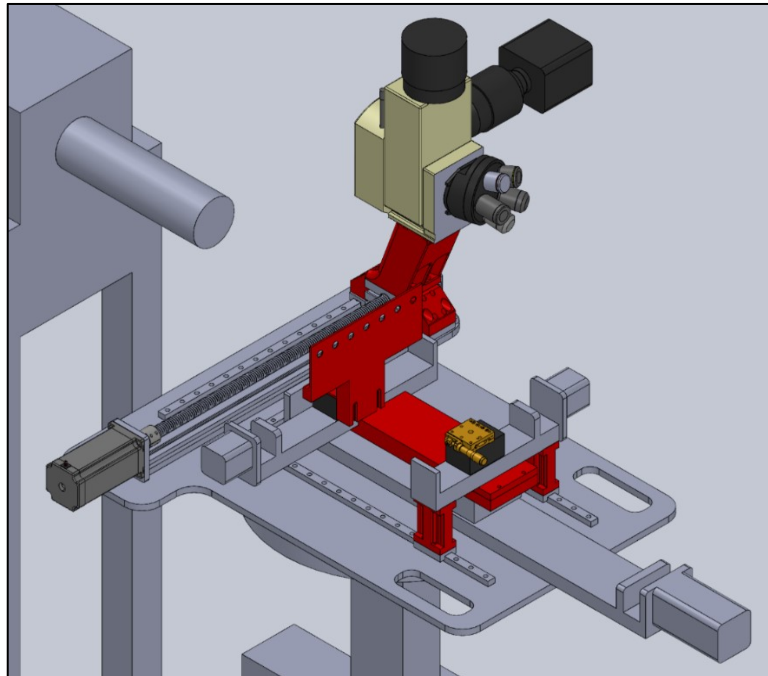

Figure 39. Pinhole Frame, Horizontal PCB Linear Motion Rail, and Optical Axis Manual Adjuster.

The pinhole frame is the large flat component with seven visible holes. This frame holds seven standard 1" circular apertures (pinholes) made by Lenox Laser. The pinhole frame is 2mm thick and has a designed height that allows the pinholes to be the same height as the optical axis. In the event that the manufacturing precision of the pinholes falls outside an acceptable range for viewing, the vertical pinhole manual adjuster, introduced in Figure 38, may be used to adjust the

vertical position of the entire pinhole frame. This manual adjuster is a screw-driven optical jack that has a total travel range of 3mm.

The horizontal PCB linear motion rail is mounted on top of the PCB/pinhole group bracket. This linear motion rail has a travel range of 100mm with a thread pitch of 4mm. It is also powered by a 24V stepper motor with 1.8° nominal steps, and it is also isolated from rotation by a single linear slide rail internal to the aluminum extruded frame. The rail is bolted to the two stabilizing brackets from the set of components added in Figure 37. This mechanical coupling serves to stabilize the PCB/pinhole group rail and the horizontal PCB rail.

On top of the stage of the horizontal PCB linear motion rail, an optical axis manual adjuster is mounted. The purpose and characteristics of this adjuster will be described in greater detail following Figure 40. Figure 40 includes the addition of the vertical PCB linear motion rail, the PCB mount, and the PCB. The PCB mount was designed and implemented solely by Dylan Blezinger. All other parts added in Figure 40 are designed and implemented in a collaborative manner.

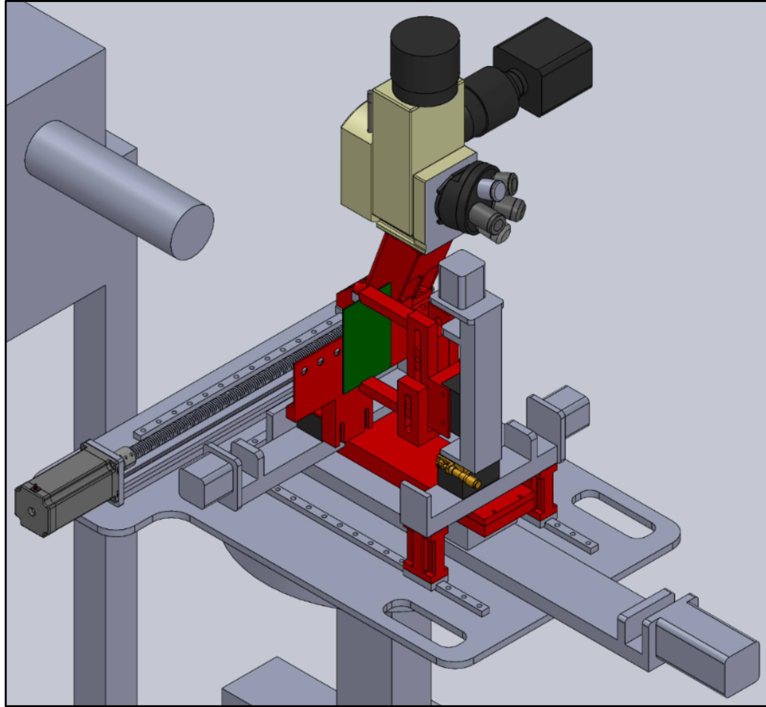

Figure 40. Vertical PCB Linear Motion Rail, PCB Mount, and PCB.

The vertical PCB linear motion rail is mounted on top of the optical axis manual adjuster. This linear motion rail also has a travel range of 100mm with a thread pitch of 4mm. It is also powered by a 24V stepper motor with 1.8° nominal steps, and is also isolated from rotation by a single linear slide rail internal to the aluminum extruded frame. The optical axis manual adjuster introduced in Figure 39 allows the user to manually adjust the distance between the PCB and the pinhole frame to the desired location. This manual adjuster has a travel distance of 16mm. The PCB mount is mounted to the stage of the vertical PCB linear motion rail. It holds a range of PCB sizes for testing, allowing enough space between the back side of the PCB and the vertical PCB linear motion rail to make test setup connections for power, logic, and measurement.

Figure 40 represents the full mechanical, motion, and optics system. The next section consists of the validation of system design requirements through measurements taken in SolidWorks.

3.2.1. Clearance Verification

Before moving to implementation of the system, it was necessary to validate that the design met system requirements of mechanical clearance. Figure 41 illustrates the first of such clearance verifications.

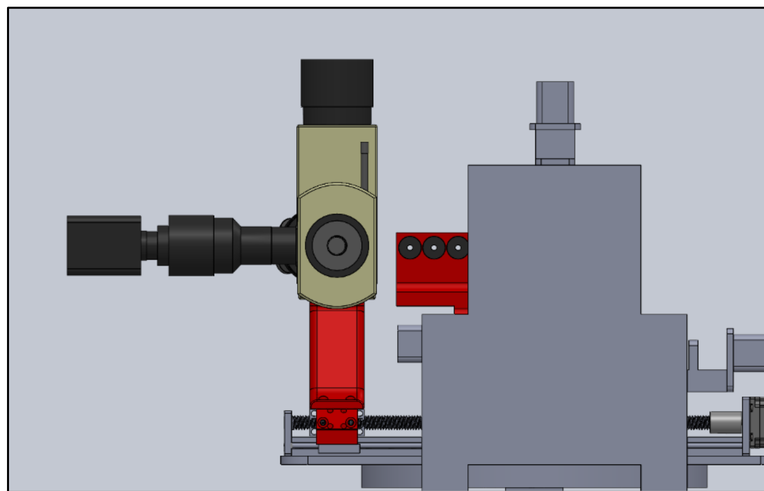

Figure 41. Pinhole/Microscope Clearance – Beam Port View.

Figure 41 shows the system's ability to position the microscope and pinhole frame in a way that the pinhole frame can clear the microscope along its path toward the beam port. This system requirement allows the microscope to be fully moved out of the path of the pinhole frame, which must extend to less than 40mm away from the opening of the beam port. Figure 42 shows this 40mm system requirement being met through a side view of the system.

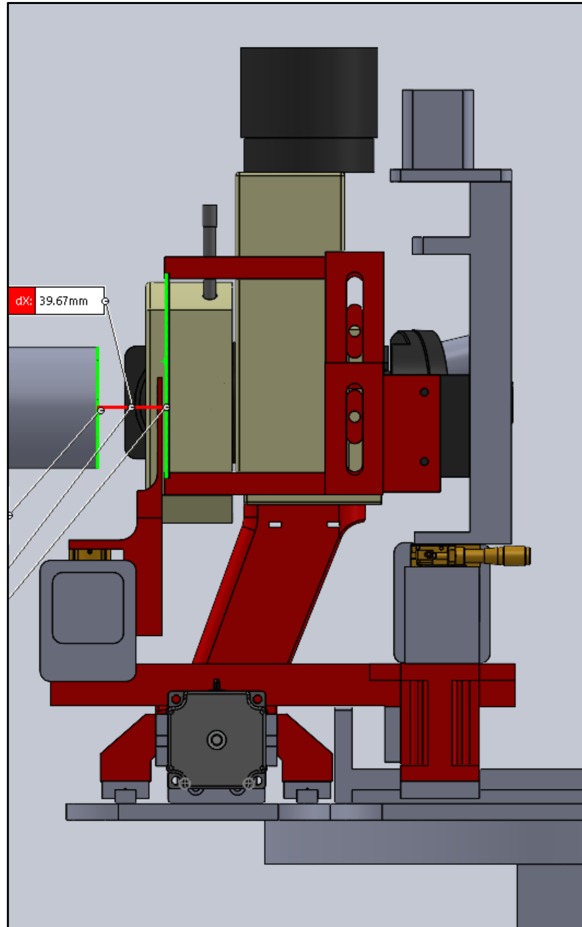

Figure 42. PCB's Ability to Reach <40mm to Beam Port.

Figure 42 is a side view of the system with the pinhole frame and PCB positioned within the 40mm system requirement to the beam port. The microscope has been positioned on the far side, clearing the pinhole frame. The measurement shown is 39.67mm, but the PCB/pinhole group rail still has a small amount of range left to move even closer. The next system requirement is illustrated in Figure 43.

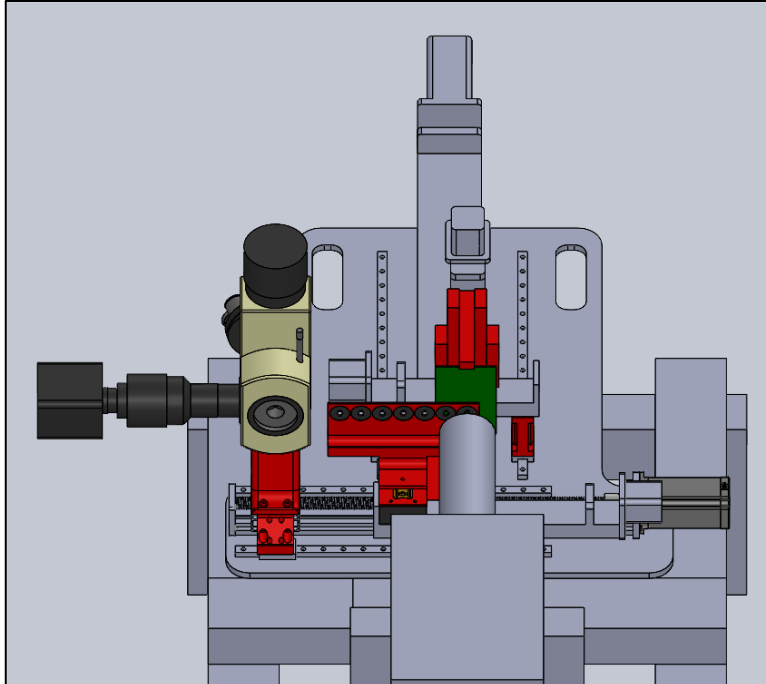

Figure 43. Ability to Test with Smallest Pinhole.

Figure 43 shows the system's ability to test the smallest pinhole, which is located in the furthest right position when viewed from the beam port. The next system requirement is illustrated in Figure 44.

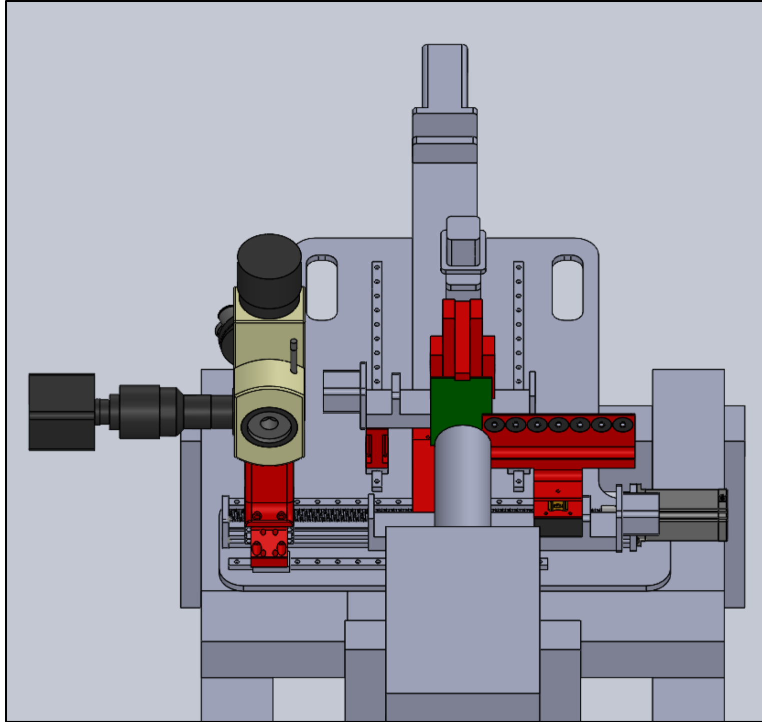

Figure 44. Ability to Test without Beam Reduction.

Figure 44 shows the system's ability to test without beam reduction. The pinhole frame lies outside the center of the beam port by greater than $1/2$", which allows for this test configuration. It also validates the system design requirement to test with all pinholes, as the remaining six pinholes fall between this position and the position shown in Figure 43. After moving the PCB/pinhole group away from the beam port, the microscope may be centered on the beam port. This is the positioning for Figure 45.

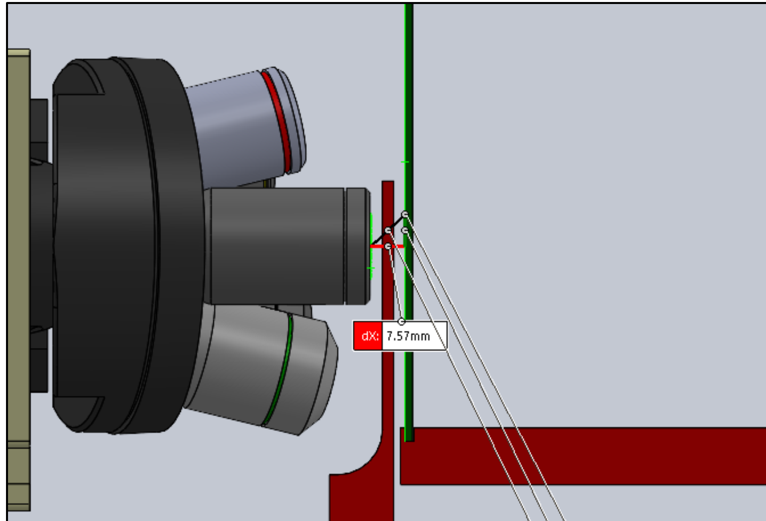

Figure 45. Clearance within Working Distance of Objectives.

Figure 45 shows the ability to position the PCB/pinhole group with the PCB inside the WD of the objective with the highest magnification. With the WD of the 100X objective being 7.6mm, a measured value of 7.57mm satisfies this requirement for the design. Additionally, the objectives can be rotated throughout all five possible positions without colliding with the pinhole frame at the correct imaging distance.

3.3. Electrical Design

The electrical design of this system was driven by the use of stepper motors for motion, the requirements of the BXFM Microscope System, and the system requirement for remote operation. Figure 46 shows an electrical block diagram, describing the major electrical components of the system.

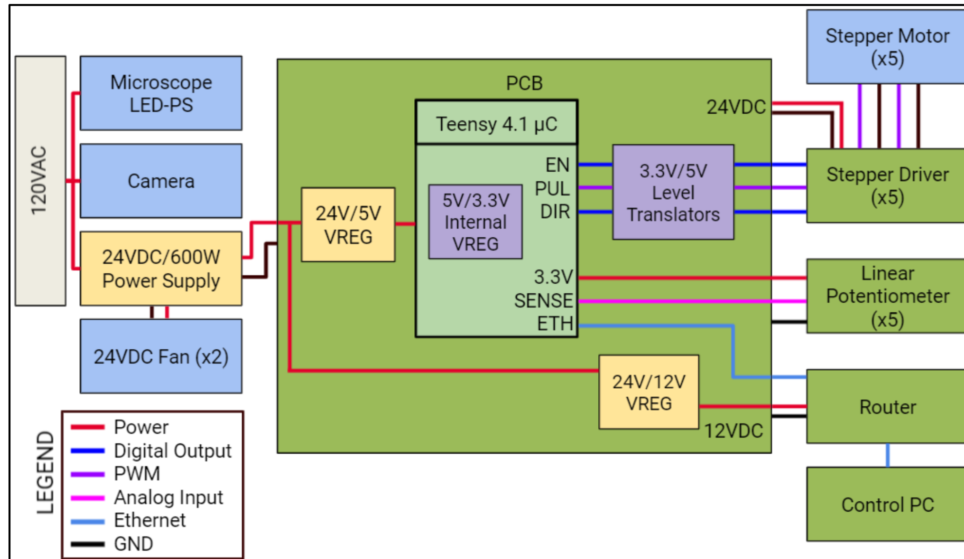

Figure 46. Electrical Block Diagram.

The power source for the system is a standard US wall outlet, providing 15A of current capacity at 120VAC. The AC power supplies the microscope's light-emitting diode (LED) illuminator, the camera, and a 200W power supply that regulates the 120VAC to 24VDC. This 24VDC source supplies a custom PCB and two 24VDC fans, which are used for cooling the electronics enclosure. The PCB includes a 24V/5V voltage regulator (VREG) and a 24V/12V VREG. The 5V powers the Teensy 4.1 microcontroller (µC). This µC has an internal 5V/3.3V VREG and uses 3.3V logic levels. The stepper motor drivers receive 24V through the PCB and require 5V control signals. The control signals are a motor enable (EN) signal, a pulse (PUL) signal, and a direction (DIR) signal. Since the µC has 3.3V logic levels, 3.3V/5V level translators are used to step the control signals up to 5V. With proper control signals, the stepper motor drivers energize the A and B coils of the stepper motors, resulting in rotational motion of the rotors. To compliment the linear motion rails, five linear potentiometers are connected to 3.3V, ground (GND), and analog input pins on the µC for sensing position. The 12V VREG

supplies power for a router, which joins the μC to the control PC over ethernet. Figure 47 shows a picture of the stepper motor driver used.

Figure 47. Stepper Motor Driver [28].

Eight switches set the switching characteristics and current for the stepper motors. The stepper motor drivers for linear motion rails in the system with a 4mm thread pitch are set to 4000 pulses/revolution, while the drivers for linear motion rails with a 5mm thread pitch are set to 5000 pulses/revolution. This effectively allows for 1μm of linear motion per step. The design of the PCB is described in the next section.

3.3.1. PCB Design

The PCB is designed to regulate 24V to 5V and 12V. It also houses the µC and 3.3V/5V level translators. Figure 48 shows the design of the 24V/12V VREG.

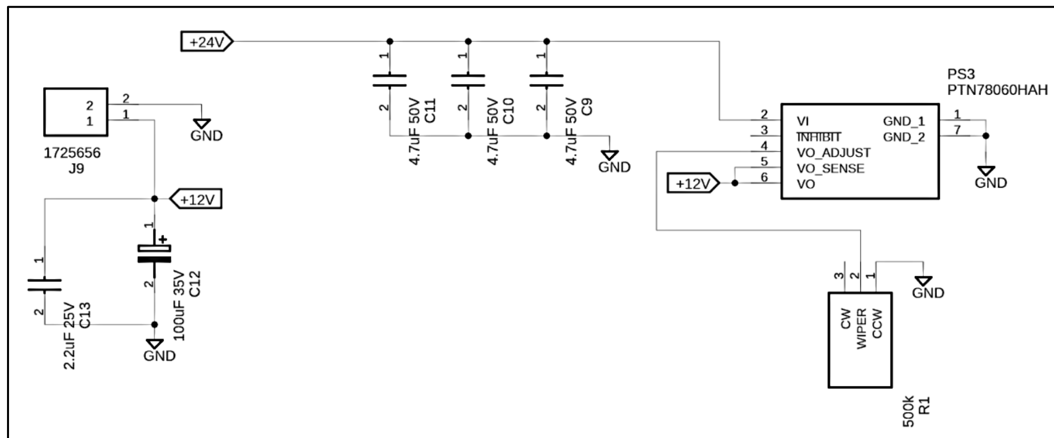

Figure 48. 24V/12V Voltage Regulator Schematic.

The 24V/12V regulation is provided by a TI non-isolated DC/DC converter module. This module requires only limited external components for signal conditioning. The external components include decoupling capacitors for input power, decoupling capacitors for output power, and a potentiometer for setting the regulated voltage level. The rated input voltage range is 15V to 36V, while the rated output range is 11.85V to 22V. With the potentiometer, the output voltage has been set at 12V. The line and load regulation values are sufficient for the application. The DC/DC converter can supply a maximum current of 3A. The safety features include under-voltage lockout, output current limiting, and overtemperature shutdown.

Figure 49 shows the design of the 24V/5V VREG.

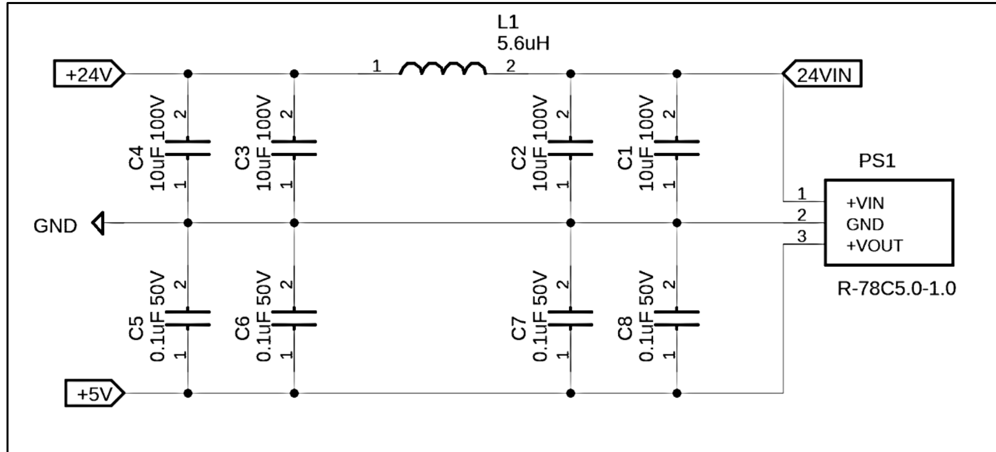

Figure 49. 24V/5V Voltage Regulator Schematic.

The 24V/5V regulation is provided by a RECOM Power non-isolated DC/DC converter module. This module requires an inductor choke and decoupling capacitors on the input and output for signal conditioning. The rated input voltage range is 8V to 42V, while the rated output is 5V. The line and load regulation values are sufficient for the application. The DC/DC converter can supply a maximum current of 1A. The safety features include short-circuit protection and overtemperature protection.

Figure 50 shows the connection scheme for the level translators.

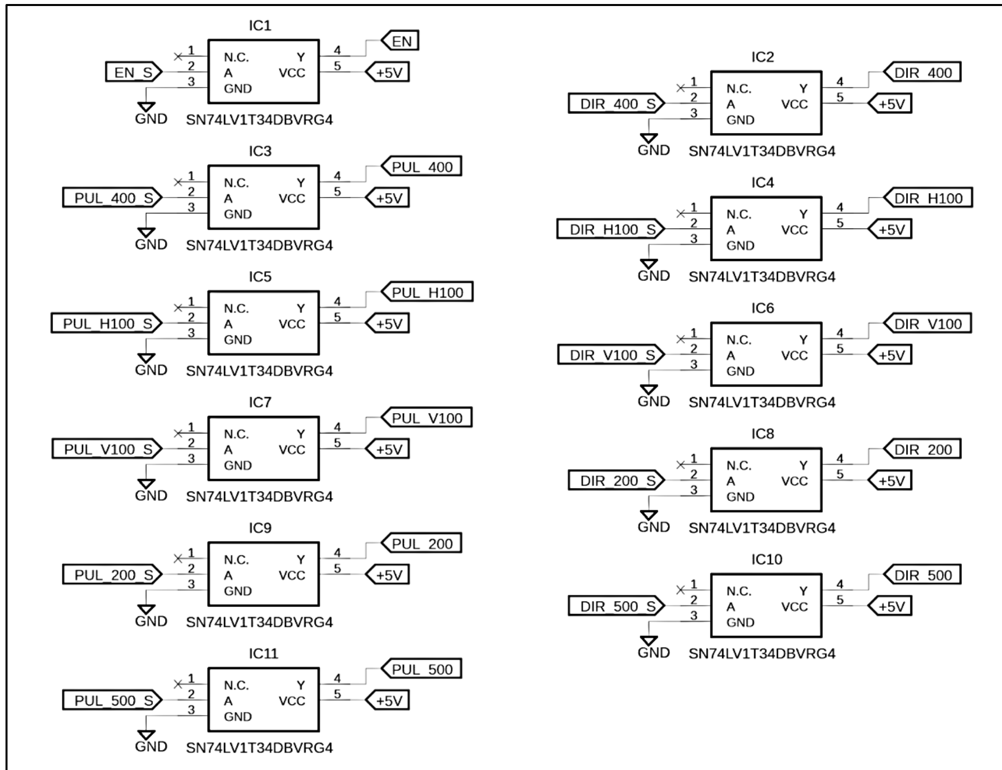

Figure 50. 3.3V/5V Level Translators – Schematic.

A TI single supply, single buffer gate, complementary metal-oxide-semiconductor (CMOS) logic level shifter is used for this application. The level translators require a 3.3V input signal, a GND connection, and a 5V supply to translate 3.3V signals to 5V signals. The level translators have very low propagation delay (3ns) and sufficiently low rise and fall times (20ns/V). Figure 50 shows the level translators shifting the 3.3V signals for the motor enable (EN) signal, all five direction (DIR) signals, and all five pulse (PUL) signals to 5V.

Figure 51 shows the connections made to the µC.

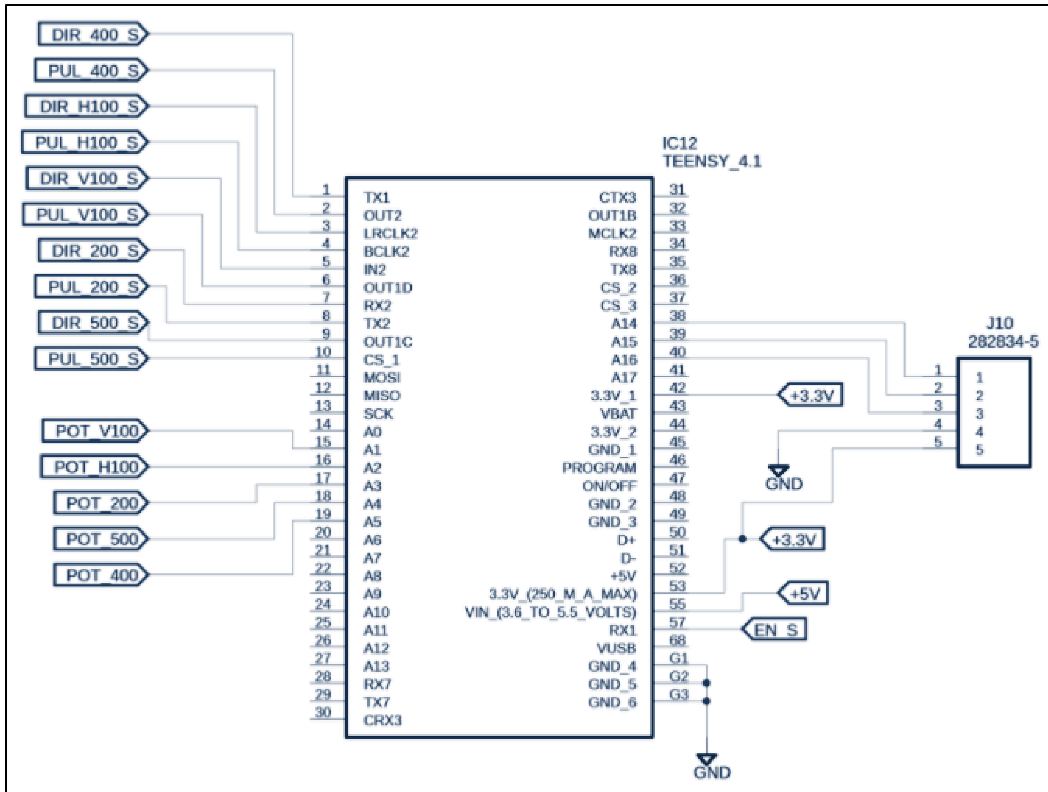

Figure 51. Teensy 4.1 Connections - Schematic.

Figure 51 shows the Teensy 4.1 µC receiving 5V at the VIN pin. Digital output connections to the DIR and PUL labels for each stepper motor driver are found on the left of the schematic. The EN signal is shown coming from pin 57. Also shown are the five analog input connections to each of the linear potentiometers, which also receive a connection to the 3.3V rail from the µC's internal 3.3V regulator. Three extra analog inputs, 3.3V, and GND are also connected to a spare terminal block, J10.

The board layout and design file are created from the overall schematic, resulting in the manufacturing preview in Figure 52.

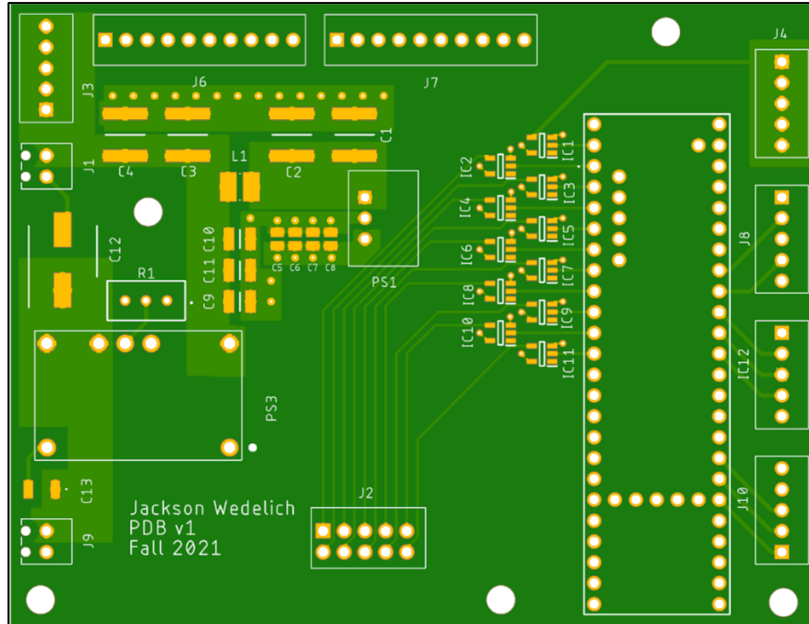

Figure 52. Printed Circuit Board Manufacturing Preview.

Connections in the schematic were routed to create a four-layer PCB design file. Design elements not shown in the schematic figures that are included in the board layout are terminal blocks for external connections. A picture of the µC is shown in Figure 53.

Figure 53. Teensy 4.1 Microcontroller [29].

The footprint of the µC is transferred to the PCB, as shown in Figure 52 on the right half of the PCB. The µC has an ethernet connection through six male pin headers on the top surface

of the µC's board. These pin headers are connected to an RJ45 connector adapter that allows standard RJ45 ethernet cables to interface with the µC. A design-rules check was successfully performed before the design file was sent to a PCB manufacturer for the fabrication process.

3.4. Microcontroller Software

The microcontroller is programmed with a C-based development environment called Teensyduino. The software has been written to read and write custom User Data Protocol (UDP) packets. The structure of these packets is detailed in the next section. Functions in the software use string indexing to interpret packets and translate the information included into the creation of PWM signals for the stepper motors. These PWM signals are created by turning digital outputs on and off at a regular interval of 260µs. This switching delay effectively creates a PWM signal with a period of 460µs and a frequency of 2.1739 kHz. Since the stepper motor drivers are set to result in 1µm of linear travel for each step, the theoretical speed of all rails is 2.1739mm/s.

Lastly, the linear potentiometers are sampled through analog input pins by the µC's analog-to-digital converter (ADC). While this ADC has a nominal resolution of 12 bits, the effective number of bits is closer to 10 bits, giving a digital range of 0 to 1023. Once the value of the 5kΩ and 10kΩ linear potentiometers has been sampled, the values are concatenated into a single string that can be written to a UDP packet. This packet, detailed in the next section, is then sent out to the Control PC over ethernet.

3.5. Communication and Control

Based on the motion system requirements, a communication scheme was developed. The development of this communication scheme was collaborative. A graphical user interface (GUI) was constructed in LabVIEW. This program runs on the Control PC, which has an ethernet connection to the µC. A picture of the GUI is shown in Figure 54.

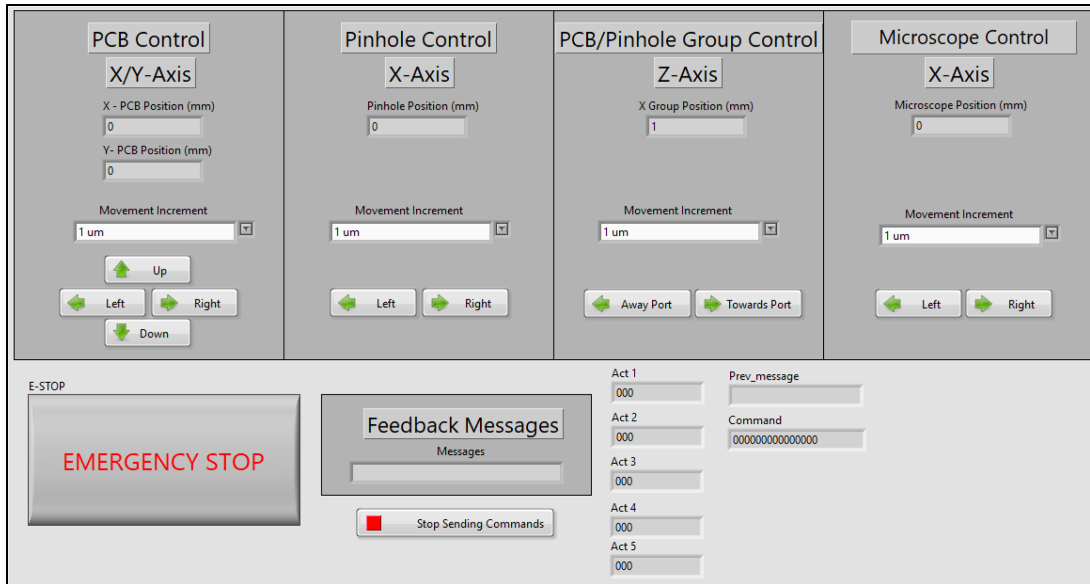

Figure 54. LabVIEW Control GUI.

The LabVIEW control GUI allows an operator to select a movement increment from a dropdown menu for each axis of motion. The operator can then command the incremental motion in either direction along the axis. Clicking the movement buttons on the GUI triggers a command message to be sent from the Control PC to the µC. This message contains the axis, direction, and distance for each button press. The 15-digit command message has a default value of all zeros. Each axis is given three digits that are statically positioned in the message. When a button is pressed, the back end of the GUI changes relevant digits in the command message to reflect the desired motion. The GUI also has an emergency stop button. This button changes all of the command digits to nines. The µC interprets this as an emergency stop, locking out the possibility of pulses being delivered to the stepper motor drivers when triggered.

The GUI also reads UDP packets sent from the μC containing the feedback values of the linear potentiometers. These are translated into distance measurements and displayed. A table showing the increments of motion available for each axis is shown below.

PCB X-axis	PCB Y-axis	Pinhole X-axis	PCB/Pinhole Group Z-axis	Microscope X-axis
1μm	1μm	1μm	1μm	1μm
10μm	10μm	10μm	10μm	10μm
20μm	20μm	20μm	100μm	20μm
50μm	50μm	50μm	500μm	50μm
100μm	100μm	100μm	1mm	100μm
500μm	500μm	500μm	5mm	500μm
1mm	1mm	1mm	20mm	1mm
5mm	5mm	5mm	50mm	5mm
10mm	10mm	10mm	220mm	239mm

Table 1. Increments of Motion for Each Axis.

Increments of motion were selected collaboratively, as overlap was present in the impact of the increment size. The increments are selected to give an operator a usable range for each axis, based on its full range and purpose. Notable deviations from nominal values can be seen in the largest increments for the PCB/pinhole group axis and the microscope axis. The largest increment for the PCB/pinhole group is 220mm because this is the distance that needs to be covered when moving the axis from the focal plane of the microscope to the 40mm air gap required to the beam port. The largest increment for the microscope axis is 239mm because this is the distance required to move the microscope away from the center of the beam port for radiated tests. The next section overs the camera software.

3.6. Camera Software

Olympus provides a free software that integrates with the camera called EPView. This software includes a variety of features that are critical to this research. The software allows for live streaming, snapshots, and movie recording. When setting up the software and microscope for the first time, a calibration process can be completed. This calibration process calibrates the relationship between the camera's sensor and each objective. To perform this calibration, a rule is placed in the FOV. Known distances from the rule are translated to the software via its measurement feature. Once the calibration is complete, all measurements taken from images in the software have the accuracy of the rule used for calibration.

The options for measurement include the position of a point, the distance between two points, the dimensions of a rectangle or circle, and the dimensions of a freehand polygon. These functions are used in section 5.

3.7. Concept of Operations

To use the system, an operator must first install the system onto the platter of the in-air test station. Once bolted down, the microscope starts from the left side of the adapter plate when viewed from the beam port. After installation of the PCB, test setup connections may be made. All connections to the electrical enclosure can then be made. The system is then turned on with a rotary switch on the electrical enclosure. The Control PC is connected to the ethernet cable coming from the electrical enclosure.

After verifying communication with the system and the camera through the control GUI and EPView camera software, the operator will center the microscope on the beam port. The PCB/pinhole group axis can then be controlled to bring the PCB into view of the microscope. After the PCB can be imaged, the operator will use the control GUI to position the PCB

horizontally and vertically, identifying and centering the region of interest. Upon successful positioning of the PCB, the desired pinhole can be brought into place with the control GUI. The PCB/pinhole group is then moved away from the beam port until the pinhole is in focus. The operator may then apply small movements to the pinhole axis until the pinhole is centered in the view. Once the pinhole has been centered over the region of interest on the PCB, the microscope can be moved 239mm to the left, clearing the footprint of the pinhole frame and the beam port. Finally, the PCB/pinhole group are moved toward the beam port 220mm. At this point, an irradiated test can be started. Once a test has been finished, the operator can reverse the previous steps to identify a new region of interest. Additional figures illustrating this process can be found in Appendix A of this document.

4. IMPLEMENTATION

The implementation of this system was accomplished in phases related to different portions of the system. This section describes the process at key points of integration.

4.1. Mechanical and Microscope Components

The adapter plate was manufactured by the Fischer Engineering Design Center (FEDC) at the Zachry Engineering Complex. The FEDC accepted a design file and used a high-pressure water jet to cut the outline of the adapter plate. The holes in the adapter plate were drilled and tapped with a computer numerical control (CNC) machine.

Figure 55. Manufactured Adapter Plate.

Once the adapter plate was manufactured, 3D printed components were manufactured as designed. 3D printed brackets were first printed at a low percentage of infill for fitment testing. Once fitment was validated, components were printed again at 100% infill with a thermoplastic

called polylactic acid (PLA). The 3D printers used were an Ender 3 Pro and a Prusa i3 MK3. After the 3D printing process was complete, the linear motion and slide rails, microscope, and brackets could be integrated with the adapter plate. Figure 56 shows this stage of the implementation process.

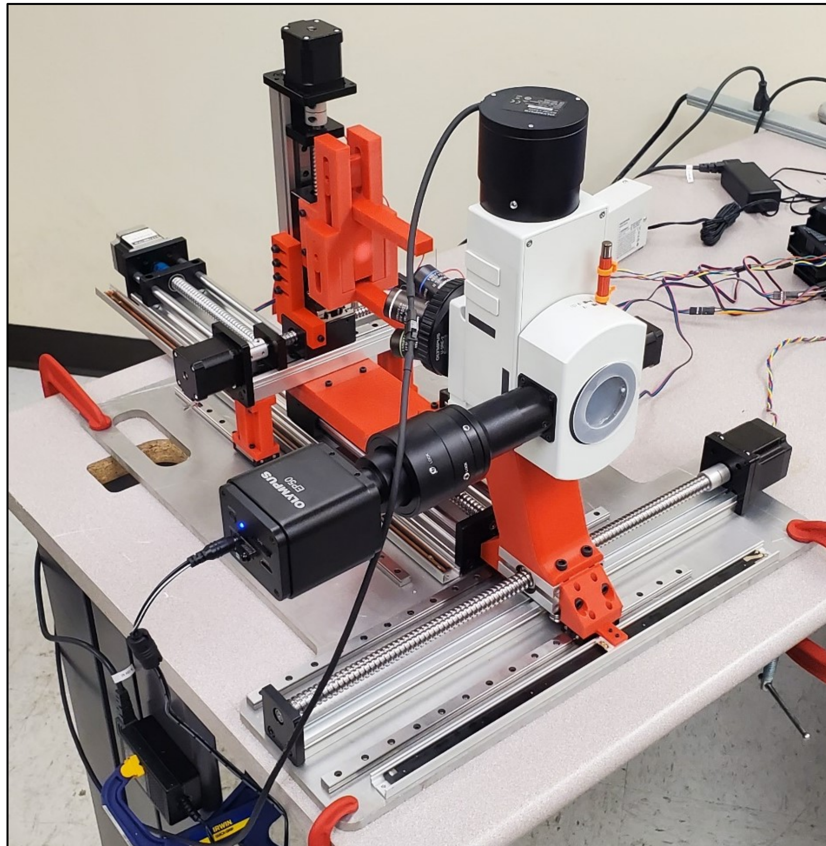

Figure 56. Mechanical Component and Microscope Integration.

The microscope was assembled and calibrated with guidance from a field service engineer from Olympus. After this stage of implementation, the electrical components of the system were assembled into an electronics enclosure.

4.2. Electrical Implementation

The PCB design file, shown in Figure 52, was sent to JLCPCB for manufacturing. The resulting PCB blank is shown in Figure 57.

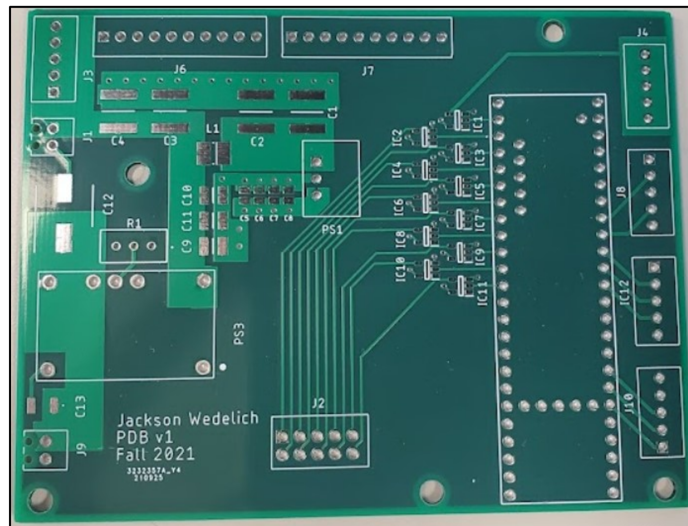

Figure 57. Printed Circuit Board from JLCPCB.

The PCB blank was then populated with components, as shown in Figure 58. All components shown in the schematics and terminal blacks were soldered to the PCB.

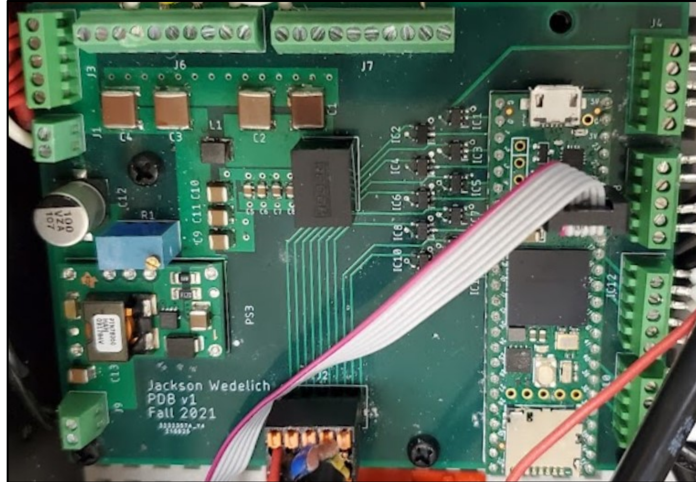

Figure 58. Populated Printed Circuit Board.

After the PCB was populated, an electronics enclosure was designed and constructed with off-the-shelf components. The construction of the electronics enclosure was a collaborative effort with Dylan Blezinger. This electronics enclosure uses Ferrule connectors for wire termination, aviation bulkhead connectors for connections to the stepper motors and linear potentiometers, and panel-mount switches for the on/off and emergency stop switches. Additionally, a standard US outlet was added to give the microscope's camera and illuminator power. Holes were drilled into the sides of the electronics enclosure for all circular bulkhead connectors and profiles were cut for rectangular bulkhead connectors. Holes were also made for the 24V fans. An open-top view of the electronics enclosure is shown in Figure 59, while Figure 60 shows a closed side view of the electronics enclosure.

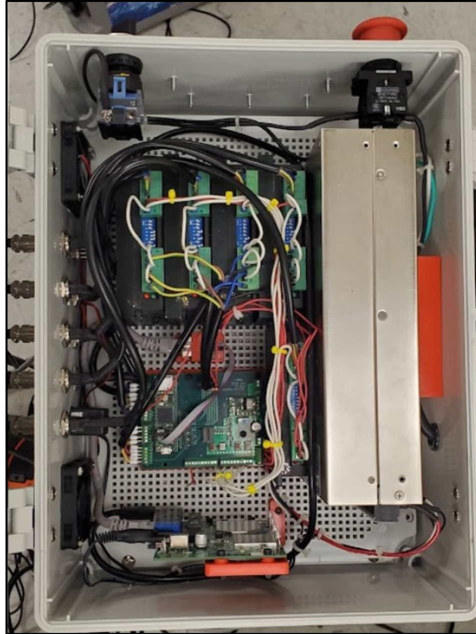

Figure 59. Electronics Enclosure – Open-Top View.

Figure 60. Electronics Enclosure – Closed Side View.

The next section shows the final integration of the system with the pinhole frame and pinholes. The pinhole frame and pinholes are the work of Dylan Blezinger.

4.3. Final Integration

The result of the final integration of the complete system is shown in Figure 61. Additional images of the full system can be found in Appendix A of this document.

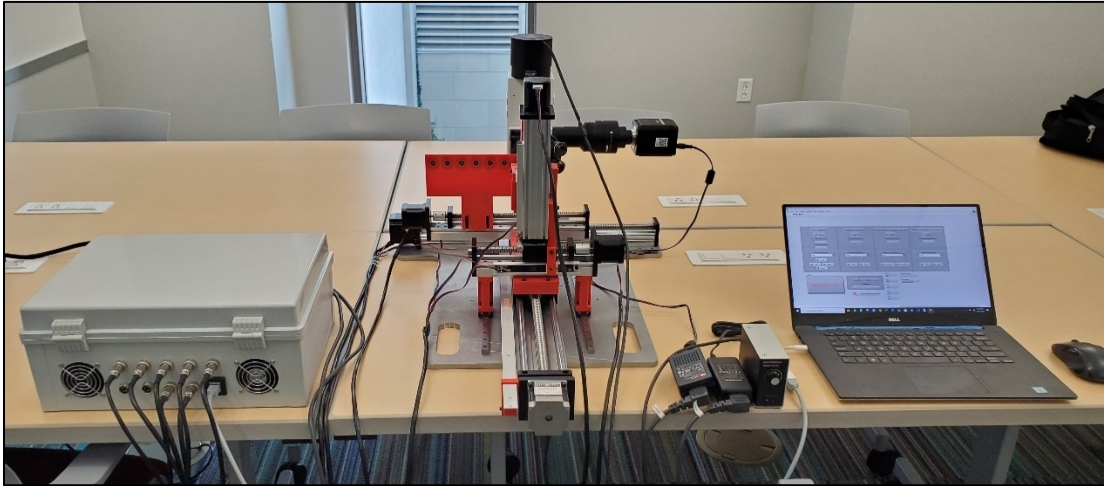

Figure 61. Full System Integration.

5. MEASUREMENTS AND RESULTS

The measurements and results are split into sections including motion, electrical, and optics. An emphasis of meeting system requirements is present throughout.

5.1. Motion Measurements

To characterize the motion capability of the system, measurements were taken according to system requirements. The system requirements for motion are a mounted system weight less than 100lbs, incremental motion of less than 5µm for the positioning of the PCB and pinhole axes, incremental motion of less than 500µm for the positioning of the microscope, and incremental motion less than the DOF of the objective with the highest magnification (1.3µm) for the focusing axis.

Several measurement tools were made available for this research, but only two available tools had the accuracy required to measure on the micron scale. The first measurement tool considered was an outside micrometer made by Starrett. An example of the measurement tool is shown in Figure 62.

Figure 62. Electronic Outside Micrometer – Starrett [30].

While the measurement tool has the ability to take measurements on the scale required, the practical use of the tool for repetitive measurements is less than ideal. The tool would

introduce human error through repetitive replacement of the tool between movements. Additionally, the accuracy of measurements taken would be limited by the flatness of surfaces in the system. These surfaces do not have a system requirement of flatness on the micron scale. Finally, the system requirements for motion are defined at the PCB or pinhole and not the stage of an axis. Measuring at the PCB or pinhole with this tool would require the construction of a highly-precise and stable reference used solely for measurement. The use of an inside micrometer carries this same disadvantage.

The second measurement tool considered was the microscope used in the system. Once the microscope is calibrated with a stage micrometer, the measurement functionality of the EPView software is accurate to the tolerance of the stage micrometer. After calibration, the stage micrometer can be placed in the PCB mount or attached to the pinhole rail to characterize the motion at the point of the PCB or pinhole frame. This is the measurement tool that was selected for this research.

The stage micrometer used was an Olympus stage micrometer including three calibration standards. The first standard, the P50, has a tick-to-tick distance of 50µm ± 3% (± 1.5µm). The second standard, the P10, has a tick-to-tick distance of 10µm ± 3% (± 0.3µm). The third standard, the P3, has a tick-to-tick distance of 3µm ± 3% (± 0.09µm). The distances are defined at the leading edges of each tick. The smallest viable calibration standard was used to calibrate each objective.

After the static calibration process, the movement testing could be done using EPView to take measurements. The first three rails characterized were the 100mm horizontal PCB rail, the 100mm vertical PCB rail, and the 200mm horizontal pinhole rail. Incremental motion was tested at all preset increments ≤ 100µm.

5.1.1. Data Collection Procedure - Motion

For each tested increment of motion on each axis, the calibration slide was mounted to the system and brought into focus. After the appropriate calibration standard was centered, a tick near the center of the standard was selected and centered within the FOV. A point was placed with the EPView measurement tool over the lower corner of the selected tick on the side of the leading edge. With this first point serving as the origin, five movements were made in the first direction to clear any backlash in the linear motion rail. A point is placed on the lower corner of the leading edge of the centered tick after each movement. A direction change is then made by moving in the opposite direction ten times. A point is also placed after each of these movements. Finally, a direction change to the original direction is made by moving in the original direction ten times.

This procedure produces a set of 26 numbered points with the accuracy of the calibration standard for data analysis. The procedure accounts for any loaded backlash in the linear motion rail through the first five points. These first five points are discarded, as removal of the backlash at the beginning of the test is an administrative procedure. The resulting 21 points include nine repetitive movement points for each direction and a characterization of the backlash in each direction change. Nine points for each direction was determined to be the longest stretch of motion available across all calibration standards without overrunning the standard. Five movements in the beginning were determined to be sufficient for removing backlash through practical use of the system.

5.1.2. Motion Results and Analysis

The first rail to be characterized was the 100mm horizontal PCB rail. The error distribution graphs for each rail can be found in Appendix B of this document. The figures in this

section represent the average error of the nine repeated moves in each direction at each tested increment. Tables in this section show the statistics that describe the worst-case scenario and repeatability of each movement.

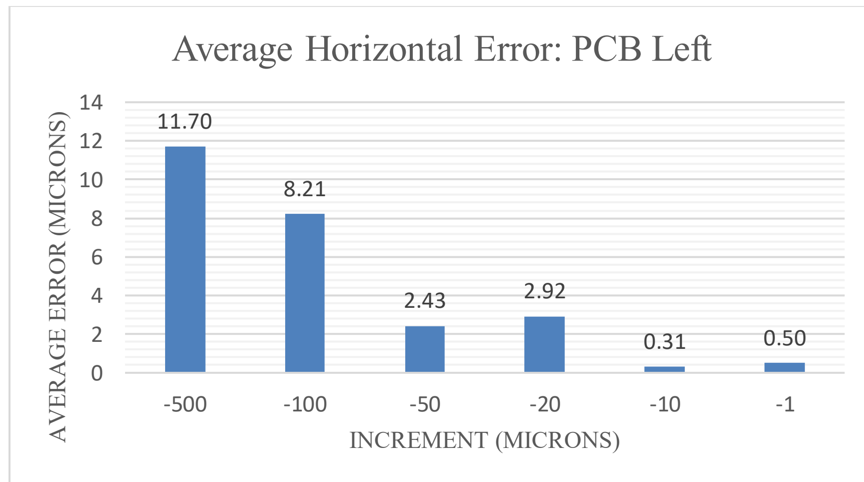

Figure 63. Average Horizontal Error: PCB Left.

Figure 63 shows the average error of the 100mm horizontal PCB rail at increments of motion from 500µm left to 1µm left. The magnitude of the error decreases as the increment decreases, with the exception of the 20µm and 1µm increments.

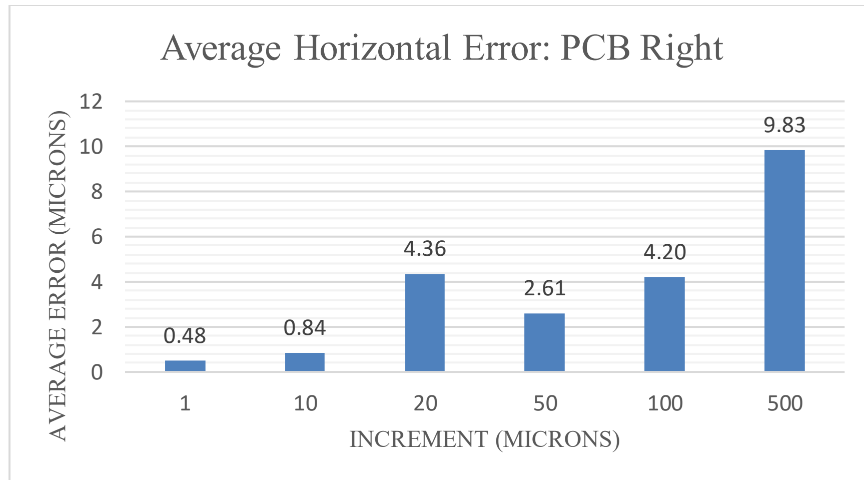

Figure 64. Average Horizontal Error: PCB Right.

Figure 64 shows the result of the same procedure moving right. A similar trend is shown, with decreasing error as increment decreases, with the exception of the 20μm increment. Table 2 shows the maximum error and standard deviation of all measured movements for the horizontal PCB rail.

Increment (μm)	Direction	Max_{Error}(μm)	σ (μm)
500	Left	18.45	6.48
100	Left	16.25	5.50
50	Left	5.40	1.83
20	Left	8.74	2.83
10	Left	1.11	0.32
1	Left	0.78	0.27
500	Right	19.23	6.58
100	Right	7.62	2.53
50	Right	9.45	3.39
20	Right	7.97	2.82
10	Right	3.26	0.94
1	Right	0.84	0.25

Table 2. Horizontal PCB Rail Movement Statistics.

The resulting movement statistics do not appear to show a clear bias to either direction. Additionally, the recorded maximum error in incremental motion for the smallest increment shows that, even with variation, the 100mm horizontal PCB rail meets the system requirement of incremental motion less than 5µm. The next rail to be characterized is the 100mm vertical PCB rail.

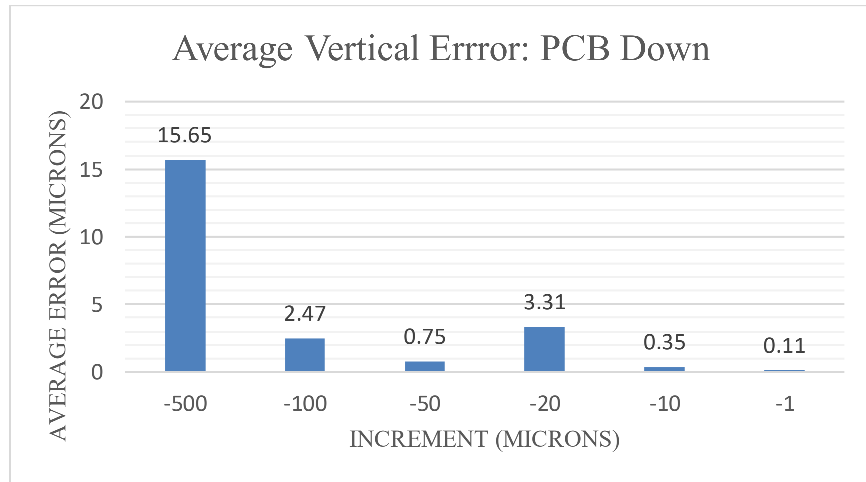

Figure 65. Average Vertical Error: PCB Down.

Figure 65 shows the result of the same procedure moving down. A similar trend is shown, with decreasing error as increment decreases, with the exception of the 20µm increment.

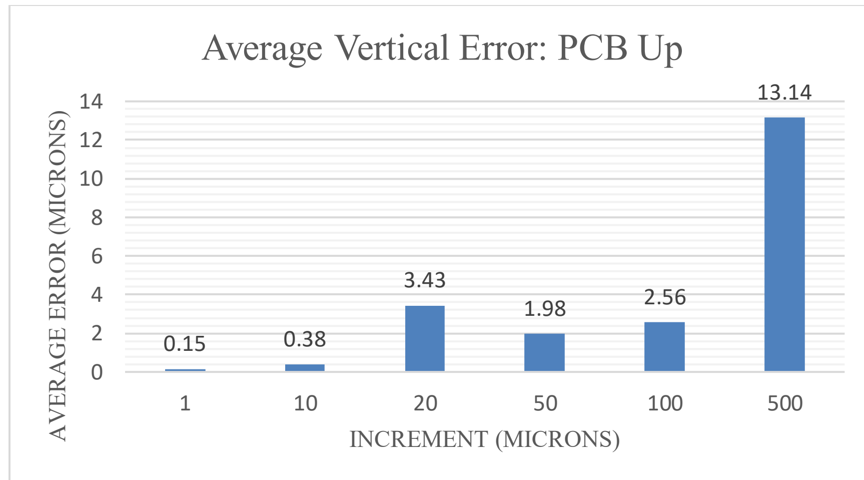

Figure 66. Average Vertical Error: PCB Up.

Figure 66 shows the result of the same procedure moving up. A similar trend is shown, with decreasing error as increment decreases, with the exception of the 20µm increment. Table 3 shows the maximum error and standard deviation of all measured movements for the vertical PCB rail.

Increment (µm)	Direction	Max_{Error}(µm)	σ (µm)
500	Up	48.88	16.35
100	Up	9.32	2.75
50	Up	1.68	0.58
20	Up	5.98	1.97
10	Up	0.61	0.17
1	Up	0.26	0.09
500	Down	28.20	10.05
100	Down	4.74	1.66
50	Down	4.23	1.37
20	Down	7.36	2.21
10	Down	0.69	0.18
1	Down	0.31	0.09

Table 3. Vertical PCB Rail Movement Statistics.

The resulting movement statistics do not appear to show a clear bias to either direction. Additionally, the recorded maximum error in incremental motion for the smallest increment shows that, even with variation, the 100mm vertical PCB rail meets the system requirement of incremental motion less than 5µm. The next rail to be characterized is the 200mm horizontal pinhole rail.

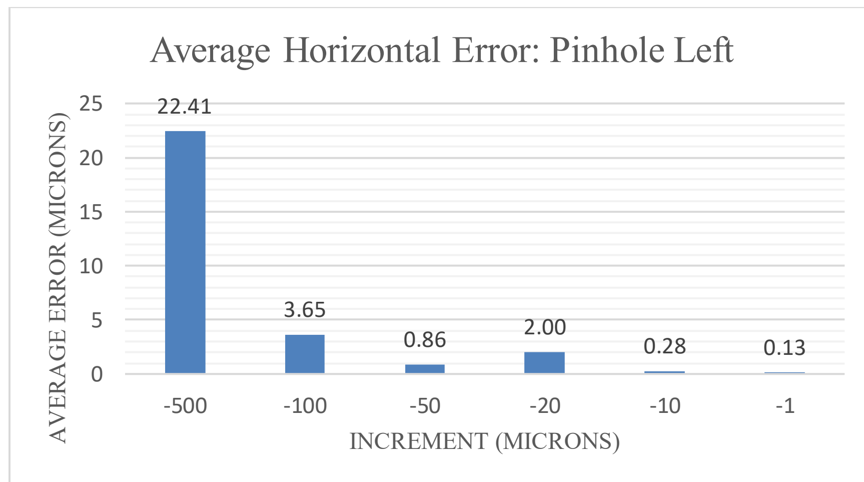

Figure 67. Average Horizontal Error: Pinhole Left.

Figure 67 shows the result of the same procedure moving the pinhole to the left. A similar trend is shown, with decreasing error as increment decreases, with the exception of the 20µm increment.

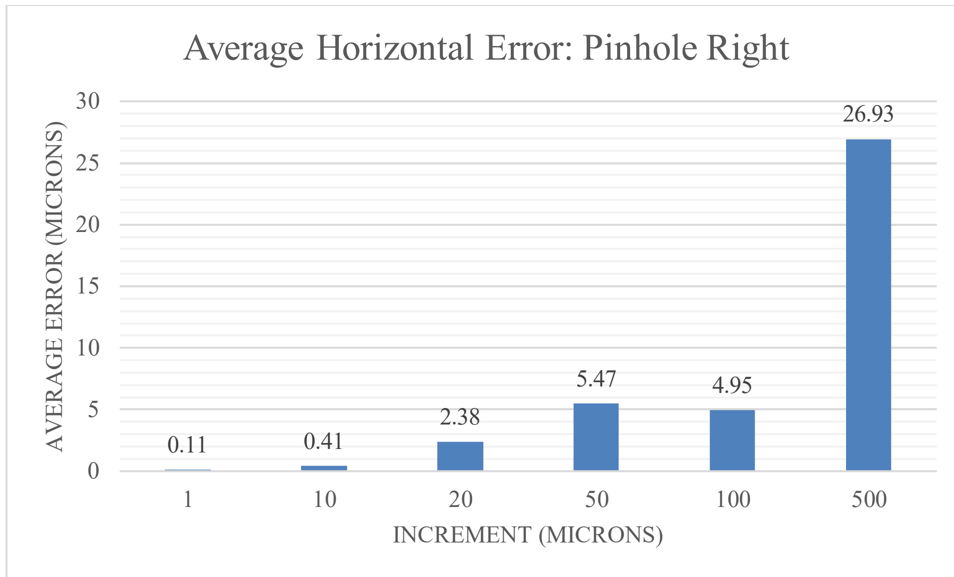

Figure 68. Average Horizontal Error: Pinhole Right.

Figure 68 shows the result of the same procedure moving the pinhole to the right. A similar trend is shown, with decreasing error as increment decreases, with the exception of the 50µm increment.

Table 4 shows the maximum error and standard deviation of all measured movements for the pinhole rail.

Increment (µm)	Direction	Max_{Error}(µm)	σ (µm)
500	Left	65.56	22.47
100	Left	8.47	2.79
50	Left	2.28	0.81
20	Left	2.89	0.82
10	Left	0.58	0.18
1	Left	0.26	0.08
500	Right	109.62	32.01
100	Right	14.52	5.27
50	Right	9.45	3.08
20	Right	5.41	1.71
10	Right	0.78	0.32
1	Right	0.22	0.07

Table 4. Pinhole Movement Statistics.

The resulting movement statistics do not appear to show a clear bias to either direction. Additionally, the recorded maximum error in incremental motion for the smallest increment shows that, even with variation, the 200mm horizontal pinhole rail meets the system requirement of incremental motion less than 5µm.

The system requirement for incremental motion less than the DOF of the objective with highest magnification was met. Proof of meeting this requirement is found in section 5.3 through the successful use of the 100X objective to image the IC.

The system requirement for incremental motion less than 500µm for the 400mm microscope rail was also met. Proof of meeting this requirement is obtained through the successful positioning of the microscope for all tests performed with pinholes in section 5.3.1.3.

The results of repetitive incremental motion show that the positioning system successfully meets system requirements for incremental motion. Though it was not a system requirement that required proof, mechanical backlash of the rails was observed throughout the data collection process. Without a rotary encoder or angular measurement device with sufficient

precision that is compatible with the linear motion rails, angular backlash of the rails could not be specifically characterized. However, the backlash as measured by linear travel was practically determined to be roughly 2µm to 3µm across all rails. This means that when using the smallest increment of motion (1µm), a direction change requires two to three steps before motion in the second direction is realized. Backlash of this level is most probably caused by a non-zero clearance between the ball-bearings and nut tracks in the ball-screw housing. This could be minimized with a pre-loaded ball-screw, but this level of backlash does not keep the system from meeting requirements of incremental motion.

5.2. Electrical Measurements

Electrical measurements, though not directly included in system requirements, were derived requirements. The electrical system was validated for safety and proof of design. A digital multimeter (DMM) was used to verify the AC and DC voltage levels at the outputs of the PCB VREGs, the µC low-voltage supply, and the input and output of the 24V power supply. Additionally, an oscilloscope was used to characterize the PWM signals at the µC and after the level translators.

5.2.1. Electrical Results and Analysis

Table 5 shows the electrical results from measurements taken with the DMM.

Measurement	Nominal Value	Result	% Error
Power Input	120VAC	121.2VAC	--
Power Supply Output	24VDC	23.98VDC	0.083%
12V VREG	12VDC	12.01VDC	0.083%
5V VREG	5VDC	5.01VDC	0.2%
µC Logic Level Supply	3.3VDC	3.281VDC	0.576%

Table 5. Electrical Results - Digital Multimeter.

The electrical results from measurements taken with the DMM delivered expected values for effective and safe operation. Figure 69 shows the 3.3V PWM signal as captured by the oscilloscope.

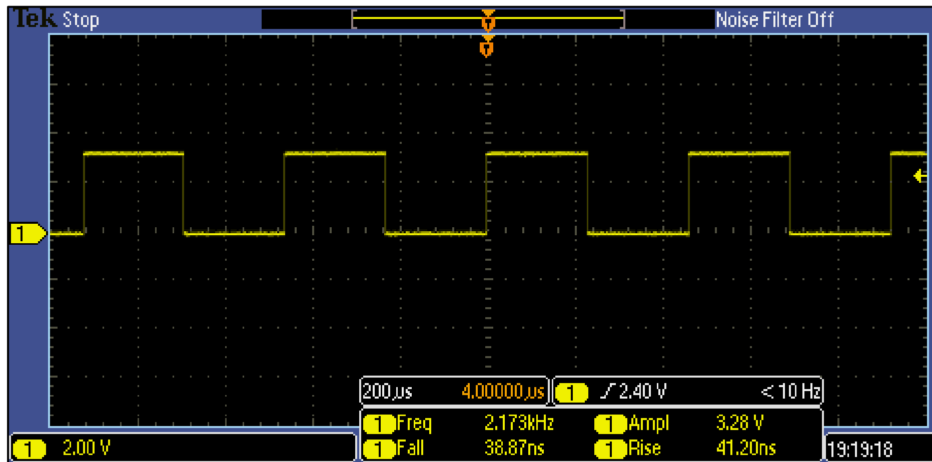

Figure 69. 3.3V PWM Signal – Oscilloscope.

Figure 70 shows the 5V PWM signal as captured by the oscilloscope.

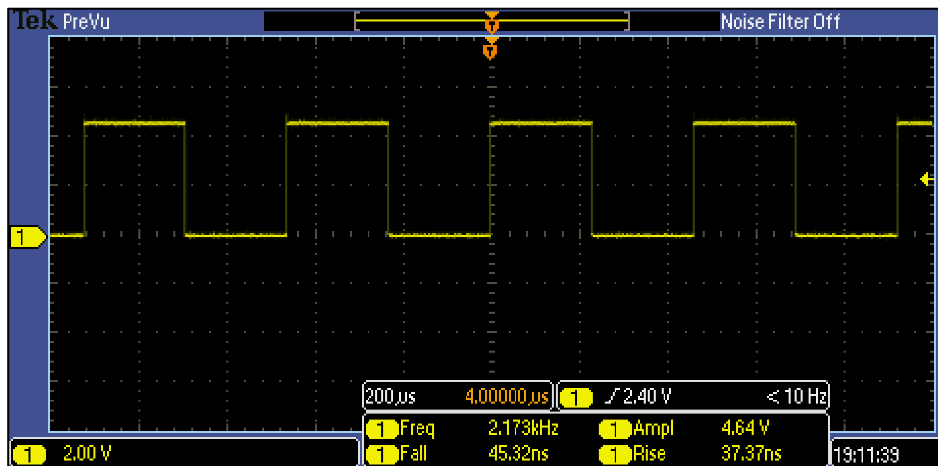

Figure 70. 5V PWM Signal – Oscilloscope.

Table 6 shows the rise time (RT) and fall time (FT) results of the 3.3V and 5V PWM signals.

Source	RT_{MEAS}	RT_{EXP}	ΔRT	FT_{MEAS}	FT_{EXP}	ΔFT
3.3V	41.2 ns	--	--	38.87 ns	--	--
5V	37.37 ns	92.8 ns	-55.43 ns	45.32 ns	92.8 ns	-47.78 ns

Table 6. PWM Rise and Fall Time Results.

The RT and FT of the µC's digital output pins are not stated in the datasheet, but the RT and FT of the level translators is stated to be a maximum of 20 ns per volt. The measured RT and FT of the 5V signal are lower than the maximum value. This validates proper switching of the level translators.

Source	Amp_{MEAS}	Amp_{EXP}	% $Error_{Amp}$	f_{MEAS}	f_{EXP}
3.3V	3.28V	3.3V	0.61%	2.173 kHz	2.1739 kHz
5V	4.64V	5V	7.2%	2.173 kHz	2.1739 kHz

Table 7. PWM Amplitude and Frequency Results.

The amplitude and frequency results for the 3.3V and 5V PWM signals are acceptable. The difference between the measured and expected frequencies can be attributed to the truncation of the measurement by the oscilloscope. The percent error in the 5V amplitude is

higher than expected, but the stepper motor drivers and stepper motors function properly, indicating that this value is acceptable.

5.3. Optical Measurements

Optical measurements are divided into three sections. The first section includes measurements taken on calibration standard. The second section includes measurements taken on an IC. The third section includes the results of investigating the research question described in section 1.1. Optical measurements were taken through the EPView software after the calibration procedure described in section 5.1 had been conducted.

The system requirements for the microscope include the ability to fit predefined pinhole sizes within the fields of view and the ability to resolve features smaller than 1µm. In addition to measurements taken against a calibration standard, TI required the practical use case of the microscope to be proven. To meet this requirement, TI provided a PCB with a de-capped IC for use during this research. Figure 71 shows an image of the PCB.

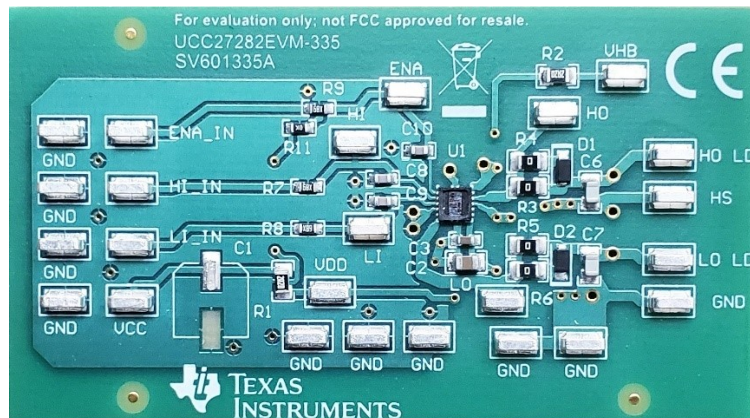

Figure 71. UCC27282EVM-335 PCB from Texas Instruments.

The UCC27282EVM-335 PCB hosts a UCC27282DRC IC, which is a 120V half bridge gate driver. This PCB is representative of a typical PCB that the TI Space Power team would normally test for SEEs.

5.3.1. Optical Results and Analysis

As previously described, the optical results are divided into three sections. The first covers FOV measurements and pinhole fitment tests measured from a calibration standard.

5.3.1.1. FOV Results and Analysis

Each objective was first focused onto an appropriately sized calibration standard. Using the EPView software, a rectangular measurement filling the entire FOV is taken in the live streaming mode. After this measurement is taken, a snapshot is taken. A secondary rectangular measurement fills the new FOV given by the snapshot. Finally, circles are drawn to show the pinholes that fit best in the live streamed FOV. Figure 72 shows the result of following this procedure with the 5X objective.

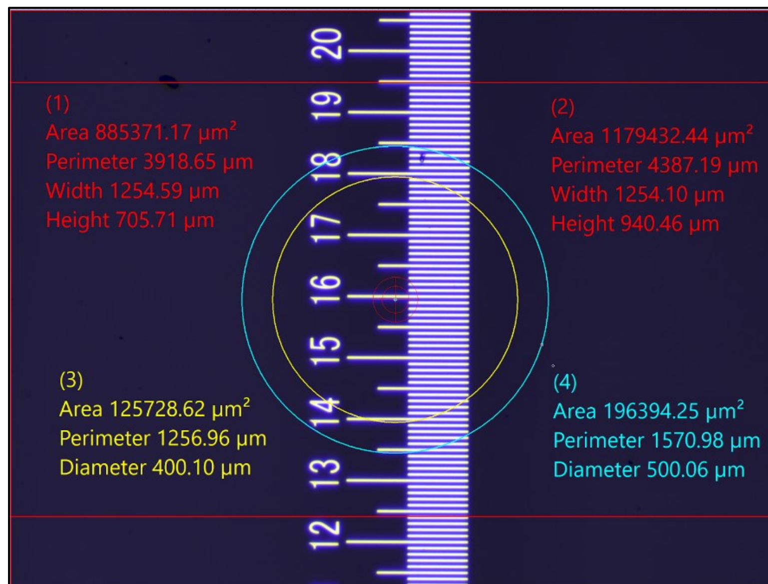

Figure 72. 5X Objective FOV on P10 Standard.

The result in Figure 72 shows the measured live stream and snapshot fields of view of the 5X objective on the P10 standard. Also shown are representations of a 400µm and a 500µm pinhole. Figure 73 shows the results of the same procedure with the 10X objective.

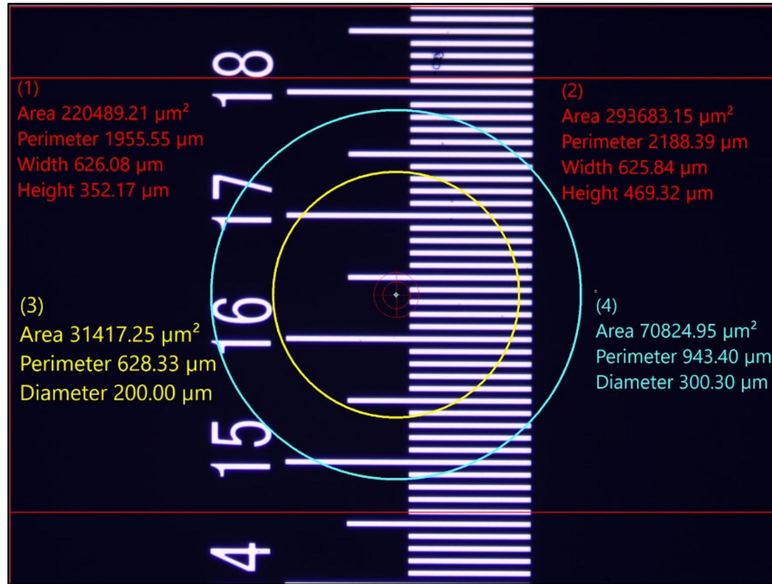

Figure 73. 10X Objective FOV on P10 Standard.

The result in Figure 73 shows the measured live stream and snapshot fields of view of the 10X objective on the P10 standard. Also shown are representations of a 200µm and a 300µm pinhole. Figure 74 shows the results of the same procedure with the 20X objective.

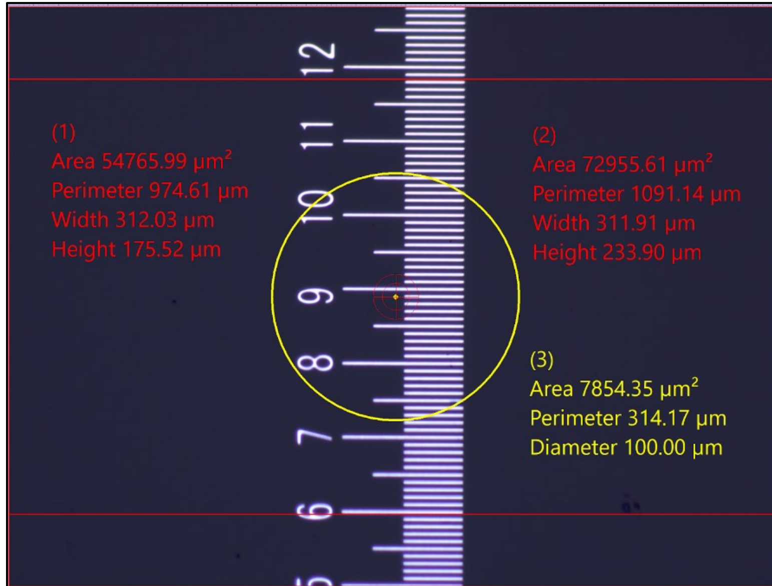

Figure 74. 20X Objective FOV on P3 Standard.

The result in Figure 74 shows the measured live stream and snapshot fields of view of the 20X objective on the P3 standard. Also shown is a representation of a 100µm pinhole. Figure 75 shows the results of the same procedure with the 50X objective.

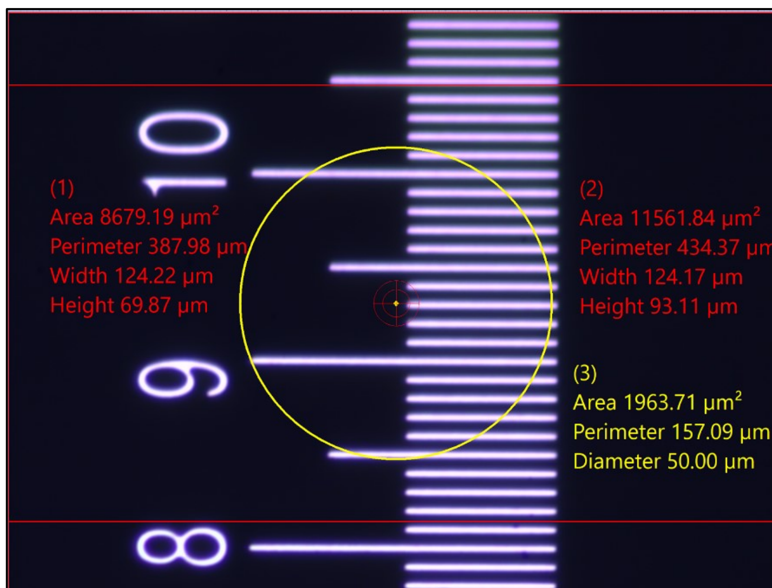

Figure 75. 50X Objective FOV on P3 Standard.

The result in Figure 75 shows the measured live stream and snapshot fields of view of the 50X objective on the P3 standard. Also shown is a representation of a 50μm pinhole. Figure 76 shows the results of the same procedure with the 100X objective.

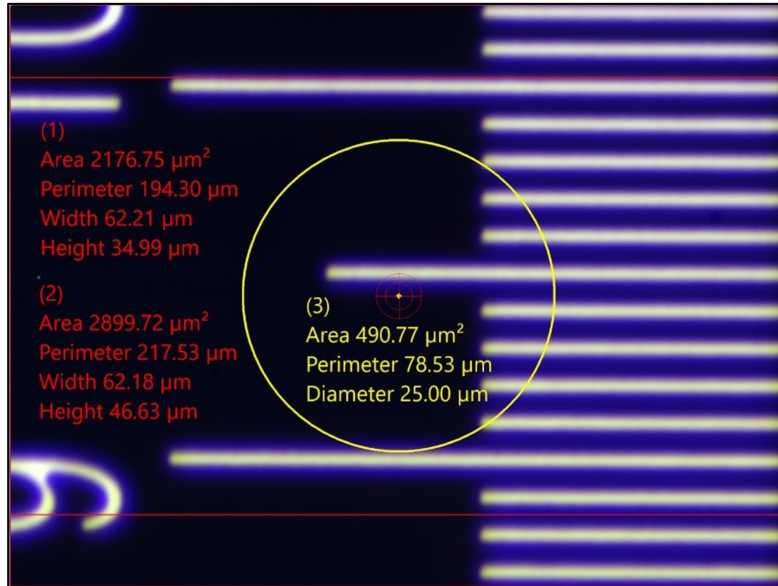

Figure 76. 100X FOV on P3 Standard.

The result in Figure 76 shows the measured live stream and snapshot fields of view of the 100X objective on the P10 standard. Also shown is a representation of a 25μm pinhole.

Table 8 shows the resulting FOVs as compared to the theoretical FOVs calculated in section 3.1.2.

Objective	Theoretical FOV_W (µm)	Measured FOV_W	%Error FOV_W	Theoretical FOV_H	Measured FOV_H	%Error FOV_H
5X	1244.16µm	1254.10µm	0.799%	933.12µm	940.46µm	0.787%
10X	622.08µm	625.84µm	0.604%	466.56µm	469.32µm	0.592%
20X	311.04µm	311.91µm	0.280%	233.28µm	233.90µm	0.266%
50X	124.42µm	124.17µm	0.201%	93.31µm	93.11µm	0.214%
100X	62.21µm	62.18µm	0.048%	46.66µm	46.63µm	0.064%

Table 8. Calculated FOV versus Measured FOV.

The resulting measured FOVs were sufficiently close to the calculated values. Differences in FOV and magnification are accounted for by the calibration process.

5.3.1.2. Practical Use Results and Analysis

The IC circuit provided by TI was imaged using all objectives. Various measurement capabilities of the EPView software are used in the images to show IC feature sizes. Figure 77 shows a view of the IC when imaged with the 5X objective.

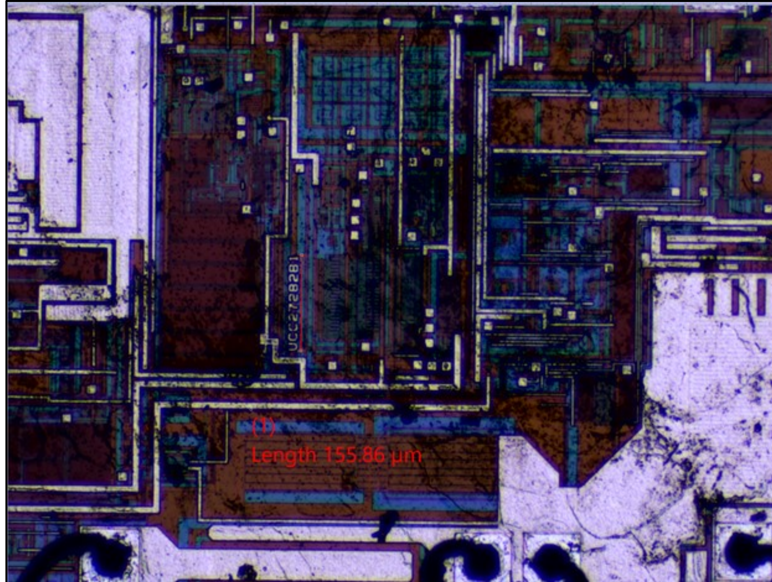

Figure 77. UCC27282DRC Imaged with 5X Objective.

The resulting image in Figure 77 shows the largest FOV on the UCC IC. A measurement of the IC’s label is included in the image. When coupled with the motion system, single-FOV images can be stitched together to create larger images as shown in Figure 78.

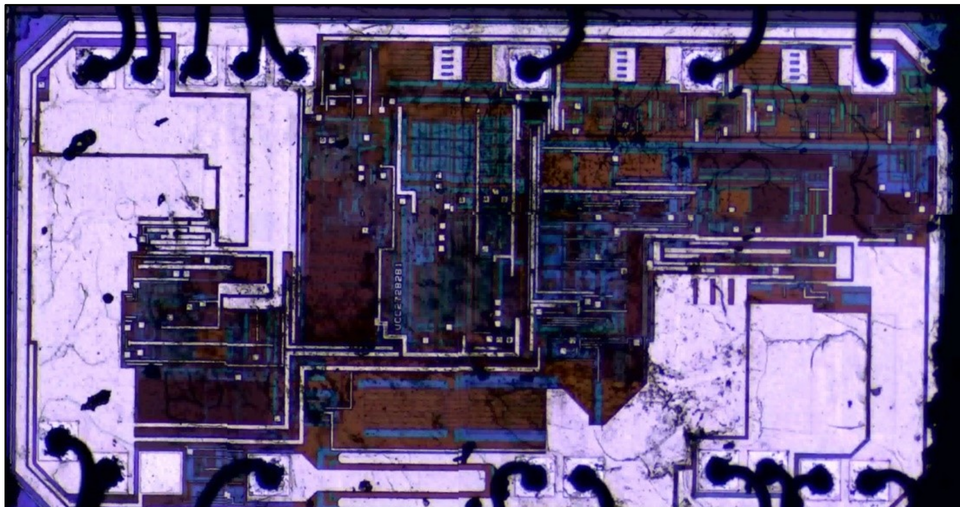

Figure 78. Stitched Image of UCC27282DRC with 5X Objective.

Images of the IC taken with the 10X, 20X, and 50X objectives can be found in Appendix B of this document. Figure 79 shows an image of the IC taken with the 100X objective.

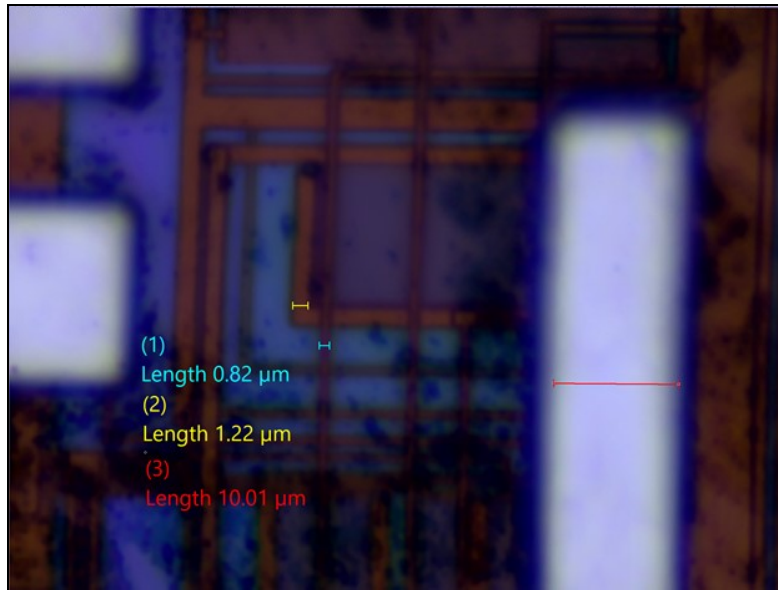

Figure 79. UCC27282DRC Imaged with 100X Objective.

Figure 79 shows an image of the IC taken with the 100X objective. Three features are measured in the view. This demonstrates the system's ability to resolve and identify features less than 1µm, meeting the final system requirement for optics.

5.3.1.3. Pinhole Imaging Research Question Results and Analysis

A question regarding the feasibility of imaging an IC through various sizes of pinholes was posed in section 1.1. It is important to note that imaging an IC through a pinhole is not a functional requirement of the system. Rather, the pinhole is required to be placed over a specific region of interest on the IC. To answer this question of feasibility, several pinholes were aligned with the optical axis and the microscope was focused on the IC behind the pinholes. This process required the use of pinholes and, thus, required collaboration with Dylan Blezinger, whose task it

was to supply and characterize the pinholes. All pinholes used in this section are made of material that is 25µm thick.

Figure 80 shows a view of the largest pinhole used, while Figure 81 shows the region of interest identified on the IC. After the pinhole and IC were imaged separately, the pinhole and region of interest were aligned.

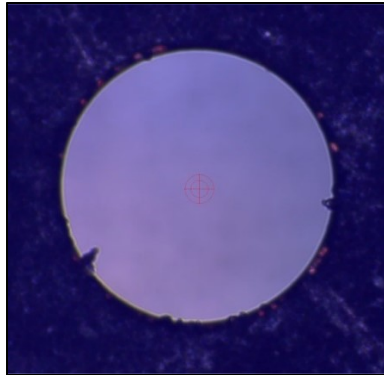

Figure 80. 500µm Pinhole Imaged with 5X Objective.

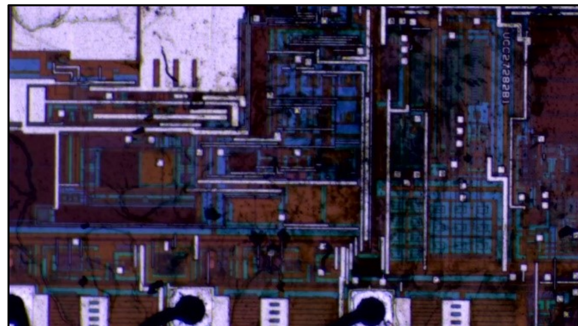

Figure 81. IC Region of Interest Imaged with 5X Objective.

Figure 82 shows the image resulting from the alignment of the pinhole and the region of interest on the IC. The microscope is focused on the region of interest.

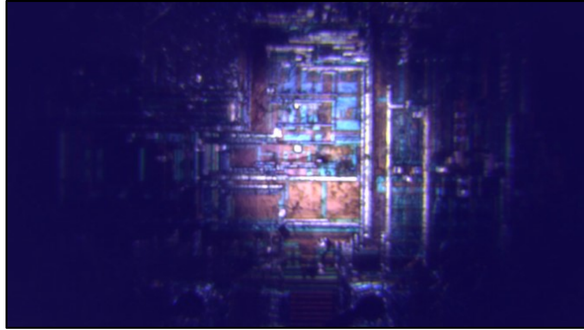

Figure 82. IC Region of Interest Imaged through 500µm Pinhole with 5X Objective.

A large amount of the clarity and detail in the region of interest is lost. The focal point represented is the clearest point of focus within the DOF. After this image was taken, the effects of using the 400µm, 300µm, 200µm, and 100µm pinholes were also investigated using the same procedure. The results of imaging the region of interest through the 500µm, 400µm, 300µm, 200µm, and 100µm pinholes can be found in Appendix B of this document. The last point at which portions of the region of interest could be detected was found with the 200µm pinhole. Figure 83 shows an image of the pinhole and Figure 84 shows the region of interest through the 200µm pinhole.

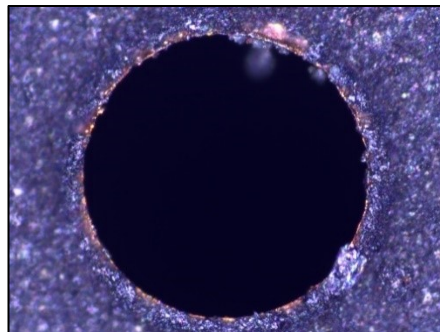

Figure 83. 200µm Pinhole Imaged with 20X Objective.

Figure 84. IC Region of Interest Imaged through 200µm Pinhole with 20X Objective.

The majority of the clarity and detail in the region of interest is lost. The focal point represented is the clearest point of focus within the DOF. This is the smallest pinhole where any features of the IC can be detected.

Due to the design specifications and distance between the pinhole and IC, the feasibility of imaging an IC through pinholes of this size has been determined to be impractical at best. The reason for this is the intersection of the pinhole with the light cone of the objective at a point along the optical axis between the focal point and the pinnacle of the objective. As described in section 2.2.2, an objective capable of resolving small features generally has a higher NA. This higher NA results in a less acute light cone. An objective with a lower magnification may have a low enough NA to image the region of interest of the IC through the pinhole, but it lacks the resolving power required to discern usable features. Additionally, smaller pinholes require a shorter distance between the closest plane of a pinhole and the IC on the other side. The model of an objective's light cone and a model of each pinhole size may be used to illustrate this issue. After modelling the light cone of an objective and all prospective pinholes, each pinhole aperture may be placed in a position where the circular edge of the pinhole on the front plane is

coincident with the light cone. This represents the smallest distance between the front plane of the pinhole and the pinnacle of the objective. The distance between the back plane of the pinhole and the apex of the light cone can then be measured. This measurement represents the maximum distance between the back plane of the pinhole and the surface of an imaged IC where the pinhole does not intersect with the light cone. Figure 85 illustrates this concept with the objectives and pinholes used in this research.

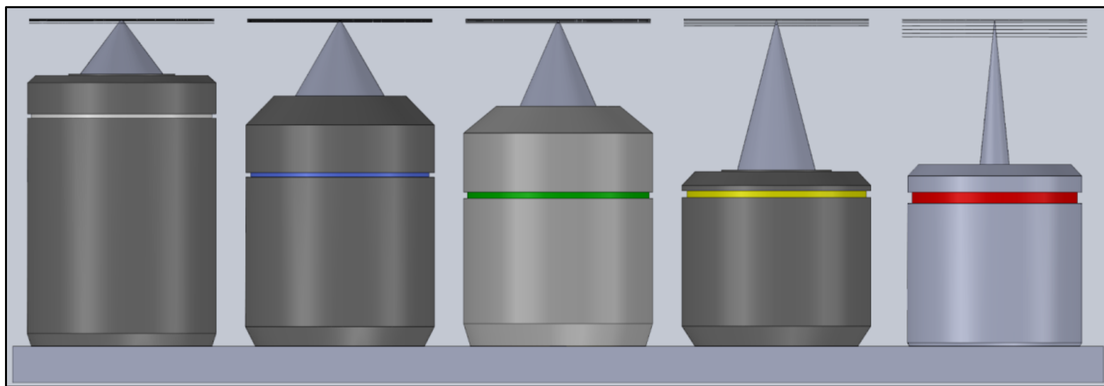

Figure 85. All Pinholes Coincident with All Light Cones.

Figure 86 shows a closer view of the 5X objective's modelled light cone coincident with all pinhole sizes used in this research. The air gap between the apex of the light cone and the back plane of the 500µm hole is measured.

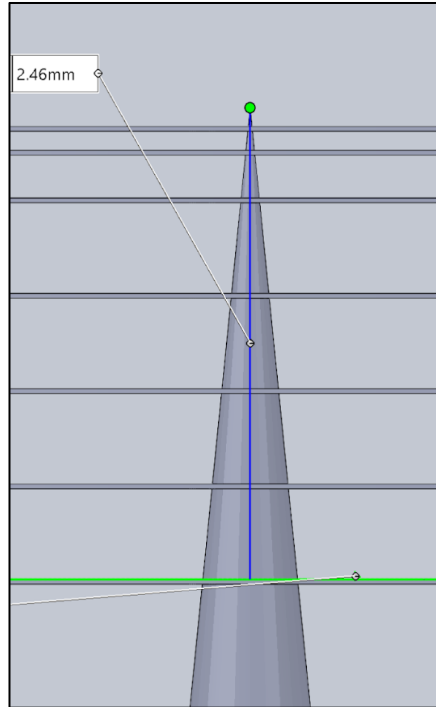

Figure 86. Required Distance from 500µm Pinhole to IC without Light Cone Intersection – 5X Objective.

The required distance from the back plane of the 500µm pinhole to the IC without light cone intersection is 2.46mm. With a ~3mm air gap between the pinhole and the IC used in Figure 82, the large DOF of the 5X objective made up for some of the distance between the apex of the light cone and the IC. Figure 87 shows the same view as Figure 86 with the distance to the 25µm pinhole measured.

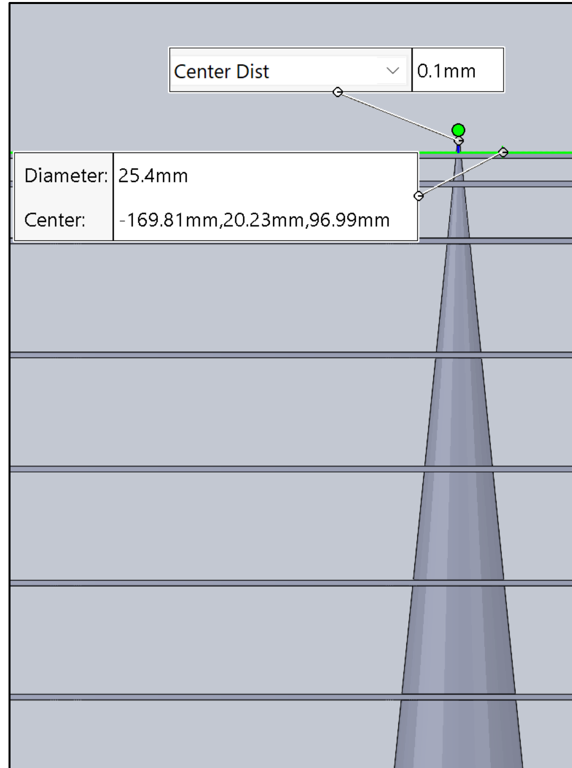

Figure 87. Required Distance from 25μm Pinhole to IC without Light Cone Intersection – 5X Objective.

The distance required for the 25μm pinhole with the 5X objective is 100μm. Moving up in magnification, the distance required to image through 500μm pinhole using the 100X objective is 580μm, while the distance required to image through 25μm pinhole using the 100X objective is 20μm.

These results lead to the following question: Given a system minimum air gap between the back plane of a pinhole and an IC of roughly 2mm, what characteristics would an objective have to possess in order to successfully image an IC through a 25μm pinhole in air? To answer this question, a target 2mm air gap for a 25μm pinhole can be used as an input to solve for the NA. Table 9 lists the calculated parameters for such an objective.

NA	0.006
α	0.344°
n	1.0003
Distance to 500μm Pinhole	41.67mm
Distance to 400μm Pinhole	33.34mm
Distance to 300μm Pinhole	25.00mm
Distance to 200μm Pinhole	16.67mm
Distance to 100μm Pinhole	8.33mm
Distance to 50μm Pinhole	4.16mm
Distance to 25μm Pinhole	2.06mm

Table 9. Parameters for Theoretical Objective Capable of Imaging IC through 25μm Pinhole, ~2mm Air Gap.

A NA of 0.006 and an **α** of 0.344° suggests impossibility. Even if an objective or lens existed with such a low NA, the resolving power would be nowhere near the required values. To effectively image through a 25μm pinhole, the air gap would need to be greatly reduced below 2mm. Calculations in this section are made with a pinhole aperture with a thickness of 25μm, as stated at the beginning of this section. If a pinhole aperture with a thickness greater than 25μm is used, the added thickness is subtracted from the required minimum air gap. Recalling the required minimum air gap of 20μm for the 100X objective to image through a pinhole with a diameter of 25μm, the elimination of an air gap shows that a pinhole has an upper limit for thickness of 45μm. If one's goal was to image an IC through a 25μm in diameter pinhole with a useful resolving power and no air gap, it would be important to take this limit into account.

5.4. Costing Data

The system cost $19,042.85 in material and manufacturing costs. Taxes and shipping costs are not included. Table 10 shows a breakdown of the costs of this system.

Item	Supplier	Cost
Microscope System	Olympus	$14,736.32
Electronics & Wiring	Various	$823.13
Enclosure Hardware	Various	$153.17
Adapter Plate	FEDC	$523.00
Linear Stage & Slide Rails	Various	$664.25
Potentiometers	P3America	$1084.00
Precision Manual Adjusters	Newport	$762.00
3D Printing Filament	SUNLU	$47.98
Miscellaneous Hardware	Various	$83.59
Total		**$19,042.85**

Table 10. Cost Breakdown of System.

6. CONCLUSIONS & FUTURE WORK

6.1. Conclusions

TI tests ICs for SEEs, often using a beam-reduction technique. The process for testing with this technique provided many opportunities for improvement. After defining system requirements and obtaining a sufficient understanding of relevant background information, a microscopy and positioning system was proposed, designed, implemented, and tested. The system performed as designed and met system requirements, accomplishing the objectives of limiting the repetitive test setup actions required to test different regions of interest on a single IC, reducing human error through mechanization of the positioning process, eliminating the attachment of shielding to the IC, and eliminating the transfer of a shielded PCB.

Throughout this research, specific conclusions regarding portions of the system were also formed. For the communication and software portion of this system, the command and feedback communication scheme proved to be a reliable architecture for controlling the system. The EPView software was feature-rich and easy to use, enabling characterization of the positioning system. For the mechanical portion of this system, the 3D printed parts were sufficiently strong and stiff enough to handle operational loads. All electronic components worked to ensure safe and effective operation of the system. For the optics portion of this system, the BXFM met all requirements to successfully image the IC and pinholes.

The research question of the feasibility of imaging an IC through a pinhole with the system was answered. It was determined to be impractical to image an IC through a pinhole of 500μm to 25μm with reasonable constraints.

Overall, the system successfully allows TI to isolate functional blocks of ICs for SEE testing with a streamlined and improved process.

6.2. Future Work

The largest portion of future work that can be done using this system is the imaging and radiated test of various ICs. The system provides a platform for any research that could make use of radiation testing with beam reduction. The combination of the microscopy portion and positioning portion of the system provides the ability to iterate through multiple functional blocks within a single IC for SEE testing. It also provides the ability to iterate through multiple ICs. Through the use of the system in radiation effects testing, new radiation-hardened IC designs may be developed and tested at a much faster rate.

Looking past ICs, the system may be used for imaging and irradiation of components other than electronics. Any research with a material that would benefit from precise radiation testing could use the system, including solar cells, thermal coatings, radiation shielding, and thermoplastics. Automated motion paths for specific use-cases could be developed to irradiate materials in a pattern, testing a variety of materials, thicknesses, or designs in one test. The future uses of this microscopy and positioning system are useful, flexible, and scalable.

REFERENCES

[1] B. Hyman. "Radiation Effects Facility - 3D-View of Testing Area." Cyclotron Institute. https://cyclotron.tamu.edu/ref/heavy_ions.html (accessed September 11, 2021).

[2] J. R. Schwank, M. R. Shaneyfelt, and P. E. Dodd, "Radiation hardness assurance testing of microelectronic devices and integrated circuits: Radiation environments, physical mechanisms, and foundations for hardness assurance," *IEEE Transactions on Nuclear Science,* vol. 60, no. 3, pp. 2074-2100, 2013.

[3] E. B. Salas. "Global space electronics market size 2018 & 2024." Statista. https://www.statista.com/statistics/1057977/global-space-electronics-market/ (accessed October 20, 2021).

[4] "Test Method Microcircuits, Standard MIL-STD-883-1, Department of Defense." https://landandmaritimeapps.dla.mil/Downloads/MilSpec/Docs/MIL-STD-883/std883-1.pdf (accessed September 11th, 2021).

[5] W. Behrens and J. Shaull, "The effects of short duration neutron radiation on semiconductor devices," *Proceedings of the IRE,* vol. 46, no. 3, pp. 601-605, 1958.

[6] J. Koomey, S. Berard, M. Sanchez, and H. Wong, "Implications of historical trends in the electrical efficiency of computing," *IEEE Annals of the History of Computing,* vol. 33, no. 3, pp. 46-54, 2010.

[7] J. Liu *et al.*, "Development of a radiation-hardened 0.18 μm CMOS standard cell library for space applications," in *2014 IEEE International Conference on Electron Devices and Solid-State Circuits*, 2014: IEEE, pp. 1-2.

[8] S. Alvarado. "4 trends in space-grade power management in 2020." Texas Instruments. (accessed September 11, 2021).

[9] R. Quinn *et al.*, "Heavy ion SEU test data for 32nm SOI flip-flops," in *2015 IEEE Radiation Effects Data Workshop (REDW)*, 2015: IEEE, pp. 1-5.

[10] K. Lewis *et al.*, "Single event effects testing for the ADC12DJ3200QML-SP 12-bit, dual 3.2-GSPS single 6.4-GSPS, RF-sampling, JESD204B, analog-to-digital converter (ADC)," in *2019 IEEE Radiation Effects Data Workshop*, 2019: IEEE, pp. 1-6.

[11] C. Castaneda, "Crocker Nuclear Laboratory (CNL) radiation effects measurement and test facility," in *2001 IEEE Radiation Effects Data Workshop. NSREC 2001. Workshop Record. Held in conjunction with IEEE Nuclear and Space Radiation Effects Conference (Cat. No. 01TH8588)*, 2001: IEEE, pp. 77-81.

[12] V. A. Skuratov *et al.*, "Roscosmos facilities for SEE testing at U400M FLNR JINR cyclotron," in *2011 12th European Conference on Radiation and Its Effects on Components and Systems*, 2011: IEEE, pp. 756-759.

[13] V. Anashin, P. Chubunov, A. Koziukov, A. Konyukhov, and G. Protopopov, "Challenges and Approaches to Radiation Hardness Control of Electronic Components to In-Space High-Energy Particles Exposure," in *2018 20th International Symposium on High-Current Electronics (ISHCE)*, 2018: IEEE, pp. 23-26.

[14] V. S. Anashin *et al.*, "Typical facilities and procedure for single event effects testing in roscosmos," in *2015 15th European Conference on Radiation and Its Effects on Components and Systems (RADECS)*, 2015: IEEE, pp. 1-6.

[15] A. E. Koziukov, V. S. Anashin, S. A. Yakovlev, A. S. Bychkov, and V. A. Mazharov, "The Difficulties and Solutions in SEE Radiation Experiments, Test Samples and Setup Preparation," in *2017 17th European Conference on Radiation and Its Effects on Components and Systems (RADECS)*, 2017: IEEE, pp. 1-4.

[16] "SW380T User Manual." Swift Optical Instruments, Inc. https://swiftoptical.com/uploads/pdf/SW380TManual.pdf (accessed September 11, 2021).

[17] M. Abramowitz and M. Davidson. "Anatomy of a Microscope - Numerical Aperture and Resolution | Olympus LS." https://www.olympus-lifescience.com/en/microscope-resource/primer/anatomy/numaperture/ (accessed September 11, 2021).

[18] R. A. Schowengerdt, "Models and Methods for Image Processing," in *Remote Sensing (Third Edition)*, R. A. Schowengerdt Ed., 3rd ed.: Academic Press, 2007, ch. CHAPTER 3 - Sensor Models, pp. 75-126.

[19] M. D. M. Abramowitz. "Anatomy of the Microscope - Objectives: Specifications and Identification | Olympus LS." https://www.olympus-lifescience.com/en/microscope-resource/primer/anatomy/specifications/ (accessed October 15, 2021).

[20] DoverMotion. "Microscope Calculations." https://dovermotion.com/applications-capabilities/automated-imaging/microscope-calculations/ (accessed October 15, 2021).

[21] H. K. M. Abramowitz, K. Spring, B. Flynn, J. Long, M. Parry-Hill, M. Davidson. "Optical Aberrations | Olympus LS." https://www.olympus-lifescience.com/en/microscope-resource/primer/anatomy/aberrationhome/ (accessed October 15, 2021).

[22] Olympus. "Industrial Microscopes DSX1000 Digital Microscopes - High-Resolution Model." https://www.olympus-ims.com/en/microscope/dsx1000/high-resolution-model/ (accessed September 3, 2021).

[23] Navitar. "Navitar 12X Zoom Lens System." https://navitar.com/products/imaging-optics/high-magnification-imaging/12x-zoom/ (accessed August 8, 2021).

[24] PI-USA. "M-406 Precision Linear Stage." M-406 Precision Linear Stage (accessed August 8, 2021).

[25] HeasonTechnology. "How do Ball Screws work?" https://www.heason.com/news-media/technical-blog-archive/how-do-ball-screws-work- (accessed September 8, 2021).

[26] RATTMOTOR. "Linear Stage Actuator." https://www.amazon.com/EBX1605J-Optical-Steppper-Milling-Machine/dp/B08HCP63GB/ref=pd_ybh_a_11?_encoding=UTF8&refRID=N72BG15T4V3FZ39Z0KDN&th=1 (accessed August 8, 2021).

[27] Olympus. "OEM Microscope Components for Integration." https://www.olympus-lifescience.com/en/oem-components/ (accessed July 22, 2021).

[28] StepperOnline. "Digital Stepper Driver - DM542T." https://www.omc-stepperonline.com/digital-stepper-driver-10-42a-20-50vdc-for-nema-17-23-24-stepper-motor-dm542t.html (accessed September 8, 2021).

[29] PRJC. "Teensy 4.1 Development Board." https://www.pjrc.com/store/teensy41.html (accessed October 15, 2021).

[30] LittleMachineShop. "Starrett 0-1" Electronic Digital Micrometer." https://littlemachineshop.com/products/product_view.php?ProductID=1845 (accessed September 8, 2021).

APPENDIX A

The first twelve figures in this appendix accompany the concept of operation explanation found in section 3.7. The next two figures, referenced in section 4.3, are pictures of the fully implemented system.

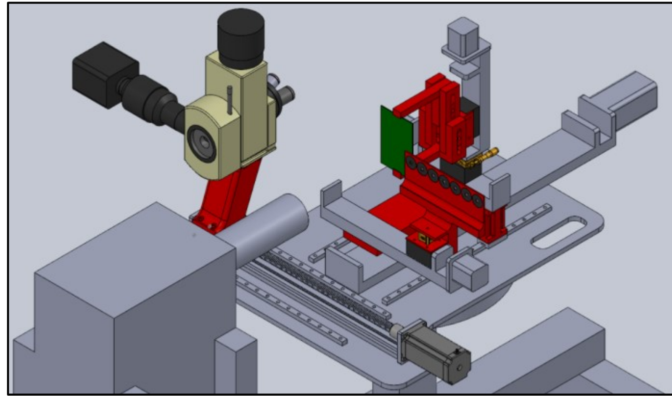

A-A- 1. Step 1: System in the Starting Position.

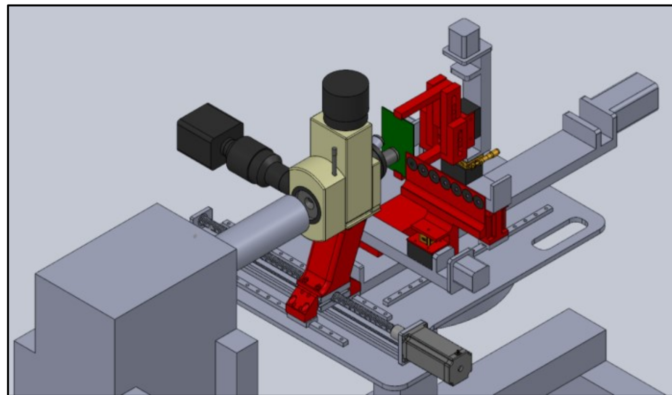

A-A- 2. Step 2: Microscope Centered.

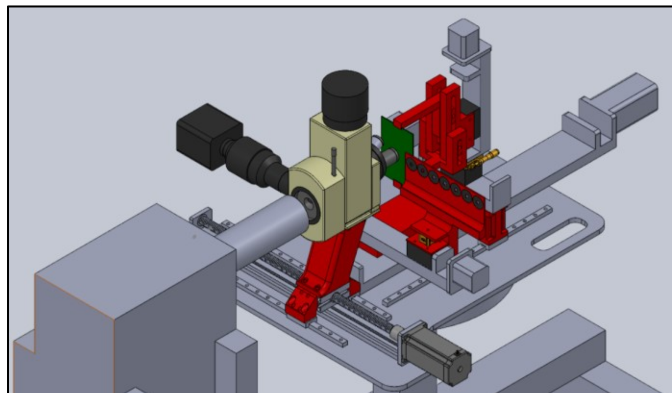

A-A- 3. Step 3: PCB Positioned Vertically.

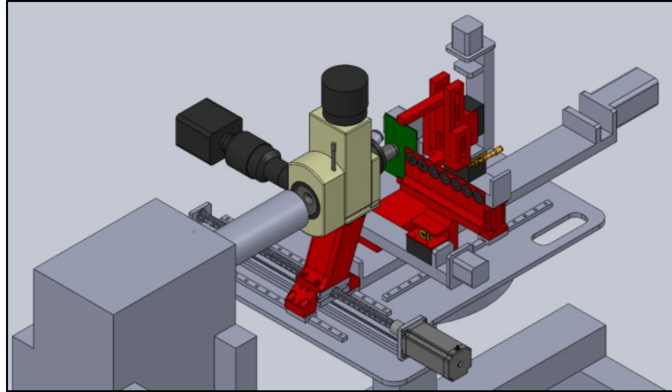

A-A- 4. Step 4: PCB Positioned Horizontally.

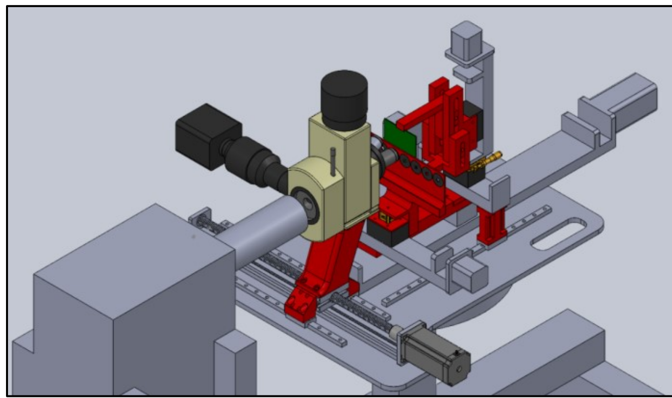

A-A- 5. Step 5: Desired Pinhole Centered.

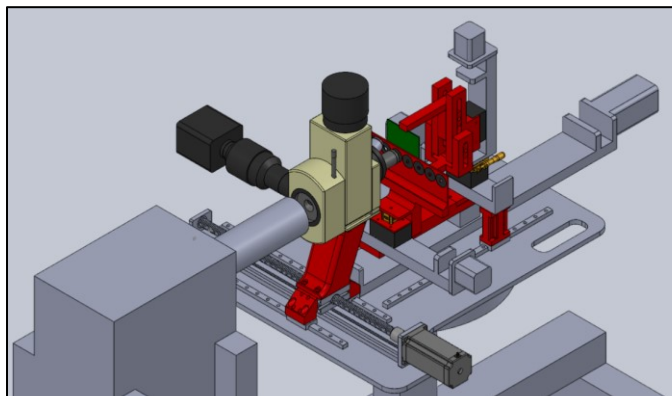

A-A- 6. Step 6: PCB/Pinhole Group Moved Away to Focus on Pinhole.

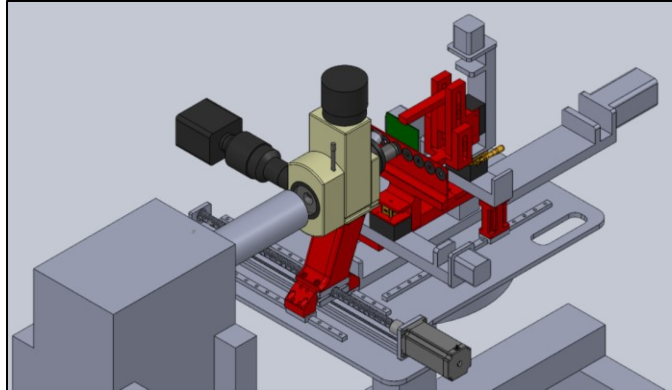

A-A- 7. Pinhole In Focus and Centered.

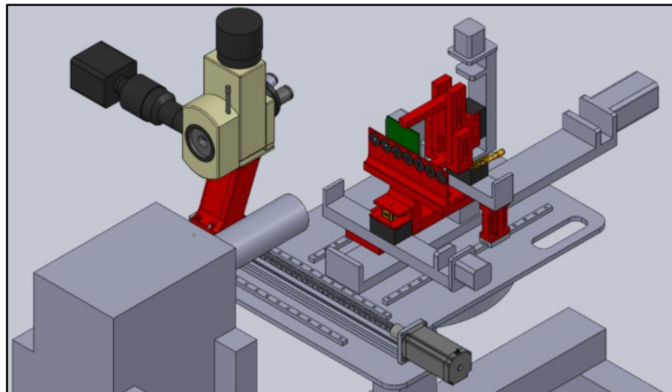

A-A- 8. Microscope Moved to Test Position.

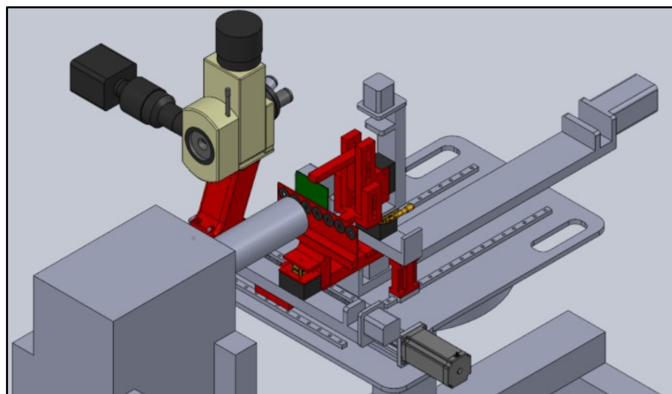

A-A- 9. PCB/Pinhole Group Moved to Test Position.

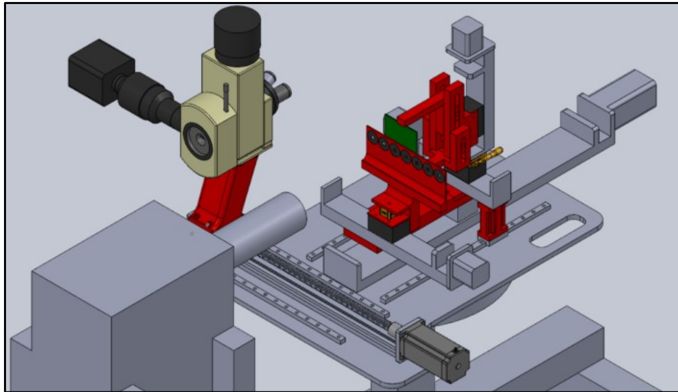

A-A- 10. PCB/Pinhole Group Moved to Align Position After Testing.

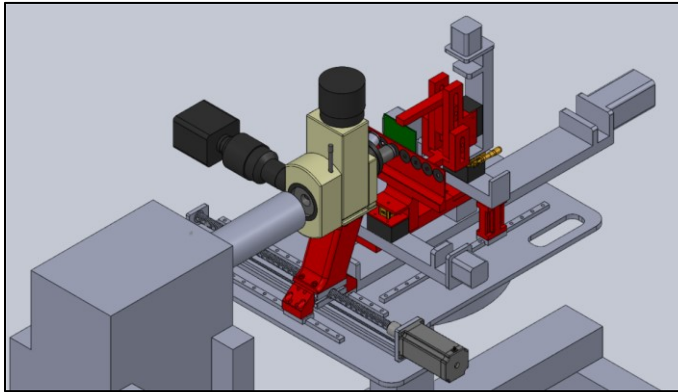

A-A- 11. Microscope Moved to Align Position.

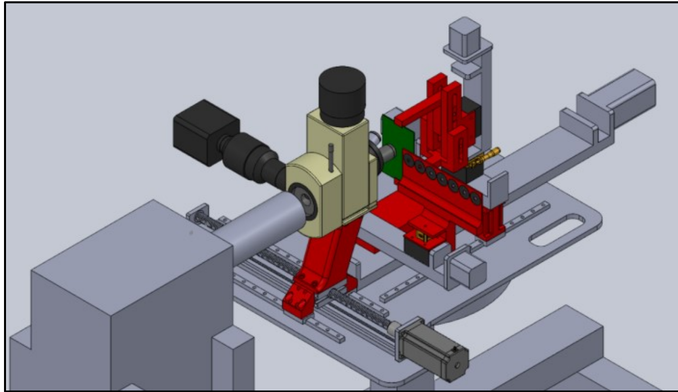

A-A- 12. Pinhole Frame Moved to Focus on PCB.

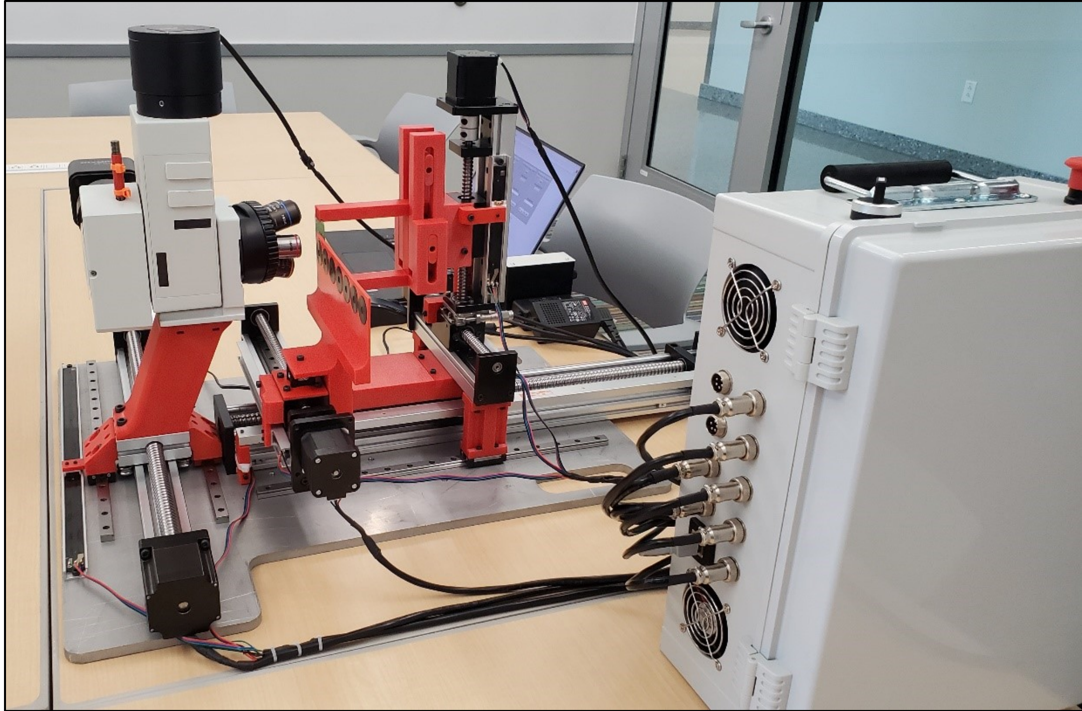
A-A- 13. Fully Implemented System – Side View.

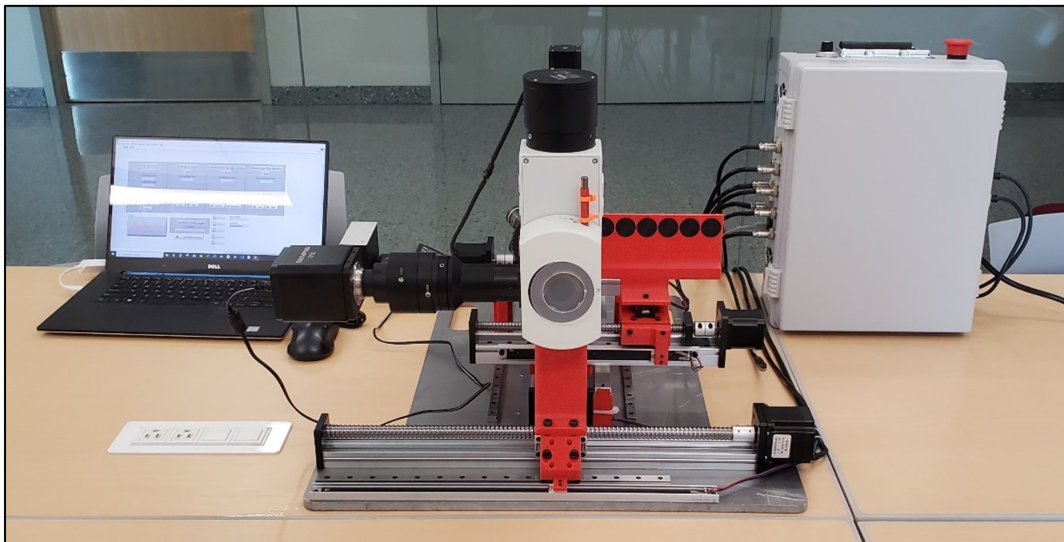
A-A- 14. Fully Implemented System – Rear View.

APPENDIX B

The first six figures if this appendix, referenced in section 5.1.2, contain the error distribution plots of each linear motion rail and direction. The next three figures, referenced in section 5.3.1.2, are images of the UCC27282DRC IC. The last figure, referenced in section 5.3.1.3, contains images of each pinhole tested and a view of the UCC27282DRC IC through these pinholes.

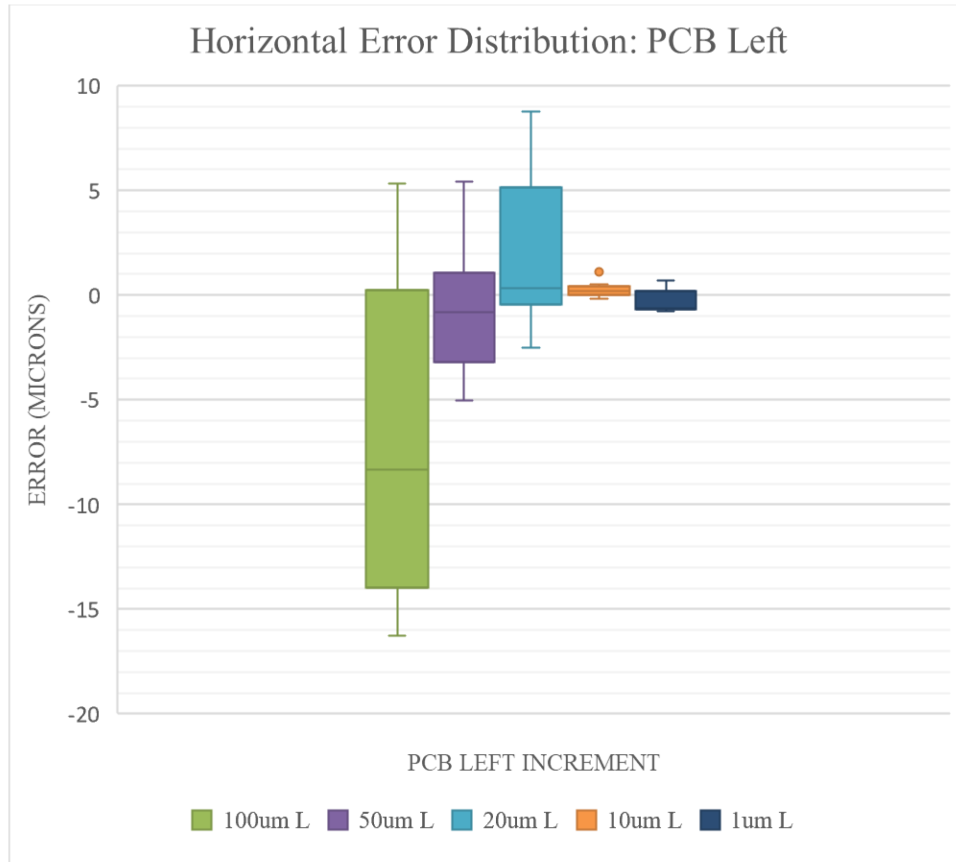

A-B- 1. Horizontal Error Distribution: PCB Left.

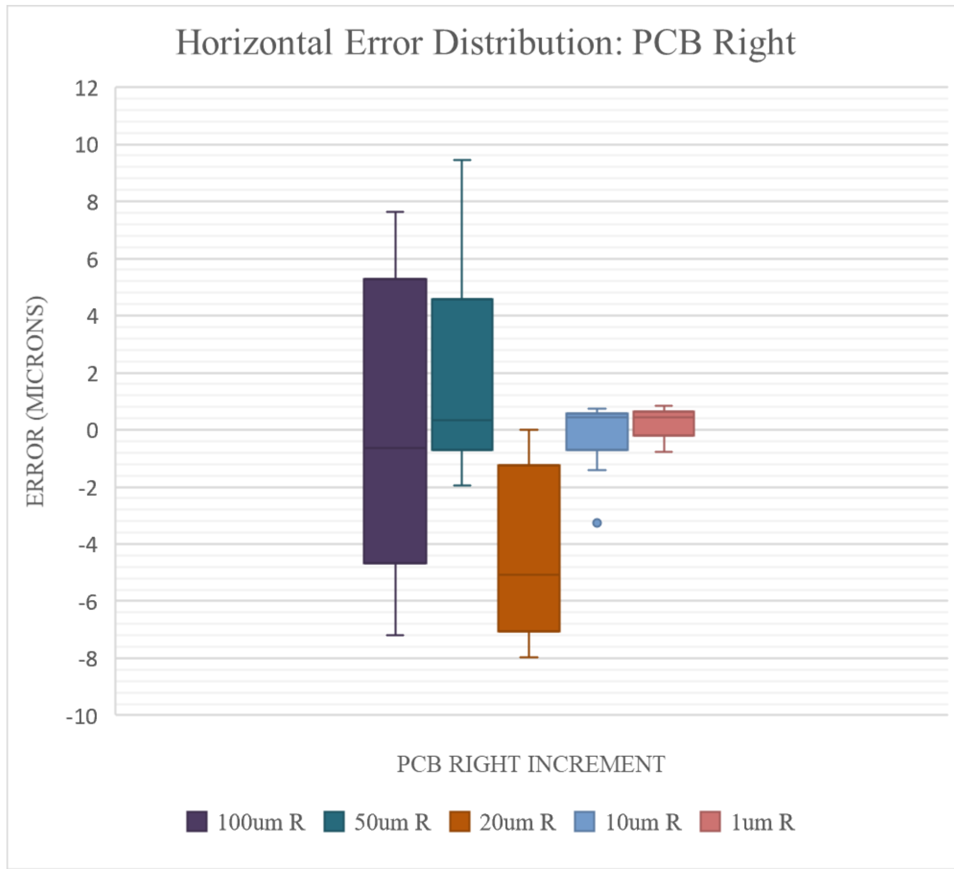

A-B- 2. Horizontal Error Distribution: PCB Right.

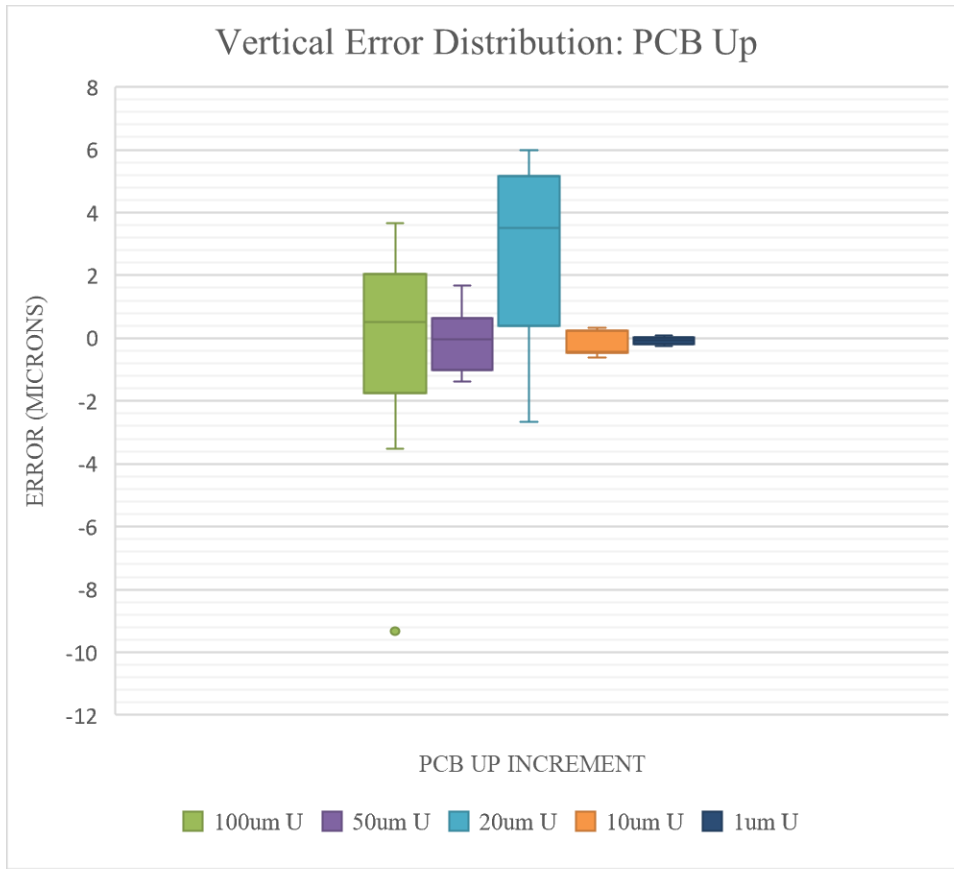

A-B- 3. Vertical Error Distribution: PCB Up.

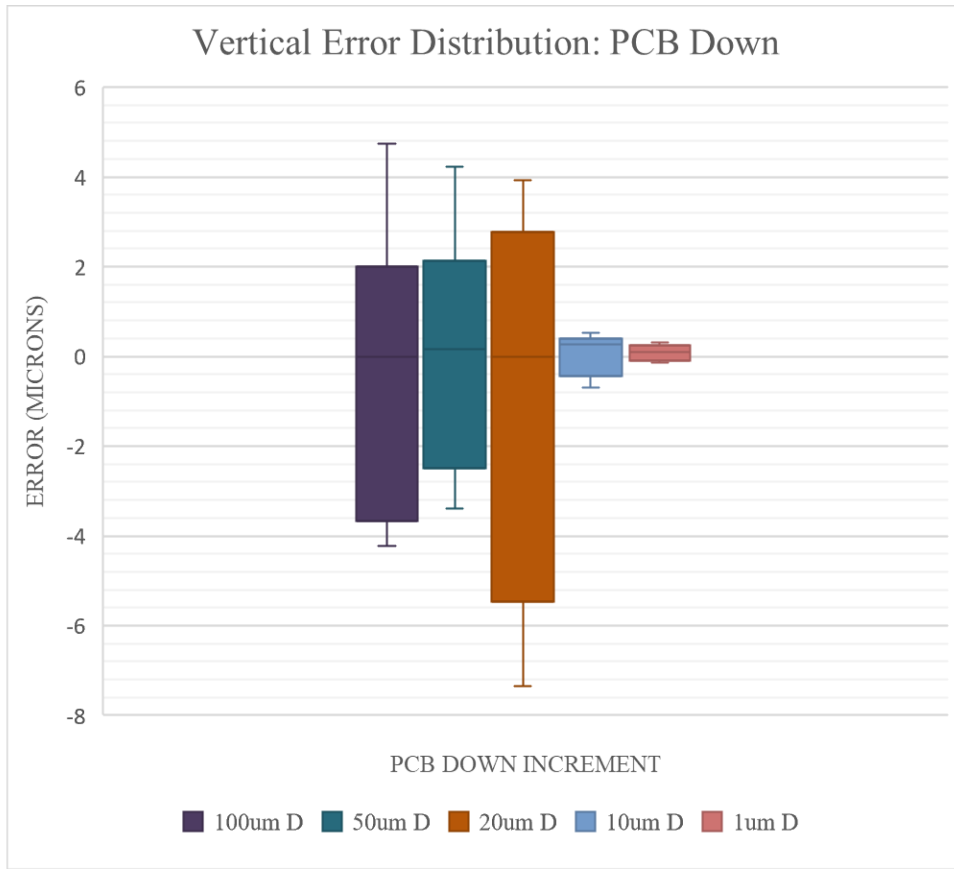

A-B- 4. Vertical Error Distribution: PCB Down.

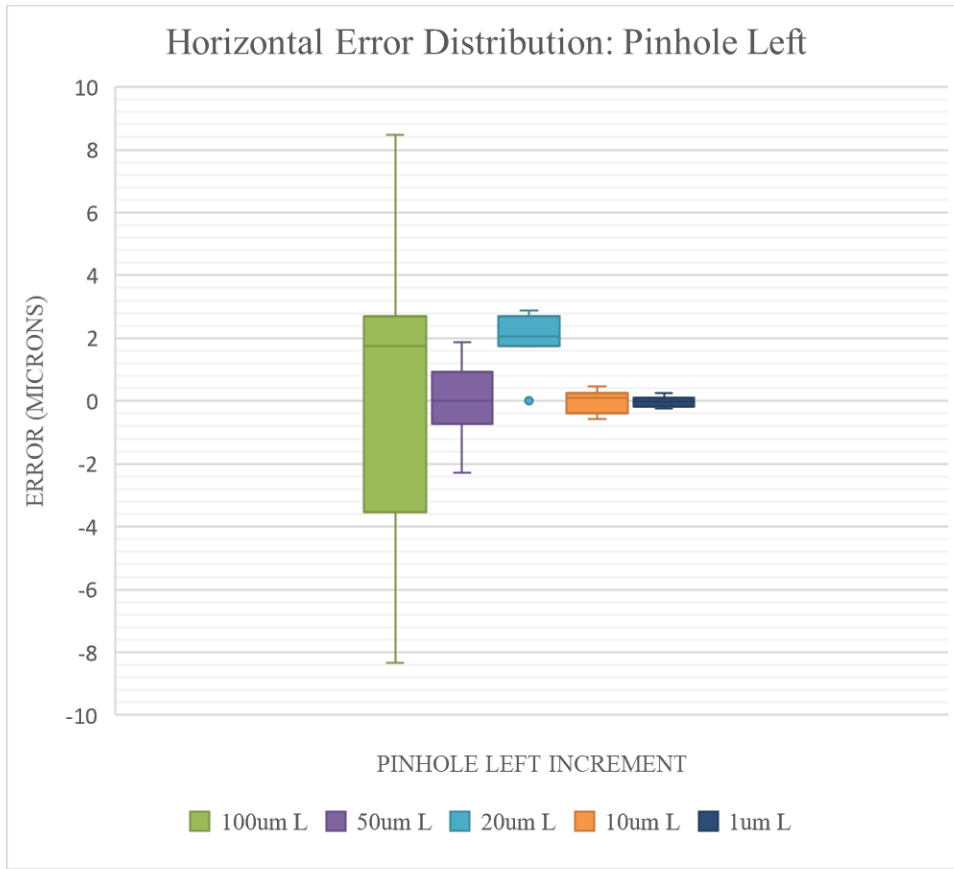

A-B- 5. Horizontal Error Distribution: Pinhole Left.

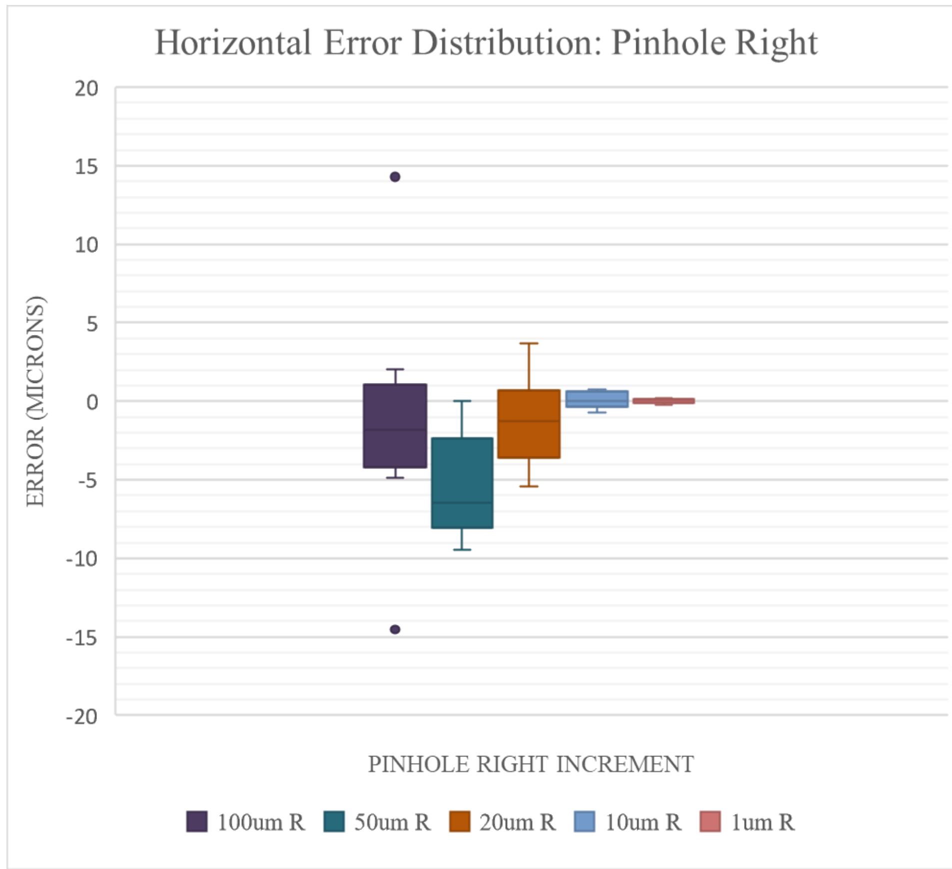

A-B- 6. Horizontal Error Distribution: Pinhole Right.

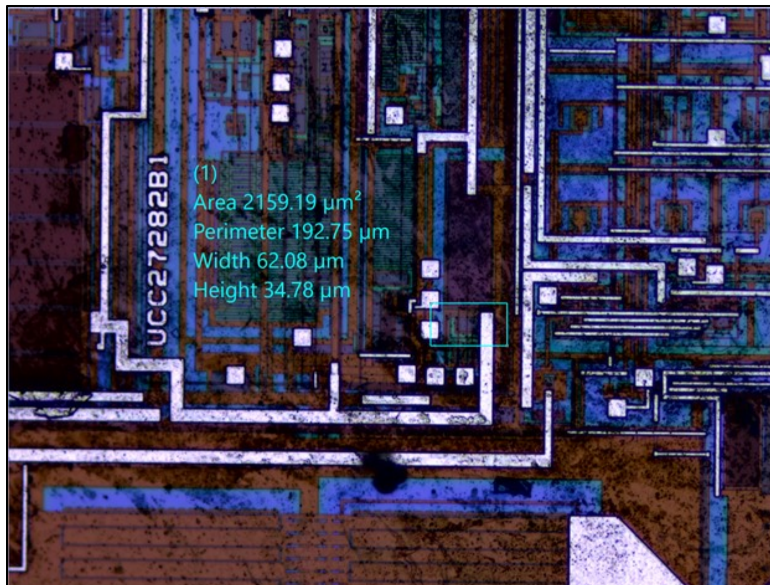

A-B- 7. UCC27282DRC Imaged with 10X Objective.

A-B- 8. UCC27282DRC Imaged with 20X Objective.

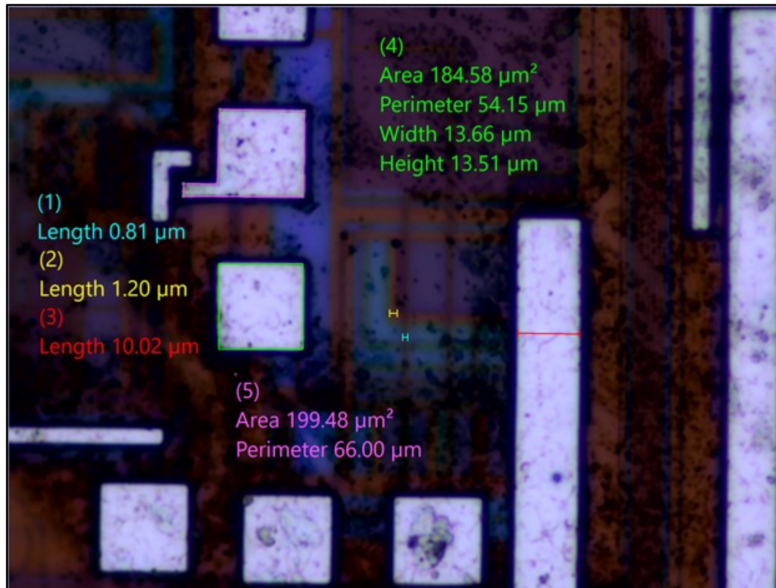

A-B- 9. UCC27282DRC Imaged with 100X Objective.

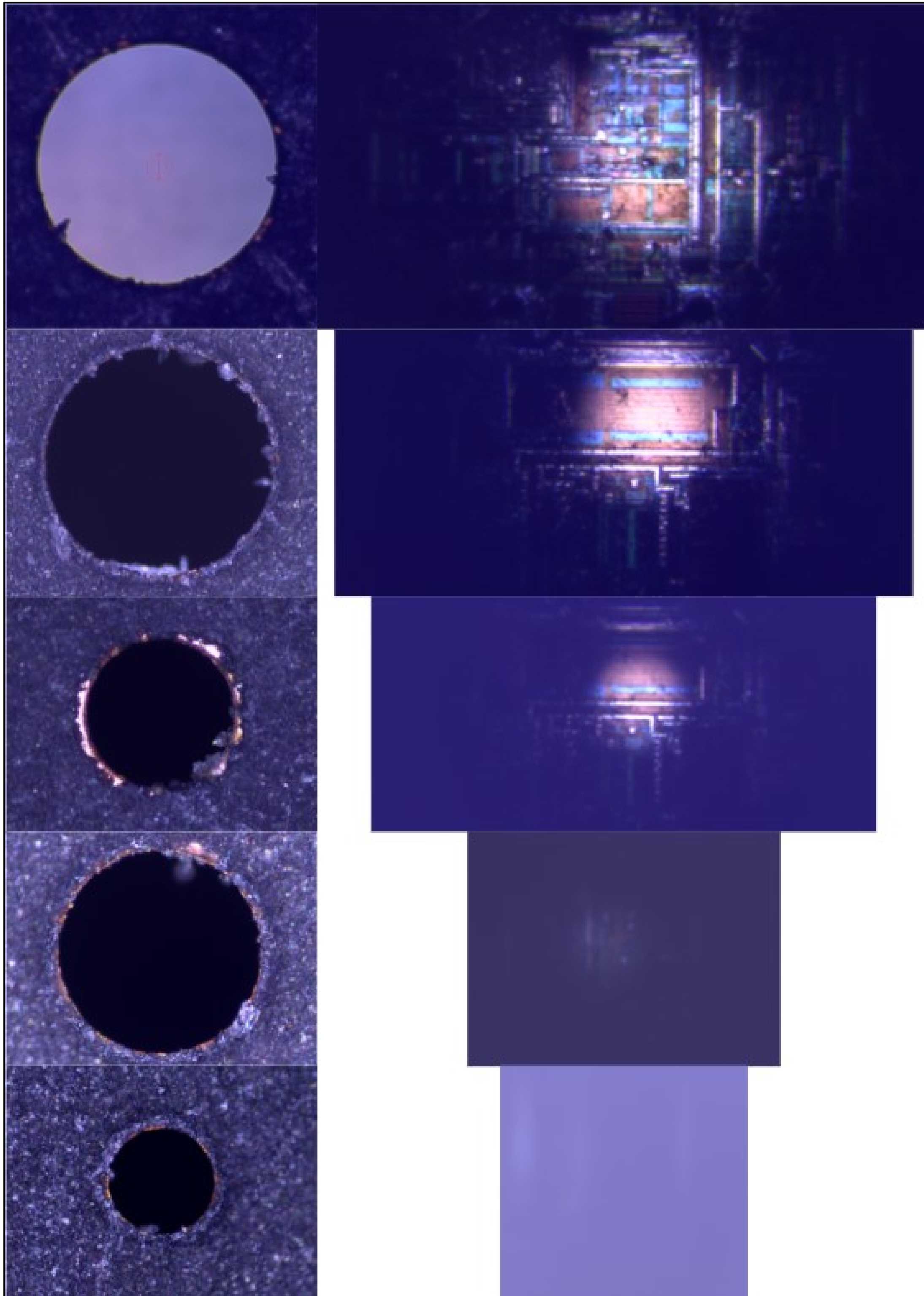

A-B- 10. Full Comparison of Imaging IC Through 500µm, 400µm, 300µm, 200µm, and 100µm Pinholes.